GaAs Blocked-Impurity-Band Detectors for Far-Infrared Astronomy

by

Benjamin Lewin Cardozo

B.S. (University of California at Berkeley) 1999
M.S. (University of California at Berkeley) 2001

A dissertation submitted in partial satisfaction of the
requirements for the degree of
Doctor of Philosophy

in

Engineering-Materials Science and Engineering

in the

GRADUATE DIVISION
of the
UNIVERSITY OF CALIFORNIA, BERKELEY

Committee in charge:
Professor Eugene Haller, Chair
Professor Oscar Dubon
Professor Reinhard Genzel

Fall 2004

The dissertation of Benjamin Lewin Cardozo is approved:

Chair Date

Date

Date

University of California, Berkeley

Fall 2004

Abstract

GaAs Blocked-Impurity-Band Detectors for Far-Infrared Astronomy

by

Benjamin Lewin Cardozo

Doctor of Philosophy in Engineering-Materials Science and Engineering

University of California, Berkeley

Professor Eugene Haller, Chair

High-purity and doped GaAs films have been grown by Liquid-phase epitaxy (LPE) for development of a blocked impurity band (BIB) detector for far-infrared radiation. The film growth process developed has resulted in the capability to grow GaAs with a net active impurity concentration below 1×10^{13} cm^{-3}, ideal for the blocking layer of the BIB detector. The growth of n-type LPE GaAs films with donor concentrations below the metal-insulator transition, as required for the absorbing layer of a BIB detector, has been achieved. The control of the donor concentration, however, was found to be insufficient for detector production. The growth by LPE of a high-purity film onto a commercially grown vapor-phase epitaxial (VPE) n-type GaAs doped absorbing layer resulted in a BIB device that showed a significant reduction in the low-temperature dark current compared to the absorbing layer only. Extended optical response was not detected, most likely due to the high compensation of the commercially grown GaAs absorbing layer, which restricts the

depletion width of the device.

Professor Eugene Haller
Dissertation Committee Chair

Contents

List of Figures

List of Tables

Acknowledgments

The work presented in this thesis would not have been possible without the help of several people. I would like to thank Professor Eugene Haller for his guidance and teaching throughout my graduate and undergraduate study. His help both in and out of the laboratory has been invaluable. Thanks to Jeff Beeman, who helped me in virtually every part of my research. His knowledge and experience within the fields of semiconductor processing and far-infrared detectors provided an excellent resource for me. Thanks to David Hom for helping me with administrative issues, which are substantial at a government laboratory such as the Lawrence Berkeley National Lab. Thanks to Bill Hansen, who I've come to countless times for questions about laboratory procedures. Lothar Reichertz provided a great deal of help with Fourier transform spectroscopy and many other laboratory techniques. His expertise in computer automated control of scientific equipment, and in cryogenic system design, greatly sped the progress of this research. Thanks to all members of the Haller group for their help and for providing interesting discussions about research and other topics. Thanks to Professor Nancy Haegel for her efforts in BIB detector modeling, and for helpful discussions throughout the research process. Thanks also to the group of Mike Thewalt at Simon Fraser University, in Burnaby, Canada, for their photoluminescence and magnetophotoluminescence characterization of many GaAs films. Thanks to my family for putting up with seeing me so infrequently over the past few years, as I dedicated myself to my education and to this work. An finally, thanks to my girlfriend Hadas for giving me the best reason to work hard on nights and weekends, so I could finish faster to be with her after many years of 3000 miles of separation.

This project was supported by NASA Ames Research Center, Order Nos. A53228D and NNA04CA94I through the U.S. Department of Energy under Contract No. DE-AC03-76SF00098.

Chapter 1

Detectors for Far-infrared Astronomy

1.1 Astronomy in the far-infrared

Astronomical observations have been of great scientific importance since the beginning of human civilization. Until the the last century, all studies of celestial bodies were made by the detection of photons by the human eye in the relatively narrow, *visible* region of the electromagnetic spectrum. Detection of visible light has been used to study planets within our solar system as well as stars in our galaxy and neighboring galaxies that are not obscured by cosmic dust. The astronomy of wavelengths outside the visible region, such as γ-ray, X-ray, infrared, and radio waves, gained importance with the advent of ground-based detection systems in the first half of the twentieth century, revealing a wealth of new discoveries about the universe not observed in the visible region. These include black holes,

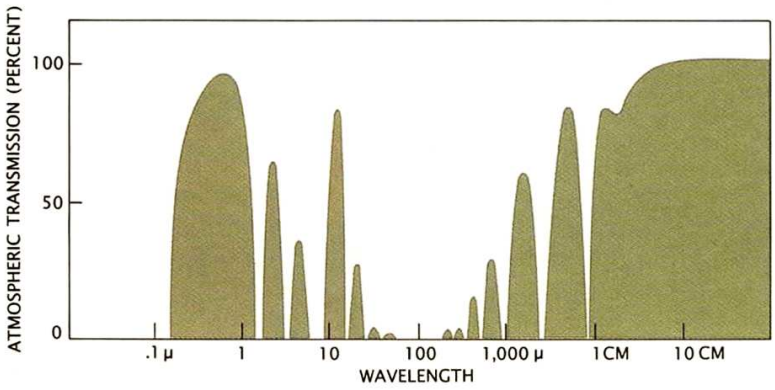

Figure 1.1: The transmission spectrum for photons through the atmosphere of Earth. With the exception of a few narrow windows, signals near 100 μm are highly attenuated. After [61].

neutron stars, and highly redshifted galaxies.

Due to several reasons, the far-infrared region, usually defined as the wavelength region between 10 and 1000 microns, remained unexplored until much later. First, photons in this region of the spectrum are heavily absorbed by the atmosphere. Figure 1.1 shows the transmission spectrum of space-originating photons through Earth's atmosphere. The low transmission near 100 μm is due primarily to excitation of vibrational and rotational modes of various molecules in the atmosphere. Principal among these are H_2O, O_2, O_3, CO_2, N_2O, and CH_4 [62]. Because of the minimal atmospheric transmission at these wavelengths, ground-based far-infrared telescopes have been limited to operation at high altitudes, where the atmosphere is of low density. An example is the the James Clerk Maxwell telescope on Mauna Kea, Hawaii. At an elevation of 4092 m, the atmospheric pressure outside the observatory is 40% lower than at sea level. Airplane-based telescopes operate at significantly higher altitudes, such as NASA's Stratospheric Observatory for Infrared Astronomy (SOFIA), which is expected to fly at altitudes over 12 km, where the atomspheric pressure

is 80% lower than at sea level [34]. Space-based telescopes, such as the Spitzer satellite telescope, currently in orbit, operate in by far the best conditions available for far-infrared observations.

Second, to achieve sufficient signal to noise ratios, detectors in the far-infrared invariably require cooling to temperature well below 10 K and furthermore require complex readout electronics that must also be cooled. Third, the lack of industrial or military applications for far-infrared detectors means that most detector development had to be funded exclusively by the astronomy research community. Because of this situation, there is often no industrial production of many specialty materials required for making far-infrared detectors, greatly slowing advances.

Far-infrared observations are important for several reasons, three of which will be discussed here. First, detection in the far-infrared is necessary to reveal and explore cool objects in space, such as planets, asteroids, cosmic dust clouds, and newly forming stars. The peak of the blackbody emission from these bodies lies in the mid to far-infrared. Their emission in the visible range of the spectrum is too weak to be observed by standard optical telescopes. The detection of low temperature cosmic dust is especially important in the investigation of star formation. Stars are believed to form out of clouds of dust and hydrogen gas. As the clouds become more massive, they begin to collapse into a smaller volume, causing the center to be under tremendous pressure, and to heat up. At sufficiently high pressure a protostar is formed, the center of which heats up to several millions of degrees, facilitating nuclear fusion and forming the star. Astrophyhysicists can observe the temperature distribution of gas and dust clouds believed to be involved in star formation

using infrared and far-infrared telescopes such as those described above.

Second, as mentioned above, the molecular vibrational and rotational mode wavelengths of most gaseous species are between 10 and 1000 μm. This means that infrared and far-infrared telescopes make possible the spectroscopy of interstellar gas clouds, allowing the identification of their composition. Hydrogen gas can be identified by observing the vibrational states of molecular hydrogen that has been stripped of one electron (designated H II). The spectral shift of these emission lines with allows astrophysicists to deduce the temperature of the gas.

Third, the signals from the furthest galaxies that have been discovered are highly doppler red-shifted due to the expansion of the universe. Many of these galaxies are now brightest in the infrared, and cannot be seen using optical telescopes. The observation of these very distant galaxies is important for studies concerning the origin of the universe. The James Webb Space Telescope, set to be launched in 2011, is under construction for this purpose.

1.2 Fundamentals of semiconductor far-infrared detectors

Semiconductor based detectors are by far the most widely used type of photon transducers in the far-infrared. The properties of semiconductors are often dominated by the addition of impurity species that contain a different number of valence electrons compared to the host material. For details about the properties of impurities in semiconductors see the book by Kittel [40]. A specific review of the properties of donor impurities in GaAs is provided in Appendix A.

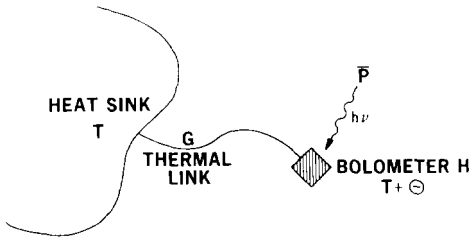

Figure 1.2: Thermal circuit for bolometer operation. The bolometer is usually composed of an absorber and a transducer. [27]

Transduction of far-infrared photons for telescopes is dominated by two classes of detectors: thermal detectors used in bolometers and extrinsic photoconductors. These two types of devices operate based on entirely different interactions with the incident light, and are useful under different kinds of operational conditions. In the following sections, the fundamentals of operation of bolometers and extrinsic photoconductors, a subset of general photoconductor detectors, will be reviewed. The advantages and disadvantages of each, under varying environmental and operational conditions, will be discussed.

1.2.1 Bolometers

As is obvious from their name, thermal detectors operate by sensing the temperature change of a material when exposed to a photon flux. The most common thermal detector, a bolometer, in the simplest case, consists of a material whose electrical characteristics are highly sensitive to changes in temperature. Bolometers are sensitive to the power of the incident photon flux, and therefore to all wavelengths equally, as long as the total energy transferred is the same. In application, the bolometer is connected to a heat sink at temperature $T_{\rm s}$ via a thermal link with thermal conductance G (Figure 1.2). The temperature of the bolometer increases by an amount $T_{\rm b}$ as it absorbs a constant photon

flux with power P. The rate of heating of the bolometer is $\frac{dT_\mathrm{b}}{dt} = \frac{P}{C}$, where C is the heat capacity. Since the bolometer has a higher temperature than the sink, heat is transferred via the thermal link until steady state is once again reached. If a fluctuating signal of power $P_1(t)$ is also incident on the detector, the total power absorbed by the detector is

$$P(t) = P + P_1(t) = GT_\mathrm{b} + C\frac{dT_\mathrm{b}}{dt} \tag{1.1}$$

Given the initial conditions of the photon flux being turned on at t=0, Equation 1.1 can be solved for the temperature of the bolometer as a function of time as

$$T_\mathrm{b}(t) = \frac{P}{G} + \frac{P_1}{G}\left(1 - e^{\frac{-t}{\tau}}\right) \tag{1.2}$$

where $\tau = C/G$ is the thermal time constant.

The temperature change causes a variation in the resistance of the bolometer which, if the device is biased under constant current conditions, can be sensed as a changing voltage. The temperature dependence of the resistance is represented by a temperature coefficient, α_T, defined as

$$\alpha_\mathrm{T} = \frac{1}{R_\mathrm{b}}\frac{dR_\mathrm{b}}{dT} \tag{1.3}$$

where R_b is the bolometer resistance. It is desirable to choose a material with a large value of α_T in order to maximize the detector response. One such material is Ge that has been doped p-type with an acceptor concentration of between 1.0×10^{15} to 1.0×10^{16} cm^{-3} by neutron transmutation (NTD) [27]. At low temperatures, electrical conduction in this system is dominated by charge carrier hopping between impurity centers. Hopping is a thermally activated process. For a p-type semiconductor such as NTD germanium, a hole that absorbs a phonon can gain sufficient energy to escape its weak bond to an acceptor center, move

under an applied field, and re-emit the phonon to bind to an empty nearby impurity center, resulting in electrical conduction. This process is completely thermal in nature, compared to the photoionization process of an extrinsic photoconductor detector discussed in Section 1.2.2. A more detailed explanation of hopping conduction in semiconductors is provided in Appendix B. The magnitude of the resistivity for hopping conduction in moderately doped NTD Ge is given in Equation 1.4, where Δ and ρ_o are constants [27].

$$\rho = \rho_o e^{(\frac{\Delta}{T})^{1/2}} \tag{1.4}$$

Unfortunately, the far-infrared absorption efficiency is relatively low for neutron transmutation doped (NTD) Ge and most other materials that have highly temperature sensitive electronic properties. Materials that are highly absorbing of far-infrared radiation and have small heat capacity, such as metal films, exhibit only a weak temperature dependence of their electrical properties, and are therefore unsuitable as a detector. This problem has been solved by the introduction of composite bolometers, which have separate absorbing and temperature sensing components.

A schematic of a composite bolometer is shown in Figure 1.3, where a temperature sensing thermistor has been glued to a highly absorbing metal film and deposited on a transparent but highly thermally conductive substrate. In the case of a standard composite bolometer, heat from the thin film absorber is transferred through the sapphire or diamond substrate to the thermistor. In most cases the thermistor element is a piece of high quality, compensated, NTD germanium as just discussed. For weak signals, the temperature increase due to absorption can be quite small. From statistical thermodynamics, thermal fluctuations

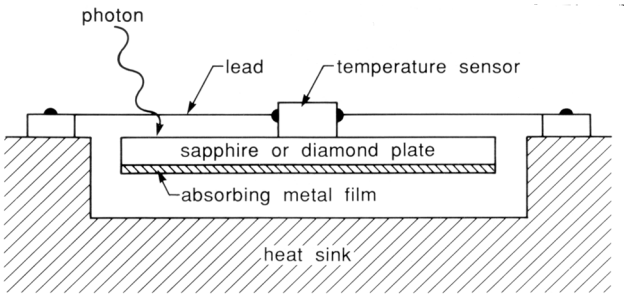

Figure 1.3: Schematic of a composite bolometer with an absorbing metal film. After [57].

occur in equilibrium due to energy fluctuations described by Equation 1.5.

$$\langle (\Delta u)^2 \rangle = k_{\mathrm{B}} T_{\mathrm{s}}^2 C \tag{1.5}$$

For low background conditions, bolometers are designed to operate at very low temperatures, as low as 0.1 K, to reduce the thermal fluctuation noise to sufficiently low levels.

Recent efforts have focused on the development of superconducting transition edge bolometers [55]. These devices take advantage of the extremely large change in electrical conductivity of a superconductor as it approaches its transition temperature. They can be fabricated using conventional planar techniques, such as thin film deposition and lithographical patterning. The low impedance of superconducting thermometers, however, is not well matched to the standard low-noise amplifiers used with Ge thermistors or photoconductors. This makes development of the readout electronics particularly complicated, and has become a major limiting factor for superconducting bolometers.

Only a brief description of bolometer operation and design has been given here. For further information the reader is referred to the review article by Richards [55].

1.2.2 Extrinsic semiconductor photoconductor detectors

Semiconductor based photoconductor detectors utilize an entirely different mechanism of transduction than do thermal detectors. Often referred to as photon detectors, response in a photoconductor involves the change of conductivity due to the excitation of electrons or holes by photons. A semiconductor in which the conductivity is dominated by electron-hole pairs that have been excited across the bandgap is called an intrinsic semiconductor. If the conductivity is determined by the addition of impurities which have a different number of valence electrons than the host, the semiconductor is considered to be extrinsic. For a brief review of the properties of intrinsic and extrinsic semiconductors the reader is referred to the book by Kittel [40]. The most basic extrinsic photoconductor consists of a piece of semiconductor that has been lightly doped with shallow level impurities, and has ohmic contacts on opposing sides. At low temperatures, most dopant atoms (donors or acceptors) bind a carrier (electron or hole) and are neutral, or "frozen out" (Figure 1.4(a)). In this state, the crystal is an electrical insulator since there are few ionized dopants producing free charge carriers. These free carriers, which conduct in the absence of an infrared signal constitute a dark current, contributing white noise to the output signal of the detector. An electron in the 1s ground state of an impurity potential in a cooled n-type extrinsic photoconductor can be excited by a photon into the conduction band directly. Alternatively, the conduction band can be reached by the combination of photon excitation into an excited state followed by the absorption of a phonon into the conduction band directly. Once free, the electron will drift under an applied electric field until it encounters and recombines with another ionized donor. This process is illustrated in Figure 1.4(b).

The motion of the electron constitutes a signal current, which is amplified by an external circuit such as a transimpedence amplifier. The average distance l that an electron travels under the applied field E is defined by its velocity v and mean recombination lifetime τ_{m} in Equation 1.6. τ depends on the density of recombination centers within the semiconductor bulk. If the semiconductor is of high crystalline quality, there will be few dislocations and volume defects, recombination will occur almost exclusively when the electron encounters an ionized donor. Hence τ depends largely on the compensation ratio of the semiconductor since the concentration of ionized donors is nearly equal to the concentration of acceptors. The average velocity of electron drift in a solid is determined by the carrier mobility μ and the electric field E.

$$l = v\tau_{\mathrm{m}} = \mu E \tau_{\mathrm{m}} \tag{1.6}$$

The photoconductive gain $\mathcal{G}$ is the ratio of l to the width of the detector L. In the limiting case of no compensation, the photoconductive gain can approach values much higher than unity, with an electron *effectively* traveling through the photoconductor many times before recombination.

The attenuation of a photon flux through a solid is determined by Beer's law,

$$\frac{I}{I_{\mathrm{o}}} = \frac{(1-r)^2 e^{-\alpha w}}{1 - r^2 e^{-2\alpha w}} \quad , \tag{1.7}$$

which accounts for multiple internal reflections within a device having surface reflectivity r and linear absorption coefficient α. Here I and I_{o} are the initial and final intensities, and w is the sample width in the direction of the incident photon flux. For a photoconductor, the absorption coefficient is related to the probability of a free electron to be generated per incident photon, or the quantum efficiency η. If multiple reflections from the surfaces are

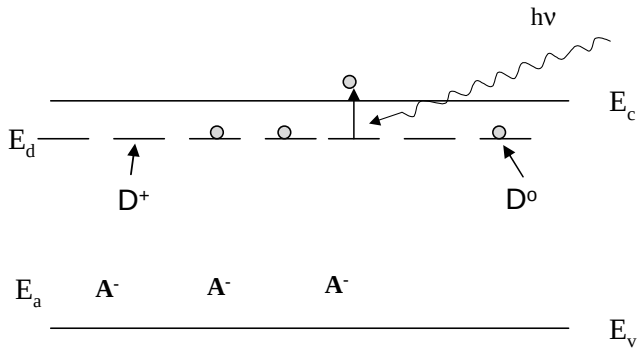

(a)

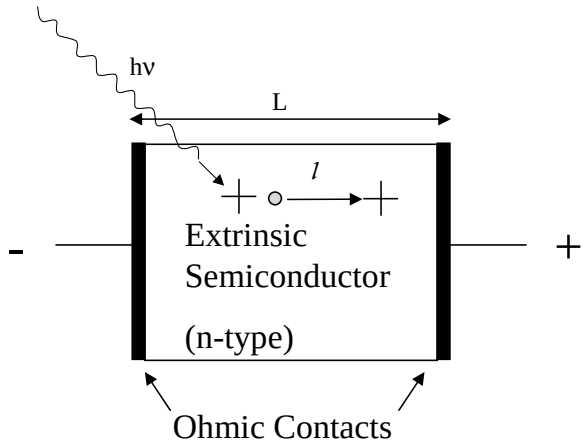

(b)

Figure 1.4: a) Band diagram of a compensated, n-type extrinsic photoconductor. It is cooled to low enough temperature such that all electrons are bound in neutral donor states (D^o) at an energy E_d below the conduction band (E_c). Ionized donors (D^+) exist due to photoionization as well as compensation by acceptors (A^-). b) Schematic of the photoionization, drift, and recombination of an electron in an extrinsic photoconductor. The electron is excited by a photon of energy $h\nu$, and travels distance l before recombining at an ionized donor.

Material	Impurity	Type	Binding Energy (meV)	Wavelength (μm)
Si	P	n	45	27.5
	As	n	54	23
	B	p	45	27.5
	Al	p	72	17.2
Ge	P	n	12.89	96.2
	Sb	n	10.29	120.5
	B	p	10.82	114.6
	Ga	p	11.32	109.5
GaAs	Te	n	6	206.6
	S	n	5.87	211.2
	Zn	p	30.6	40.5
	C	p	26.9	46.1

Table 1.1: Binding energies and maximum wavelengths for photoionization of some shallow level impurities in Si, Ge, and GaAs.

considered, the quantum efficiency is given by Equation 1.8. Quantum efficiency is discussed further in section 1.4.

$$\eta = \frac{(1-r)(1-e^{-\alpha w})}{1-re^{-\alpha w}} \tag{1.8}$$

Given η and $\mathcal{G}$ the expected signal current for an incident photon flux Φ is calculated in Equation 1.9, where q is the electron charge.

$$I = q\Phi\eta\mathcal{G} \tag{1.9}$$

Shallow levels in the most commonly encountered semiconductors Si, Ge, and GaAs have a binding energy ranging from a few meV to 10s of meV, as detailed in Table 1.1. The optical response due to the shallow donor and acceptor excitations in Table 1.1 range from 17.2 μm for Al in Si to 211.2 μm for sulfur in GaAs. All these values lie in the far-infrared. The spectral response of an extrinsic photoconductor can be tailored to some extent by choosing the host material and doping species. The spectral response of several Ge detectors and of a GaAs:Si sample is shown in Figure 1.5. Because of its small donor

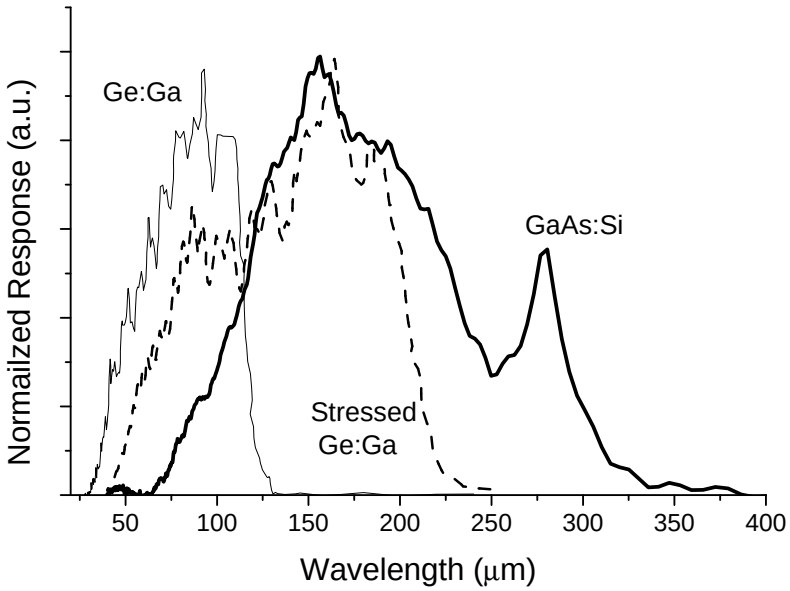

Figure 1.5: Spectral response of common Ge photoconductor detectors and of Si-doped GaAs. The long wavelength response of GaAs:Si is a result of its shallow (6 meV) donor binding energy. All responses have been normalized to have equal peak values. The short wavelength cutoff is instrumental.

electron binding energy, GaAs:Si exhibits photoconductive response at longer wavelengths than Ge. The response of p-type Ge can be extended to longer wavelengths, however, if uniaxial stress is applied to the detector [39]. Uniaxial stress has the effect of splitting the four-fold degeneracy of the Γ_4 valence band edge and reducing the energy difference between the bound acceptor states and the top of the valence band [29].

The signal current of an extrinsic photoconductor depends linearly on its quantum efficiency (Equation 1.9). The most direct and important mechanism for enhancing η is to increase the total number of absorbing centers, or majority dopant atoms, within the semiconductor. Raising the doping concentration will increase the probability of photon absorption. The dopant concentration, and hence the quantum efficiency cannot be increased without limit. At sufficiently high concentrations, the excess carriers associated

with each impurity will be able to conduct even in the absence of light. This so called dark current arises due to hopping conduction between impurity centers. Hopping conduction is discussed in detail in Appendix B. High performance Ge:Ga photoconductors typically contain Ga concentrations of between 1×10^{14} and 3×10^{14} cm^{-3}. These concentrations are below the onset of significant hopping conduction. Such devices maintain dark currents of a few hundred electrons per second or less under standard operating conditions.

1.3 Sources of noise in far-infrared photoconductor detectors

Since far-infrared detectors frequently are used to observe very weak signals, an understanding of noise sources is vitally important. There are four major sources of noise influencing a far-infrared photoconductor detector: Johnson, $1/f$, generation-recombination, and photon noise. The mean square noise current $i(f)$ is the integral of the current spectral density S of each noise component over all frequencies.

$$\langle (i(f))^2 \rangle = \int_0^\infty S_{\mathrm{i}} df \tag{1.10}$$

Johnson (or Nyquist) noise occurs due to the random thermal, or Brownian motion of charge carriers within any electrical conductor. The spectral density for Johnson noise depends on the temperature and the resistance but is independent of frequency. For low frequencies Johnson noise takes the form

$$S_{\mathrm{N}} \propto \frac{k_{\mathrm{B}}T}{R} \tag{1.11}$$

where R is the resistance, k_{B} is the Boltzmann constant, and T is the temperature. Within a frequency band df, a perfect resistor exhibits only Johnson noise with a noise voltage

proportional to the temperature and resistance.

$$V_{\text{Johnson}}(\text{rms}) = \sqrt{4k_{\text{B}}RTdf} \tag{1.12}$$

Johnson noise is generated by the detector readout electronics, normally necessitating that they be cooled.

The origin of $1/f$ noise appears to have a range of origins for different devices. For example trapping of electrons at surface states or deep levels can lead to $1/f$ noise. As its name implies, the noise density is approximately proportional to the current and to the inverse of the frequency.

$$S_{1/\text{f}}(f) \propto \frac{I}{f} \tag{1.13}$$

Generation-recombination (G-R) noise occurs do to the random and continuous excitation and de-excitation of electrons between bound donor states and the conduction band (or, equivalently holes between bound acceptor states and the valence band). In the case of an extrinsic photoconductor, G-R noise arises due to the random drift distance of excited carriers under the applied field. The magnitude of the noise current depends on the density of traps, the current flowing through the detector, and the recombination lifetime. The inverse of the recombination lifetime τ_{r} defines a characteristic frequency above which G-R noise intensity falls off rapidly. At low temperatures, when most free carriers are bound at impurity states, the spectral density of G-R noise is given by Equation 1.14.

$$S_{\text{G-R}}(f) \propto \frac{I^2}{N}\left(\frac{\tau_{\text{r}}}{1+(2\pi\tau_{\text{r}})^2}\right) \tag{1.14}$$

Photon, or shot noise refers to the random arrival of photons at the detector. This is a frequency independent form of noise and represents the minimal value of noise spectral

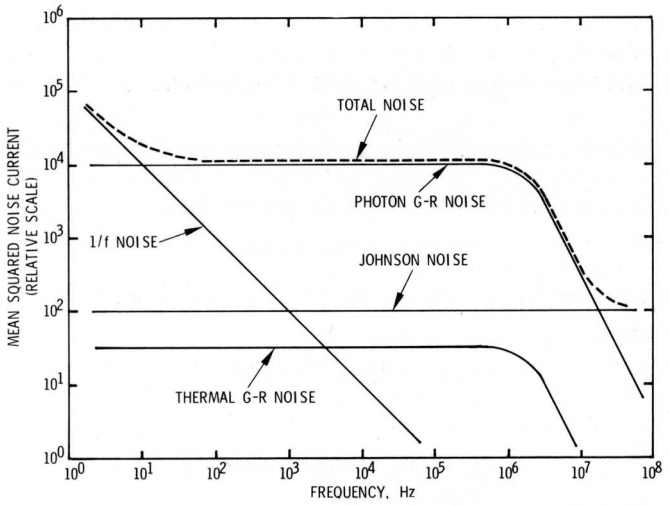

Figure 1.6: The spectral response of various noise sources in an infrared photoconductor, and their sum. After [15]

density that one can achieve in principal with a detector. A detector that is dominated by photon noise is said to be background limited and is known as a background limited infrared photodetector (BLIP). The magnitude of shot-noise current depends on the photon flux and the geometry of the detector and is described by the density function of Equation 1.15. The geometric factor Ω describes the area of the detector and the solid angle visible to the source.

$$S_{shot} \propto \Phi\Omega \tag{1.15}$$

The spectral response of the total noise current with its components is displayed in Figure 1.6.

1.4 Detector figures of merit

In order to gauge the performance of a detector or detection system, several figures of merit have been developed that allow comparison between different types of devices.

The figures of merit discussed here are widely used within the far-infrared astronomy and detector development community.

Quantum Efficiency

Quantum efficiency, which was briefly discussed in Section 1.2.2, is defined as the detector output generated per incident photon. For a photoconductor detector, the quantum efficiency is interpreted as percent of incident photons that cause a bound electron (hole) to be excited to the conduction (valence) band and drift under an applied voltage. For a bolometer, the quantum efficiency represents the percent of photons absorbed within its absorber. In both cases, the quantum efficiency of a device depends upon the device geometry and the properties of the material from which it is fabricated. For example, the quantum efficiency of an extrinsic semiconductor photoconductor detector increases if the majority doping concentration is increased. η also increases if the length of the detector is increased in the direction in which photons travel through it.

Responsivity

The responsivity of a detector is a ratio of the detector output signal to the power of the incident photon stream. For a photoconductor, responsivity is therefore defined as the signal current generated under the applied bias divided by the photon power. The incident power is the number of photons arriving per second Φ multiplied by the quantum efficiency η and the energy of each photon (hc/λ, where h is Plank's constant, c is the speed of light, and λ is the wavelength). The signal current for a photoconductor is given by Equation 1.9. Therefore the responsivity, in A/W, is written as

$$\mathcal{R} = \frac{\eta \mathcal{G} q \lambda}{hc} \tag{1.16}$$

The responsivity is an important figure of merit determining the signal strength of a detector but is of little meaning unless compared with the noise.

Noise Equivalent Power (NEP)

NEP is given by the incident signal power that is necessary to create a signal to noise ratio of 1 for a bandwidth of 1 Hz and has units of $\frac{W}{\sqrt{Hz}}$. In terms of the currents due to the i noise sources and the responsivity, the NEP is given by.

$$NEP = \frac{1}{\mathcal{R}} \left(\sum_i I_{\mathrm{n}}^2 \right)^{1/2} . \tag{1.17}$$

The NEP should be specified in combination with the photon wavelength being detected, the incident power, and the measurement frequency of the device. The more sensitive a detector is, the smaller is its value of NEP. Frequently a figure of merit known as the detectivity (D), which is the inverse of the NEP, is used. The detectivity is larger for more sensitive detectors.

The total noise current is the sum of the root mean squares of all noise contributions (see Section 1.3). The NEP of a detector dominated by photon noise (BLIP) is given by

$$NEP_{\mathrm{BLIP}} = \frac{2hc\Phi^2}{\lambda\eta^2} . \tag{1.18}$$

When the noise is background limited, the NEP is only a function of the quantum efficiency for a given wavelength. This is because photon noise is not associated with the quality of the detector.

1.5 A comparative analysis of bolometers versus extrinsic photoconductors

The most obvious disparity between bolometers and photoconductors from a detector standpoint is that bolometers can be used for all wavelengths in the far-infrared, while photoconductors have a limited spectral range of operation. Different types of extrinsic photoconductor detectors, with varying host and impurity materials, can be used to cover a large portion of the far-infrared; however currently none exist which are sensitive to radiation beyond approximately 220 μm. Despite this disadvantage, extrinsic photoconductor detectors are often preferred for use in high-altitude and space telescopes. For operation in low background conditions, such as observations from space telescopes, bolometers require extreme cooling, below 1K, to achieve comparable NEP to those of photoconductor detectors. The small amount of dark current that flows in a high quality Ge:Ga, background limited photoconductor near 1.5 K allows the detection of extremely weak signals. This difference in operating temperature means that a far more practical cooling system is required onboard a space telescope using photoconductors. Photoconductor detectors also have the advantage of the availability of cold, low noise, integrating pre-amplifiers that form the first low noise stage of the electronic amplifier.

Photoconductor detectors are desirable compared to bolometers for the production of high density arrays. The integration of bolometers with their readout electronics into large arrays is still an unsolved problem due to the complex assembly of each detector pixel. Also, the lack of low noise multiplexed readout electronics prohibits large bolometer array sizes. Relatively large format arrays of far-infrared photoconductors and their complementary

readout electronics have been produced. The 32×32 Ge:Ga array used onboard the Spitzer telescope [30] is a good example. Additionally, two 32×16 stressed Ge:Ga arrays, each operating over a different wavelength band, have been constructed for use on the Herschel Space Observatory, expected to be launched in 2007.

1.6 The blocked impurity band detector

Blocked impurity band (BIB) detectors are a class of photoconductor infrared detectors that have the potential for significantly higher performance compared to a standard extrinsic detector of the same material. The BIB device, first conceived and demonstrated by Petroff and Stapelbroek [53], is a modification of a bulk photoconductor. It consists of a doped absorbing semiconductor layer in series with a thin high-purity layer. The high-purity layer blocks dark current associated with hopping and impurity band conduction in the doped layer.

GaAs and Ge BIB devices have the potential to offer response at very long wavelengths, where currently only bolometers can be used, without sacrificing the higher sensitivity at operating temperatures above 1 K of standard photoconductor detectors. Arrays of BIB detectors have been realized using doped silicon for detection at higher energies ($\geq$ 333 cm^{-1} or 30 μm) [52, 44, 19]. Figure 1.7 shows a 128×128 pixel array that is part of the Multiband Imaging Photometer currently onboard the Spitzer Telescope (MIPS) [30], that is used to detect radiation near 417 cm^{-1} (24 μm). The Si BIB devices and their corresponding readout electronics operate at a relatively easily obtainable temperature of 6 K. BIB detectors made from GaAs are expected to operate according to the general

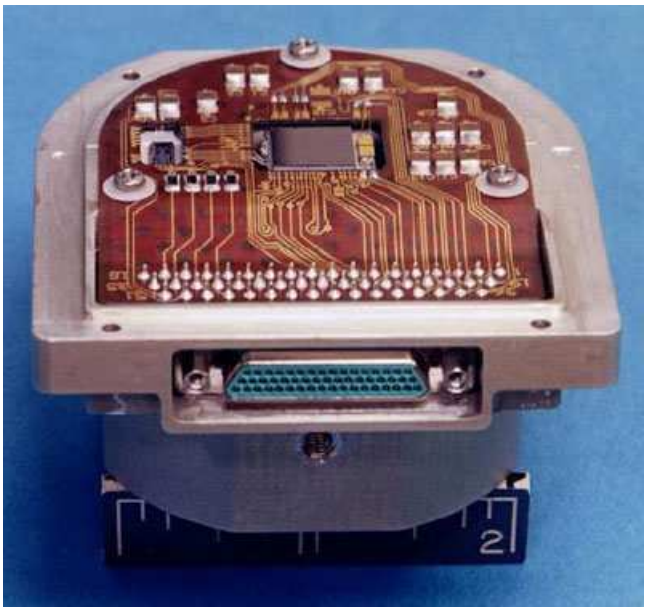

Figure 1.7: The 128x128 Si BIB array with associated readout electronics currently onboard MIPS, an instrument of the Spitzer space telescope. After [32].

model developed for BIB detectors. Because of the much reduced donor binding energy, at correspondingly longer wavelength and lower temperatures, they should be able to detect photons with wavelengths exceeding 300 μm.

1.6.1 Characteristics of the BIB detector

As discussed in earlier, the BIB detector consists of a doped absorbing layer coupled with a high purity blocking layer. The blocking layer effectively suppresses the contribution of hopping conduction to the dark current. This allows for an increase in the absorbing region doping concentration compared to a standard photoconductor, in which the concentration is limited to lower values by the onset of hopping conduction. The increased dopant concentration of the absorbing layer in a BIB detector compared to a standard bulk photoconductor greatly enhances the linear optical absorption coefficient α of the device. With a

larger α, a smaller absorbing layer dimension in the direction of the photon flux is require to yield equal photon absorption. The resulting reduced detector volume makes the BIB detector less susceptible to interactions with high energy cosmic rays. The higher doping of the BIB detector also leads to response at longer wavelengths, a result of the formation and broadening of an impurity band. At higher impurity concentrations the dispersion of bound energy levels pushes the density of states closer to the conduction band.

Another advantage of BIB detectors is that the photoconductive gain is no less than unity. This advantage is discussed in detail in Section 1.6.2. Also, like standard photoconductors, they can be relatively easily fabricated into large arrays using standard photolithographic techniques. The integration of BIB detector arrays with their readout electronics is accomplished using the so-called "flip-chip" design [45]. In this technique the BIB detectors are fabricated on an infrared transparent substrate with both the absorbing and blocking layer contacts on the same side of the device. This is accomplished by creating a buried contact by ion-implantation prior to growth of the absorbing layer. The cross-section of this BIB detector structure is shown in Figure 1.8(a). The readout electronics are fabricated on a separate substrate wafer. The electrical contacts of the readout align with those of the BIB detector array. Small pieces of indium known as "bumps" are placed over the contacts of both the readout and BIB detector wafers. The two wafers are then pressed together to form the contacts between the detectors and the readout electronics. Photons enter the active region of the BIB detectors after transmitting through the high-purity substrate. This process is illustrated in Figure 1.8(b).

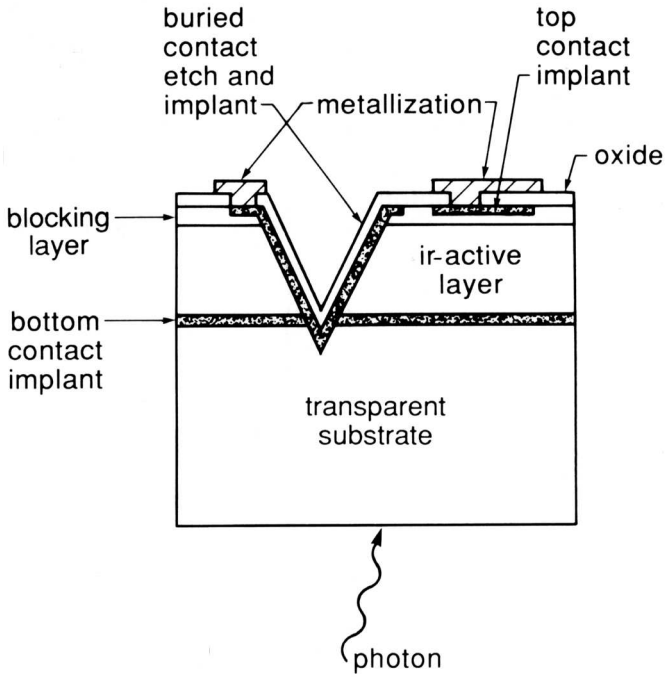

(a)

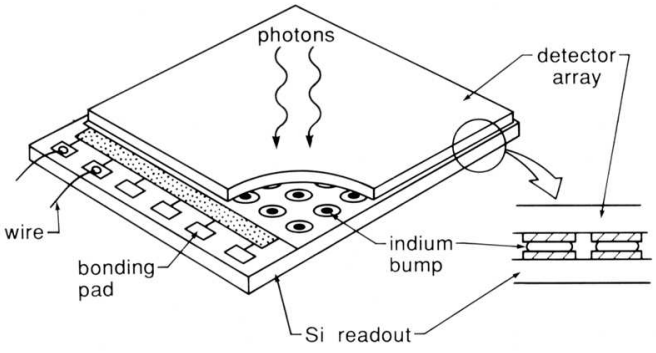

(b)

Figure 1.8: a) Cross-section of a Si BIB detector with both blocking and absorbing layer contacts on the front side of the device. b) Schematic of a Si BIB detector array that has been integrated with its readout electronics using the "flip chip" technique. After [57]

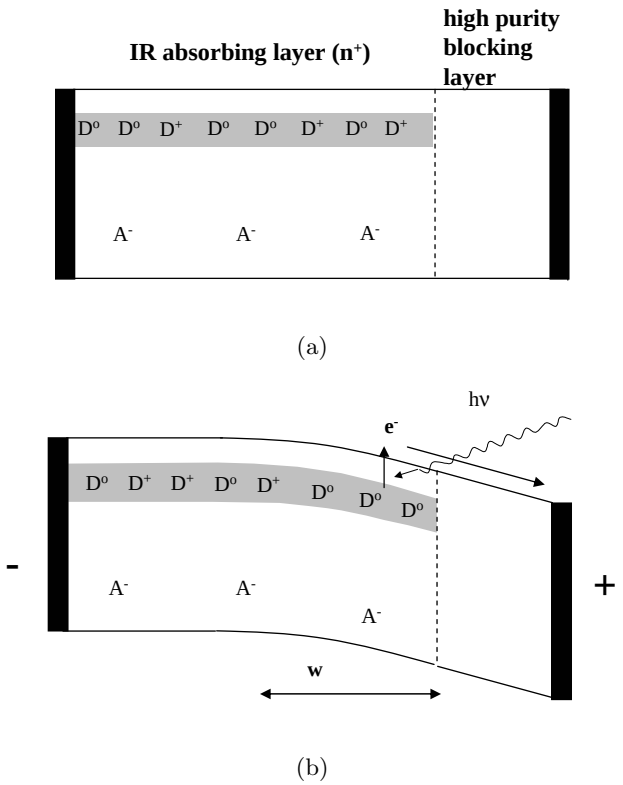

Figure 1.9: Band diagram of a BIB detector a) unbiased, b) with an applied bias a depletion layer (w) forms.

1.6.2 BIB detector theory

The energy band diagram for a BIB detector with no external bias is shown in Figure 1.9(a). The n-type absorbing region contains mostly donors with a smaller number of acceptor impurities. The majority doping concentration is high enough such that hopping conduction within an impurity band dominates the electrical characteristics of the semiconductor at low temperatures. At low temperature (< 2 K for GaAs), most electrons are bound within the impurity band. Ionized donors still exist at least at a concentration of $N_d^+ = N_a^-$ due to the presence of compensating acceptors. In the blocking layer very few donor atoms are present and hence no impurity band forms. This leads to a great reduc-

tion in hopping conduction compared to the absorbing layer. The electrons bound within the impurity band cannot conduct through the high-purity blocking layer. The blocking layer interrupts the conduction path for dark current as long as the impurity band does not overlap with the conduction band. Any current flowing through the device must be due to electrons that have been excited into the conduction band either thermally or optically.

If a positive bias is applied to the blocking layer contact in the absence of light (Figure 1.9(b)), electrons within the impurity band travel toward the interface between the absorbing and blocking layers. The ionized donors then capture free electrons and become neutral. Ionized acceptors, present at very small concentrations, are stationary, and form a negative space-charge region. As a result, the only charge present near the interface between the absorbing and blocking layers is due to ionized acceptors. The ionized acceptors therefore determine the depth of penetration of the electric field into the absorbing region. The depletion thickness and electric field within the BIB device can be solved by using the Poisson equation if the charge distributions for the blocking and absorbing layers are given. The depletion-region width and electric field of an n-type BIB detector are given by Equations 1.19 and 1.20, respectively,

$$w = \sqrt{\frac{2\epsilon\epsilon_{\mathrm{o}}(V_{\mathrm{a}} - V_{\mathrm{bi}})}{eN_{\mathrm{A}}} + b^2} - b \tag{1.19}$$

$$E(x) = \frac{qN_{\mathrm{a}}}{\epsilon\epsilon_{\mathrm{o}}}(w - x) \qquad . \tag{1.20}$$

Here ϵ is the relative dielectric constant, ϵ_{o} is the permittivity of free space, V_{a} is the applied bias, V_{bi} is the built in bias, e is the electron charge, N_{A} is the compensating acceptor impurity concentration, and b is the blocking layer thickness.

When exposed to light, free electrons generated by photons that have been ab-

sorbed within the depletion region will be collected at the positively biased contact. Electrons excited in the neutral region will recombine with a nearby ionized donor. The ionized donor charge state travels to the negative contact. The combined motion of the positive donor state and the electron results in a unity photoconductive gain. If the detector bias is high enough such that electron impact ionization becomes likely, the photoconductive gain will be greater than unity.

In order to detect a large percentage of the incident photons (Equation 1.7), it is necessary to achieve a value for the product of the linear absorption coefficient α and the depletion layer width w, $\alpha w \geq 2$. This, in turn, requires an appropriate depletion region width. As shown in Equation 1.19, the depletion region thickness is determined by the applied bias and the minority acceptor concentration within the device. The minimization of the compensating acceptor concentration is, therefore, of the greatest importance in achieving high quantum efficiency. For example, in order to detect greater than 50% of the incident flux at 37 cm^{-1} (270 μm), a GaAs BIB detector (neglecting surface reflection) with an active region majority doping of 6.7×10^{15} cm^{-3}, a 5 μm blocking layer, and an applied bias of 300 mV, must have an acceptor concentration below 1.0×10^{12} cm^{-3}. This corresponds to an acceptor to donor compensation ratio of 0.00014.

GaAs is an especially attractive material for BIB production because of its low donor electron binding energy (6 meV). This means that a bulk GaAs photoconductor would be sensitive to radiation well below 45.5 cm^{-1} (above 220 μm), the limit of detection by state of the art, stressed Ge:Ga photoconductors [58]. In an actual BIB detector, the response is expected to extend to even longer wavelengths due to impurity band formation

and broadening. For optimal BIB detector performance, the active region must be doped to a sufficiently high concentration for efficient absorption and to widen the impurity band, giving longer wavelength response. Increasing the doping concentration, however, will require lower operating temperatures to reduce dark current generated by thermally excited carriers. At very high doping, the impurity band will overlap with the conduction band, leading to a failure of the device.

Chapter 2

GaAs Liquid-Phase Homoepitaxy

2.1 Fundamentals of liquid-phase epitaxy

Liquid-phase epitaxy (LPE) was one of the first growth techniques used to produce semiconductor thin films and heterostructures. Semiconductor LPE involves the absorption and subsequent precipitation onto a substrate of a solute material from solution. During LPE, the source material which is to be deposited is introduced into a metallic solvent that is held inside a crucible, and contained within a controlled atmosphere. A substrate, which may be the same (homoepitaxy) or different (heteroepitaxy) from the material to be deposited, is at this stage isolated from the solution. The entire system is heated, which causes the solubility of the source material in the solvent to increase. Once the solvent has become saturated with the source material at the initial growth temperature, the solution is transported to the substrate. Solution transportation can be achieved with a variety of techniques, including tipping onto the substrate, dipping of the substrate into the solution, sliding over the substrate, or spinning of the solution over the substrate. After

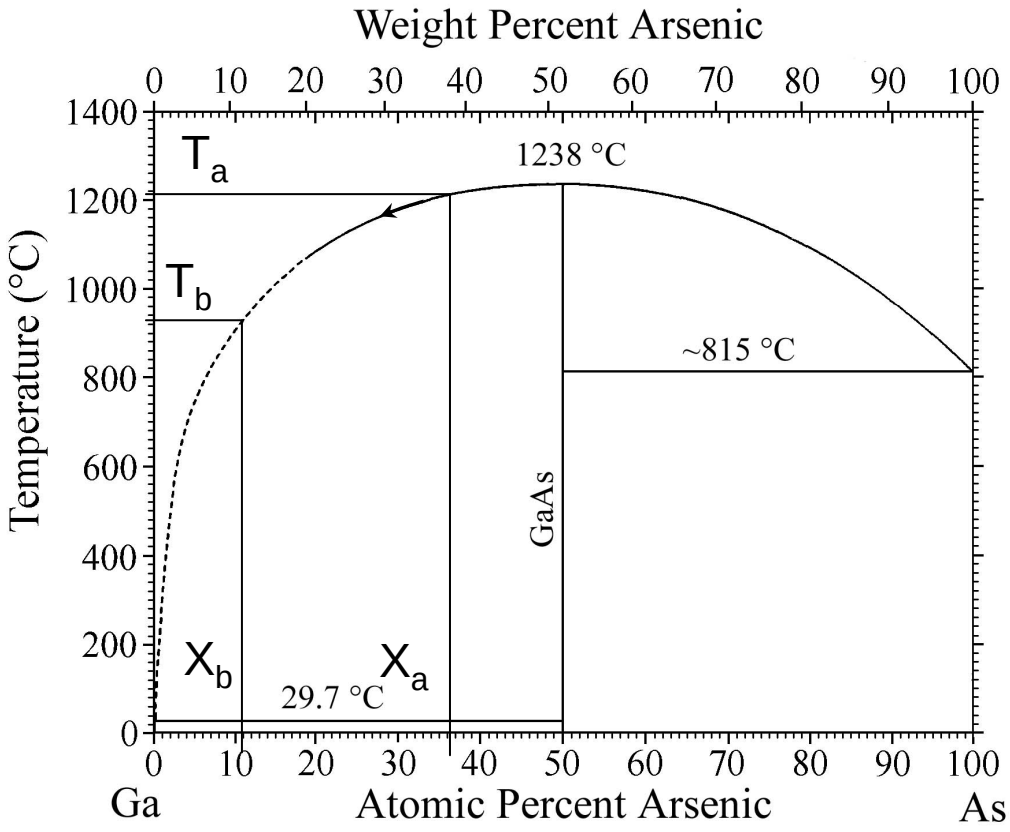

Figure 2.1: Phase diagram showing the reduction of the As solubility in liquid Ga as the temperature is decreased. Modified after [46]

transportation to the substrate, the temperature is lowered, which reduces the solubility of the depositing material in the metal solvent. The solute material is driven out of solution as the solubility decreases, depositing preferentially onto the substrate.

The LPE process for the case of GaAs can be observed by following a schematic of the Ga-As phase diagram (Figure 2.1). In the Ga-As system, GaAs is a line compound at 50% As concentration for all temperatures except near the melting point (1238°C). Since GaAs is grown out of a Ga metal solution, only the Ga rich side of the phase diagram is of importance. If ample GaAs is added to pure Ga at temperature T_{A} the equilibrium

concentration of GaAs that will dissolve in the Ga is X_{A}. At temperature T_{B} there is a significantly smaller equilibrium value of GaAs dissolved in the Ga (X_{B}) as the solubility has decreased. As the temperature of the system is lowered, the Ga+As solution becomes supersaturated with As, forcing some GaAs to precipitate out of solution. This process will continue until the remaining Ga solution contains the equilibrium concentration of As for the final temperature. The composition of the liquid will follow the liquidus line indicated by the arrow. The number of molecules of GaAs ejected from the solution due to the temperature gradient is given by equation 2.1,

$$N_{L\rightarrow S} = \frac{(X_{\mathrm{A}} - X_{\mathrm{B}})V\rho}{WN_{\mathrm{a}}} \tag{2.1}$$

where V is the volume of solvent (Ga), ρ is the solvent density, W is the solvent molecular weight, and N_a is Avogadro's number. The GaAs molecules can form nuclei either homogeneously (within the Ga+As melt) or heterogeneously on the GaAs surface. Nucleation theory predicts that nucleation will occur preferentially at the substrate or on the surface of the solution because of the increased energy associated with creating excess surface from homogeneous nucleation. It has been experimentally determined for the case of the Ga-As system that a supercooling of approximately 10 degrees at 800°C is required before homogeneous nucleation begins to occur within the melt [6].

2.2 Advantages of LPE GaAs growth

Throughout the 1960s and 70s, LPE was the primary growth technique used for industrial production of optoelectronic devices such as lasers and light emitting diodes. This was mainly due to the relative simplicity of reactor designs. In recent years LPE has largely

been replaced in such industrial processes. Today, production of GaAs and other III-V semiconductor thin film based devices is dominated by the vapor phase epitaxiy (VPE), and to a lesser extent molecular beam epitaxy (MBE). These growth techniques have been highly developed to reproducibly generate flat, high quality, and very uniform thin films, with a high throughput as demanded by the microelectronics industry. LPE, however, offers specific advantages over MBE and VPE growth of compound semiconductors. First, LPE can produce very thick films, up to 100μm or greater, depending on the amount of solvent used and the growth start temperature. Second, films of ultra-high-purity can be produced because of the segregation of most impurity species out of the solid phase during growth. Such thick, high-purity GaAs films are particularly important since the bulk material cannot be grown with the purity of Si or Ge crystals.

Another major advantage of the LPE technique over VPE and MBE growth is the low cost and simplicity of the system design. A LPE growth process generally does not require highly toxic gases or metal-organic solutions, as is the case for GaAs vapor growth. It also does not require ultra-high vacuum conditions as required for MBE growth.

LPE is particularly well suited to GaAs growth because the component Ga can be used as a liquid metal solvent. Elemental semiconductors such as Si or Ge must be grown out of other metal solutions such as In or Pb which can incorporate into the film and are not available in as high purity as Ga. While LPE films cannot match the surface quality and thickness control of those grown by the MBE and VPE techniques, the high thickness and purity requirements of far-infrared detectors, such as the GaAs Blocked-Impurity-Band (BIB) detector necessitate film growth from the liquid phase.

2.3 Microscopic theory of GaAs LPE growth

The major driving forces which dictate the nucleation and growth of a solid out of solution, as occurs during LPE growth, are the formation of a lower energy final phase, the addition of free surface, and the creation of stress due to misalignment with the substrate. For the case of GaAs homoepitaxy, stress is not a factor because the substrate has the same lattice constant as the depositing film. If the Ga is saturated with As at concentration $C(T)$, at an initial growth temperature T, and is then allowed to cool by ΔT, the system will become supersaturated. The equilibrium concentration of solute in solution is given by the liquidus line, $C_{\mathrm{L}}(T)$. The degree of supersaturation β is defined as [6]

$$\beta = \frac{C(T) - C_{\mathrm{L}}(T)}{C_{\mathrm{L}}(T)} \tag{2.2}$$

The gain of free energy per unit volume $\Delta G_{\mathrm{crystal}}$, if GaAs is rejected from the liquid and deposited in crystalline form to reduce the supersaturation, is given by Equation 2.3, where R is the universal gas constant.

$$\Delta G_{\mathrm{crystal}} \sim RT\beta \tag{2.3}$$

Therefore the total free energy for growth out of a solution is given by

$$\Delta G = -S(\theta)(\frac{4}{3}\pi r^3 \Delta G_{\mathrm{crystal}} + 4\pi r^2 \gamma_{\mathrm{sl}}) \tag{2.4}$$

$$S(\theta) = \frac{(2+\cos\theta)(1-\cos\theta)^2}{4} \tag{2.5}$$

where r is the radius of a hemispherical nucleus of solid material forming on the substrate, γ_{sl} represents the surface energy for the interface between the solid and liquid phases, θ is the wetting angle between the nucleus and the substrate. If the surface of deposition is

perfectly flat, the balance between the thermodynamic driving force and the creation of new surface places restrictions on the size of the nucleus that is stable. Nuclei below a critical radius will dissolve back into solution.

The initiation of crystal growth on a perfectly flat substrate requires a large amount of supersaturation of the solution to overcome the nucleation barrier associated with the addition of free surface (Figure 2.2(a)). Burton [16] has estimated that supersaturation of approximately 50% is required before significant nucleation can occur. Rapid crystal growth, however, is known to occur at supersaturation levels of 1% or less. These numbers are reconciled if surface defects, which provide initial growth steps that facilitate nucleation, are considered. During lateral growth, an atom that attaches itself to a growth step does not increase the surface energy of the system, as much as a single atom on a flat surface. Furthermore, an atom that attaches to a corner has an even smaller increase in area, as shown in Figure 2.2(b).

The same principles apply during nucleation on surface defects, such as surface-terminating screw dislocations and misorientation steps. Screw dislocations that terminate at the surface and have a Burgers vector perpendicular to the 2D lateral growth direction act as nucleation sources. Figure 2.3(a) shows how a step formed by such a dislocation can lead to lateral growth. The spiral procession of the growth step around the dislocation core is shown schematically in Figure 2.3(b). As atoms attach to the step, growth will proceed in a spiral direction around the core of the dislocation. This type of growth leads to the formation of growth pyramids composed of small steps. Growth pyramids have been identified by decoration of the steps with epitaxial Ge (Figure 2.4).

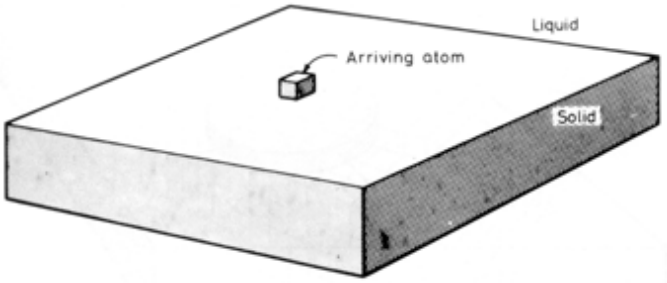

(a)

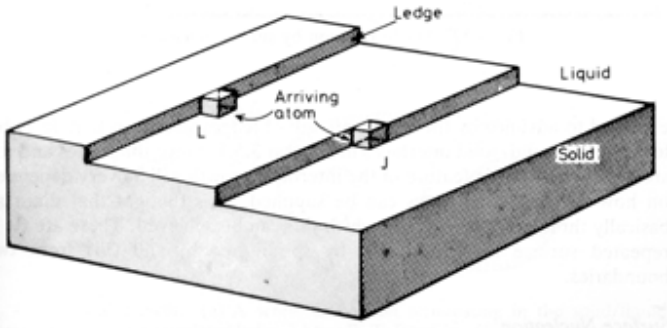

(b)

Figure 2.2: (a) The addition of an atom to a perfectly flat surface (a) creates significantly more surface energy than addition to a ledge. Addition to a corner creates no additional surface energy (b). Growth steps enhance nucleation and film growth. After [23]

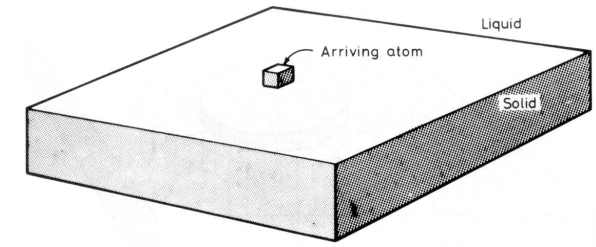

(a)

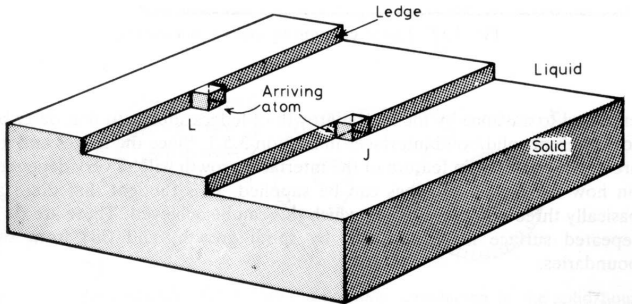

(b)

Figure 2.3: Growth originating at a surface-terminating screw dislocation. (a) The dislocation provides a nucleation step for atoms arriving at the surface. After [54]. (b) Growth proceeds in a spiral direction, originating at the dislocation core. Growth shown chronologically from step 1 to step 6. After [18].

Figure 2.4: Scanning electron microscope image of the spiral growth steps around a screw dislocation nucleus, highlighted by Ge epitaxy. After [10].

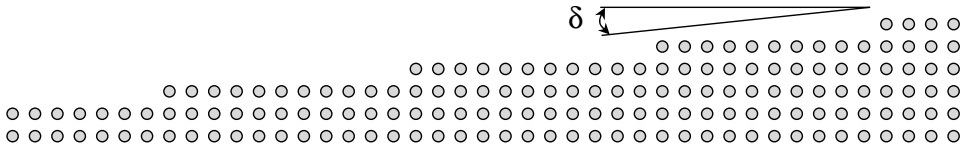

Figure 2.5: Schematic of misorientation steps on a crystalline surface due to miscut angle δ with respect to a major plane

If a crystal is not perfectly oriented with respect to a crystalline plane, misorientation steps will exist at the surface (Figure 2.5). The size of and spacing between the steps depends on the degree of misorientation, which can be represented by an angle δ off of a major crystalline plane. For high degrees of misorientation, the steps will be larger and more closely spaced than is the case for less misorientation. Misorientation steps act as nucleation sites in the same way as surface-terminating dislocations do, except growth proceeds laterally, instead of in a spiral manner.

According to Astles, liquid-phase epitaxial growth can been broken down into three stages: nucleation, surface attachment, and solutal transport [6]. Each of these steps is the result of a separate thermodynamic driving force and any of them may be the determining step of the growth rate depending upon the growth conditions. During nucleation, atoms that are absorbed onto the growth interface attach to the substrate and diffuse together to form clusters. As shown above, the driving force for nucleation evolves from the reduction in free energy from crystallization, $\Delta G_{\text{crystal}}$, the magnitude of which is determined by the degree of supercooling of the solution. In order to enhance $\Delta G_{\text{crystal}}$, and hence the growth rate during the nucleation stage, the solution is typically cooled by 3-5 degrees prior to transportation to the substrate, as described above. During surface attachment, the clusters or nuclei grow together and create a continuous film, driven by the reduction

in free energy associated with the minimization of surface area. Smaller nuclei diffuse toward and join with larger ones, reducing the surface energy. Solutal transport involves the transport of atoms between the growth interface and the solution. As the film grows it will cause a reduction in the concentration of As atoms in the solution near the interface. The concentration gradient results in a reduction of the chemical potential for As in the low concentration region, making it energetically favorable for more As to flow towards the interface. This process becomes kinetically limited at low temperature, however, when the diffusion length of As atoms in the Ga solution is small.

2.4 Surface morphology of LPE grown films

Bauser had divided LPE growth mechanisms into several categories that result in different surface morphologies and depend upon the orientation and dislocation density of the substrate [8]. Each of these mechanisms has been demonstrated using LPE growth of GaAs on a spherically shaped substrate, which incorporates a range of different crystal orientations into the same growth run. The growth mechanisms identified were facet growth, dislocation controlled facet growth, near-facet growth, terrace growth, and terrace-free growth. In the absence of dislocations or substrate edges, atoms that arrive at the substrate will preferentially attach to surface misorientation steps. When the substrate is highly oriented, few misorientation steps exist, leading to very slow nucleation and growth. This case is demonstrated at the topmost point of Figure 2.6(a). The growth rate may be increased by enhancing the solution supercooling to overcome the lack of nucleation sites. This leads to increased homogeneous nucleation in the melt as well as the inhomogeneous

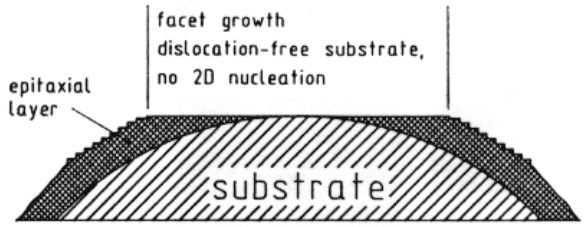

(a)

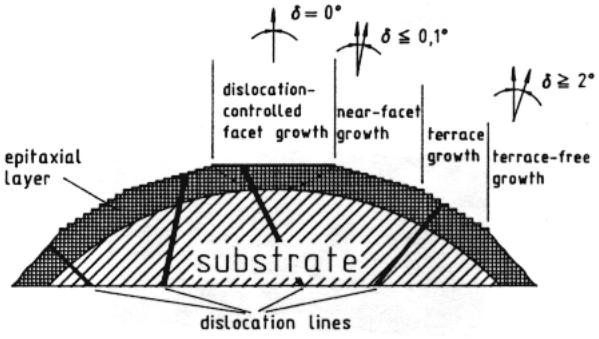

(b)

Figure 2.6: Schematic showing the identified growth modes as a function of substrate misorientation for LPE GaAs films grown on a spherically polished substrate with (a) no dislocations, (b)surface terminating dislocations. After [8].

inclusion of impurity atoms in the film, and is therefore undesirable for device production.

Facet growth in the presence of dislocations is the most desirable growth mechanism, as it produces a nearly atomically flat surface. It occurs on substrates that are very highly oriented ($\delta \leq 0.05°$) to a major crystalline plane, and is demonstrated at the topmost point of the spherical substrate of Figure 2.6(b). As described above, growth proceeds in a spiral motion around the dislocation core, forming pyramid structures. As growth proceeds the pyramids extend and eventually coalesce to form a flat film. Bauser et al., by noting the positions of etch pits on an LPE film surface, confirmed that dislocations act as the source for the growth pyramids [9].

At slightly higher degrees of substrate misorientation ($\delta \leq 0.1°$), the dominant growth mode has been termed near-facet growth. In this circumstance, growth is initiated at widely spaced misorientation steps on the surface that are typically of a few atomic dimensions high [8]. The films produced by near-facet growth are not as flat as dislocation controlled facet growth due to the distribution of misorientation step size. In general they are, however, flat enough to be suitable for use in electronic device applications.

Growth on substrates that are misoriented by $0.1° < \delta < 2°$ from a low-index plane results in terrace growth. Substrates of relatively high misorientation contain a large number of randomly spaced surface steps of varying height. The steps will advance parallel to the interface as more atoms are added. The continuous formation and growth of new steps results in crystal growth perpendicular to the interface, however the velocity of an advancing growth front depends on its height, with the tallest ledges advancing the slowest. In Figure 2.7 three growth steps are displayed, with their velocities indicated by the length

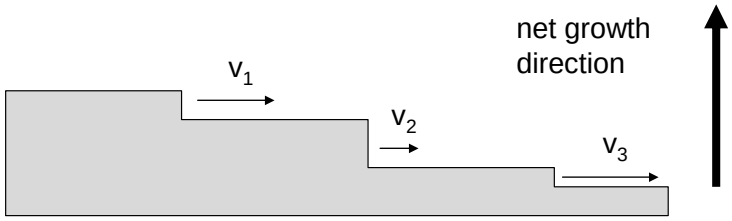

Figure 2.7: The sum of advancing 2D growth steps leads to a net growth in the vertical direction. The velocity of a growth steps is inversely proportional to its height.

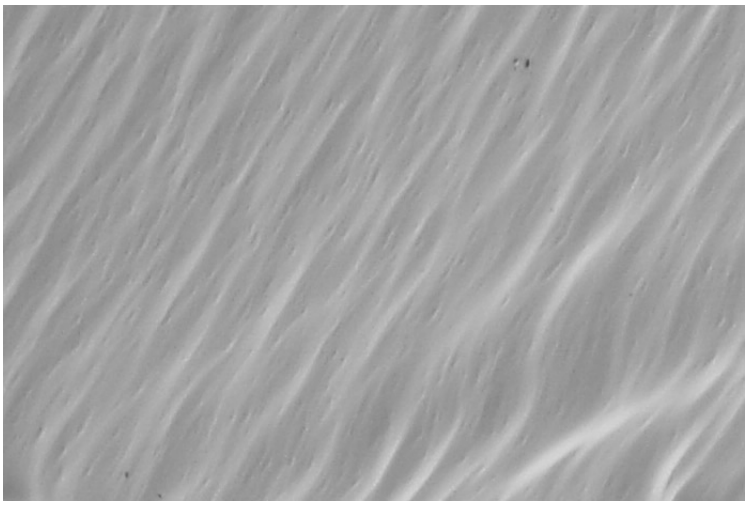

Figure 2.8: Optical micrograph of an LPE GaAs film with terraced surface morphology

of the corresponding arrows. The relatively short growth front, moving with velocity v_1 will extend faster than the large one beneath it until the two have merged to form an even larger front in a process known as "step bunching" [8]. In the terrace growth mode, step bunching is severe due to the presence of misorientation steps of widely varying heights. As growth is continued, the height and lateral dimensions of the step bunches increase until they are structures of macroscopic dimensions, known as terraces. Terraces consist of a flat section, or tread, and a steep incline, or riser (Figure 2.8). Besides leading to a rippled surface morphology, terraces are a major cause of inhomogeneous impurity incorporation,

as impurity atoms tend to accumulate on the steep riser section of the terrace.

Terrace-free growth is observed if the substrate is very highly misoriented from a low index plane ($\delta > 2°$). For such large angles, the formation of terraces has been predicted to be unstable, and a smooth morphology is expected.

2.5 LPE system design and growth parameters

Variables in the design of a LPE growth system include the type of crucible material, ambient gas and containment materials. Each of these must be chosen to satisfy the necessary restraints on film purity, thickness, and morphology. Graphite is the most common crucible material for GaAs LPE due to its availability in high-purity, ease of machining, and thermal stability. Graphite can be baked at high temperatures to remove volatile impurities. Due to the porous structure of polycrystalline graphite, impurity species can become trapped in the crucible and create a quasi-continuous source of contamination. Additionally, impurities can intercalate between the atomic sheets of single crystal graphite. It is therefore essential for high-purity growth that the crucible be maintained in a clean environment, such as under vacuum, at all times. Other crucible materials, including alumina and boron nitride have been investigated [47] however films grown from these crucibles were found to be not as pure as graphite grown films. Quartz is the usual choice for the reactor tube because of its availability in very high-purity, as demanded by the semiconductor industry, and its mechanical stability up to high temperatures ($\sim 1400°$C). Hydrogen is typically used as the ambient gas because it helps to reduce oxides on the substrate and surface of the Ga solution. Despite its advantages, the SiO_2-H_2 system is believed to cause Si contamination

in GaAs LPE films by the reduction of the quartz into SiO. Argon-hydrogen mixtures have been explored as a way to minimize the hydrogen-quartz interaction [21].

The cooling rate is the most important growth parameter for LPE film growth. The most common technique uses a temperature ramp that may include several different cooling rates during one growth run. This method allows for the growth of very thick films, particularly when the cooling rate is slow, allowing time for the solute to diffuse to the solution-substrate interface. In another technique, known as "step growth", the temperature of the solution is lowered before transportation to the substrate. Upon contact with the substrate, spontaneous nucleation and growth will occur. This process occurs at a single temperature, leading to improved film uniformity. The degree of supercooling prior to growth is limited however, by homogeneous nucleation within the melt, which will occur to a large extent as the solution temperature is dropped. This limits the thickness of the resulting film, since the growth is driven by the amount of supercooling. Step and ramp growth are frequently combined to achieve films that are thick but of better uniformity than achievable with ramp growth alone. This is done by an initial supercooling of the solution, followed by transportation to the substrate and subsequent temperature ramp.

The different versions of LPE that have found wide use are defined by their solution transport mechanism. The various forms of solution transportation that have been developed include tipping, sliding, dipping, and rotation. The tipping and dipping boat systems are preferred for achieving the highest purity films because of the simplicity of the apparatus, which requires few mechanical parts with a minimum of exposed surface area. For tipping growth the solution is isolated from the substrate on one side of a crucible

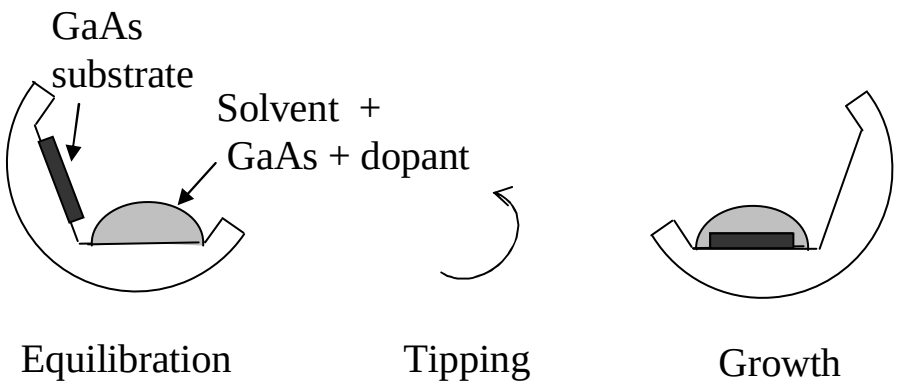

Figure 2.9: Solution transportation in a tipping boat LPE system

that can be tilted to allow it to flow over the substrate. This process is illustrated for the case of GaAs in Figure 2.9. The sliding boat is the system of choice for LPE of III-V based LEDs and lasers due to its potential for massively parallel growth and smooth surface morphology. In this technique, the solution or solutions (for multilayer growth) are held in graphite chambers that can slide horizontally over a graphite plate. The substrate and source material rest inside an inlet in the graphite plate such that its surface is flush. A solution is first slid over the source material so that it can dissolve it until saturation. It is then slid to the substrate, where the temperature is lowered, resulting in growth. The process of sliding over the substrates results in very flat final surfaces because all of the solution is removed rapidly. The sliding boat system, however, suffers from contamination due to free elemental carbon and other impurities that are generated in the sliding process. Rotational or centrifuge LPE transports the solution by a rapid spinning of the containing crucible. This technique has the potential for production of high-purity and multilayer films but is still useful for growth over large areas. Centrifuge LPE of GaAs is currently under

development [41]. Both the sliding boat and centrifuge LPE systems can be used to grow multiple films of different compositions in the same growth run. This is a great advantage in the production of semiconductor optoelectronic devices, where alternating layers of n-type and p-type doping are required.

2.6 Impurity incorporation in GaAs LPE

Impurities contained within the melt invariably enter the epitaxial film during growth. The extent to which an impurity species incorporates depends on a number of factors including the valence state and atomic size. The preference of an impurity to enter the growing film is given by its segregation coefficient k, which is defined as the ratio of the concentration of the impurity in the solid phase to the concentration in the liquid phase. The segregation coefficient for most shallow donors and acceptors in GaAs has been determined to be much less than 1, with exceptions for Se, Te, and S [6]. The preference of most impurities to remain in the liquid phase is a great advantage for the production of ultra-high-purity GaAs films by LPE. Acceptor type dopants such as Zn, Ge, and C are not found to efficiently transfer from the liquid to the solid phase. While the donors Se and Te have segregation coefficients close to or greater than 1, these do not present problems for high-purity growth because they are usually dilute within the metallic Ga solution used for LPE growth. Sulfur, which also has a segregation coefficient close to 1, is relatively volatile and has been shown to be effectively removed by baking of the solution prior to growth [6]. GaAs LPE films can be grown with much higher purity than bulk GaAs, which is typically grown by the Liquid Encapsulated Czochralski (LEC) or Vertical Gradient Freezing (VGF)

techniques. This is mainly due to the lower growth temperature of LPE films, which is typically 800°C or less, compared to bulk growth at the melting point of GaAs (1238°C).

For the production of doped films, a controlled amount of impurities may be added to the melt by the use of doped bulk GaAs of known concentration. In general, the impurity concentration in the resulting film is directly proportional to the concentration in the melt, allowing accurate doping of LPE GaAs films. For tellurium doping during LPE growth, substitutional incorporation can be reproducibly achieved between approximately 5×10^{14} and 1×10^{21} cm^{-3}.

Chapter 3

GaAs LPE experimental methods and results

3.1 Design of the LPE reactor

The growth of GaAs films was performed using a tipping-boat liquid-phase epitaxy system. A schematic drawing of the LPE system is shown in Figure 3.1. The key components of the system are:

- Silica outer process chamber
- Silica inner cantilever rod (rotates to perform tipping)
- Clamshell resistance furnace
- Hydrogen or argon gas ambient and gas supply system
- Turbomolecular pumping system
- Sapphire or graphite crucible

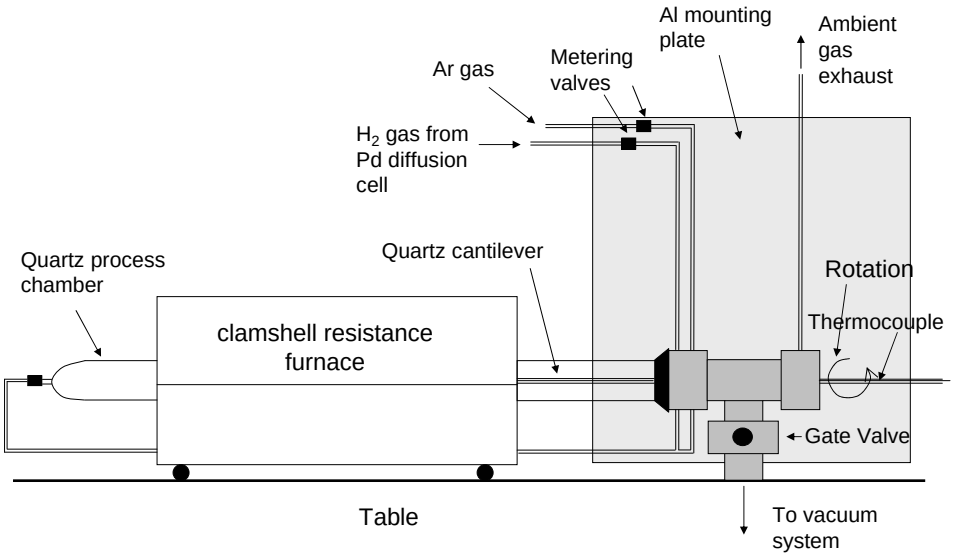

Figure 3.1: Schematic diagram of the tipping-boat LPE system used for GaAs film growth.

Initial attempts at the growth of high purity GaAs films used a graphite crucible that had been baked out at approximately 1500°C in vacuum using radio frequency induction heating. It was observed that the free electron concentration of the films, as determined by Hall effect measurements, decreased after baking of the crucible, suggesting that sulfur was the largest n-type contaminant since it is of high vapor pressure and most readily removed from the graphite by baking. This was later verified by magneto-photoluminescence spectroscopy, as discussed in Section 3.3.3. While extremely high purity GaAs films ($<1\times10^{13}$ cm^{-3}) were grown using graphite, the crucible was found to have a "memory effect" in which impurities introduced into the crucible could only be removed by a combination of baking and growth. The presence of impurities in the graphite, which could originate in the source materials used for growth or from the air, acted as a continuous source that could be slowly reduced over time. Another disadvantage of graphite as crucible

material was that it introduced carbon, an electrically active acceptor impurity in GaAs.

To address these problems a sapphire crucible was fabricated. Unlike graphite, because sapphire is a non-porous material, impurities that reach the surface cannot penetrate into the bulk. After each growth, the crucible was etched to restore it to its initial condition. Because the sapphire crucible can be etched between growths, it does not suffer from the memory effect of the graphite crucible. Films grown in the sapphire crucible are comparable to the highest purity films attainable using graphite.

The 6.0 cm ID silica process chamber and 1.6 cm OD $\times$ 1.0 cm ID silica cantilever were cleaned by etching with HF, followed by high temperature (800°C) baking under vacuum followed by flowing argon ambient. Cleaning is performed after periods of inactivity of crystal growth longer than two weeks. The silica cantilever, a tube which is closed at the end which resides inside the furnace, serves two purposes. The first is to support the crucible inside the furnace. Graphite crucibles were specially designed and machined to fit onto the end of the silica cantilever. The sapphire crucible could not be machined into the same shape as the graphite crucible because of its hardness. A silica holder was fabricated to connect the sapphire crucible to the cantilever rod. The second purpose of the cantilever is to allow a thermocouple to access the center of the furnace. The temperature measured at the furnace center is approximately the temperature of the source material and substrate within the crucible.

The cantilever rod can be rotated axially (see Figure 3.1) for transport of the solution to the substrate to initiate growth. It is positioned on a rail which allows motion along the axis of the reactor, and the system is sealed by a metal fitting with two o-

rings: one that seals with the silica cantilever and a larger one that seals with the steel T-section support structure. Before and after growth the crucible is removed from the furnace by pulling back the cantilever and the process chamber. A turbomolecular pump with mechanical roughing pump is used for evacuating the system prior to growth and during baking. The pumping system is separated from the process chamber by a gate valve. Further details on the design and construction of the LPE system are provided in [69].

3.2 Description of the growth process

For high-purity growth, the As source required for epitaxy was supplied to the Ga melt by the addition of small pieces of GaAs which were cleaved from a commercial semi-insulating wafer. For the growth of doped films, both semi-insulating and Te-doped GaAs wafer pieces were cleaved and added to the Ga solution. The substrate was also cleaved from commercial GaAs wafer. Both semi-insulating and conducting substrates were utilized. A semi-insulating substrate is required for accurate characterization of the film by Hall effect while conducting substrates allow characterization by capacitance-voltage measurements. Conducting substrates were also used for producing the BIB device. Prior to introduction into the crucible, all GaAs pieces were immersed in HCl for 1 minute followed by rinsing in distilled methanol to reduce Ga oxide that had formed at the surface.

During each growth run, 10 g of high-purity (8N) MBE grade Ga was placed inside the crucible as shown in Figure 2.9. The necessary amount of GaAs required to saturate the Ga at the initial growth temperature (approximately 0.55 g at 800°C) was weighed and added to the Ga, as described in Chapter 2. The system was closed by securing the seals

at the gas inlet, the outer growth chamber, and the cantilever assembly. The chamber was evacuated and the temperature increased to 300°C to remove water vapor from the system. Above 300°C the system is filled with 1 atmosphere of hydrogen gas which is purified by a Pd diffusion cell. Hydrogen gas flowed at the rate of approximately 1 L/min for the duration of the growth run. Once the system reached the initial growth temperature it was allowed to equilibrate for 8 hours, during which the GaAs dissolved into and saturated the Ga metal solvent. After the equilibration time, the temperature controller was set to ramp down at a rate of 30°C per hour. The crucible was tipped to allow the Ga+As solution to flow over the GaAs substrate once the temperature had dropped by 4°C. This initiated the growth process.

The sapphire crucible was etched between growth runs to remove residual Ga and GaAs that remained after removal of the growth materials. The crucible was first etched in concentrated HCl to remove Ga, followed by 4:1 HNO_3:HF to remove GaAs. Next it was immersed in hot concentrated H_3PO_4 kept at 250°C. Finally, the crucible was baked inside the growth system at 800°C in Ar ambient to remove residues from the etching process.

3.3 Characterization of high purity GaAs LPE films

The composition of high purity LPE GaAs films grown for this study were characterized by three measurement techniques: Hall effect and resistivity, capacitance-voltage, and magnetophotoluminescence spectroscopy.

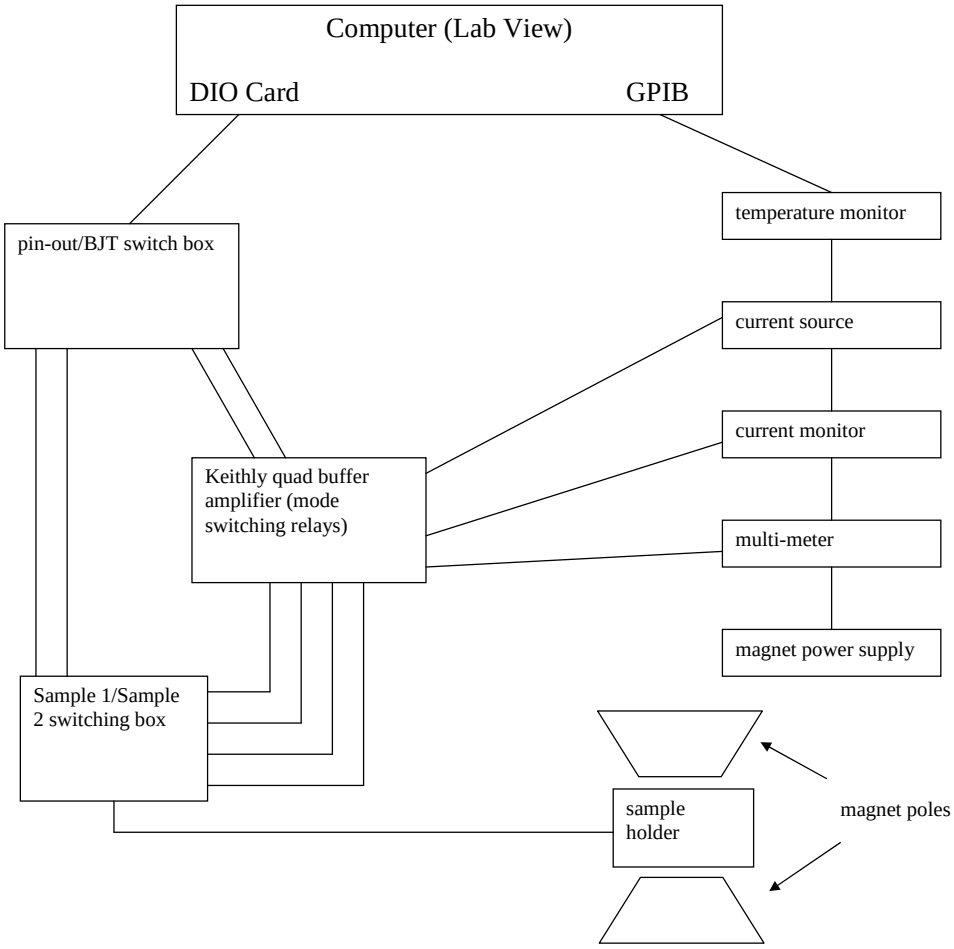

Figure 3.2: Block diagram of the Hall effect and resistivity measurement system.

3.3.1 Hall effect and resistivity characterization

Hall effect and resistivity measurements were performed to determine the carrier type, concentration, and mobility of the LPE films. The theory of these measurements is explained in Appendix D. A block diagram of the measurement system that was used for room temperature and variable temperature measurements is shown in Figure 3.2. The current is supplied by a Keithley model 220 programmable current source, which has an output range of 10^{-10} to 10^{-2} A. The current through the sample is measured by a Keithley

model 617 electrometer. The Hall voltage is measured by a Keithley model 196 digital multimeter. All three instruments are connected to a computer via GPIB interface and are connected to the sample holder through triaxial cables. The measurement mode is switched via a Keithley quad buffer amplifier that is controlled by the computer. An electromagnet combined with an HP 450 W power supply provides the magnetic field, which is set at a value of ± 3 kG.

Measurements taken at 77 K were performed in a separate Hall effect system in which the sample and sample holder are immersed in liquid nitrogen. The operation of this system is similar to that of the one described above however it does not utilize a computer for control. The magnetic field is only 100 G, and this system is suitable for the Hall measurement of high purity samples.

The results of Hall effect and resistivity measurements for many high purity, n-type films are presented in Tables 3.1 (77 K measurements) and 3.2 (300 K measurements). A complete list of all samples grown is given in Appendix E. Some films were characterized at 77 K in order to determine the Hall mobility more accurately, as the mobility is nearly a maximum at this temperature. Many films were measured at 300 K, however, since the free electron concentration, which is nearly constant between 300 K and 77 K, was used to gauge film purity in studying variations from run to run. Transport measurements of many of the highest purity samples ($\leq 5 \times 10^{12}$ cm^{-3}) yielded anonymously low mobility. This is believed to be due to inhomogeneous doping, and the presence of scattered p-type regions in the film. Most attempts at high purity growth resulted in n-type films. In rare occassions, high purity p-type films were obtained. This is most likely due to contamination

Sample	**Crucible**	**Thickness** $[\mu m]$	ρ_{77} [Ω cm]	n_{77} $[\mathrm{cm}^{-3}]$	μ_{77} $[\mathrm{cm}^2/\mathrm{V\ s}]$	Θ
196	graphite	70	5.68	8.79×10^{12}	125000	0.90
197	graphite	86	4.99	1.09×10^{13}	115000	0.90
198	graphite	110	2.02	3.01×10^{13}	103000	0.78
199	graphite	180	2.76	2.20×10^{13}	103000	0.76
200	graphite	86	1.15	5.72×10^{13}	95400	0.70
201	graphite	118	1.86	3.84×10^{13}	87700	0.83
214	graphite	75	1.16	4.31×10^{13}	125000	0.59
224	graphite	85	3.65	1.12×10^{13}	153000	0.77
330	sapphire	74	3.02	1.78×10^{13}	116000	0.83
337	sapphire	83	4.66	1.08×10^{13}	124000	0.85

Table 3.1: Results of Hall effect and resistivity measurements performed on high purity LPE GaAs films at 77 K. Θ is the compensation ratio calculated according to [66]. All samples were grown on semi-insulating GaAs substrates with a starting growth temperature of 800°C.

of the graphite crucible with an acceptor impurity species, or decomposition of the crucible, resulting in carbon contamination within the melt. At 77 K ionized impurity scattering is dominant in n-type GaAs. Walukiewicz et al. have calculated the effects of the donor and acceptor concentrations on the electron mobility at room temperature [67] and 77 K [66]. The compensation ratio in Tables 3.1 is based on these calculations.

3.3.2 Capacitance-voltage characterization

The concentration of space charges within the depletion region of a metal-semiconductor junction, which are due primarily to majority dopant atoms that have been stripped of their electrons (n-type) or holes (p-type), can be determined by measuring the junction capacitance as a function of bias. The depletion region of a junction acts as a capacitor which varies according to the bias. The depletion capacitance of a metal-semiconductor junction

Sample	**Crucible**	**Thickness** $[\mu m]$	ρ_{300} [Ω cm]	n_{300} $[\mathrm{cm}^{-3}]$	μ_{300} $[\mathrm{cm}^2/\mathrm{V\ s}]$
264	graphite	100	5.37	1.38×10^{14}	8440
291	sapphire	63	127	6.23×10^{12}	7900
300	graphite	41	1202	1.00×10^{12}	5200
301	graphite	31	61.8	1.86×10^{13}	5440
312	graphite	87	13537	1.90×10^{11}	2430
330	sapphire	70	104.2	1.67×10^{13}	7490
337	sapphire	83	54.1	1.43×10^{13}	8080
338	sapphire	90	53.42	1.50×10^{13}	7800
339	sapphire	103	214	4.5×10^{12}	6500
340	sapphire	85	367	3.34×10^{12}	5100

Table 3.2: Results of Hall effect and resistivity measurements performed on high purity LPE GaAs films at 300 K. All samples were grown on semi-insulating GaAs substrates with a starting growth temperature of 800°C.

is given by

$$C = \left|\frac{dQ}{dV}\right| = A\frac{\epsilon_\mathrm{s}}{x_\mathrm{d}} \tag{3.1}$$

where A is the device area, ϵ_s is the dielectric constant of the semiconductor, and x_d is the depletion region thickness. Electrostatic analysis within the n region of a junction via Maxwell's equations yields:

$$x_\mathrm{d} = \sqrt{\frac{2\epsilon_\mathrm{s}\left(V_\mathrm{bi} - V\right)}{qN_\mathrm{d}}} \tag{3.2}$$

where V_bi is the built-in potential, V is the applied bias, and N_d is the donor concentration. Using Equations 3.1 and 3.2, the donor concentration is related to the capacitance via Equation 3.3

$$\frac{d\left(1/C^2\right)}{dV} = \frac{2}{A^2\epsilon_\mathrm{s}qN_\mathrm{d}}\ . \tag{3.3}$$

C-V analysis was performed on LPE GaAs films that were grown on conducting substrates. Ohmic Ni/Ge/Au contacts were formed to the back side of the substrate by electron beam evaporation followed by annealing at 450°C for 30 seconds. A Pt Schottky

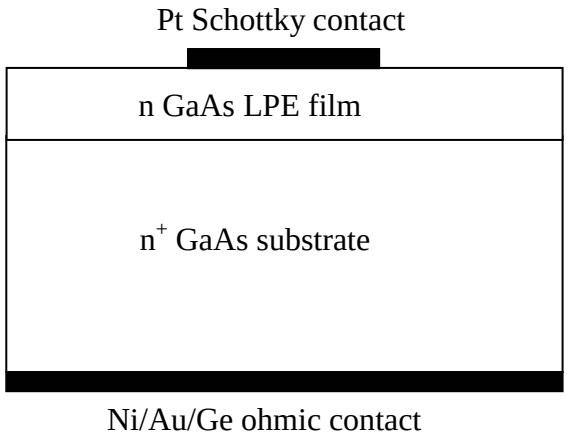

Figure 3.3: Schematic cross-section of a metal-semiconductor junction used for C-V analysis of LPE GaAs films.

contact was deposited via electron beam evaporation onto the film. Prior to evaporation, the film was treated with 20:20:1 H_2O:HNO_3:HF to achieve a clean surface, which reduces the concentration of interfacial defects between the Pt and GaAs. The schematic cross-section of a GaAs metal-semiconductor junction used for C-V analysis is shown in Figure 3.3. All C-V measurements were recorded using an HP model 4280A C-V plotter, with the bias applied to the Schottky contact.

The capacitance-voltage characteristic for a high purity sample is shown in Figure 3.4. The slope of the curve is related to the donor concentration by Equation 3.3. The sample of Figure 3.4 was measured under forward bias since the film was found to be fully depleted even at zero applied bias. The measured slope of $2.8\times10^{22}\mathrm{F}^{-2}\mathrm{V}^{-1}$ corresponds to N_d=5×10^{11} cm^{-3}, in close agreement with the smallest free electron concentrations of films grown on semi-insulating substrates as determined by Hall effect.

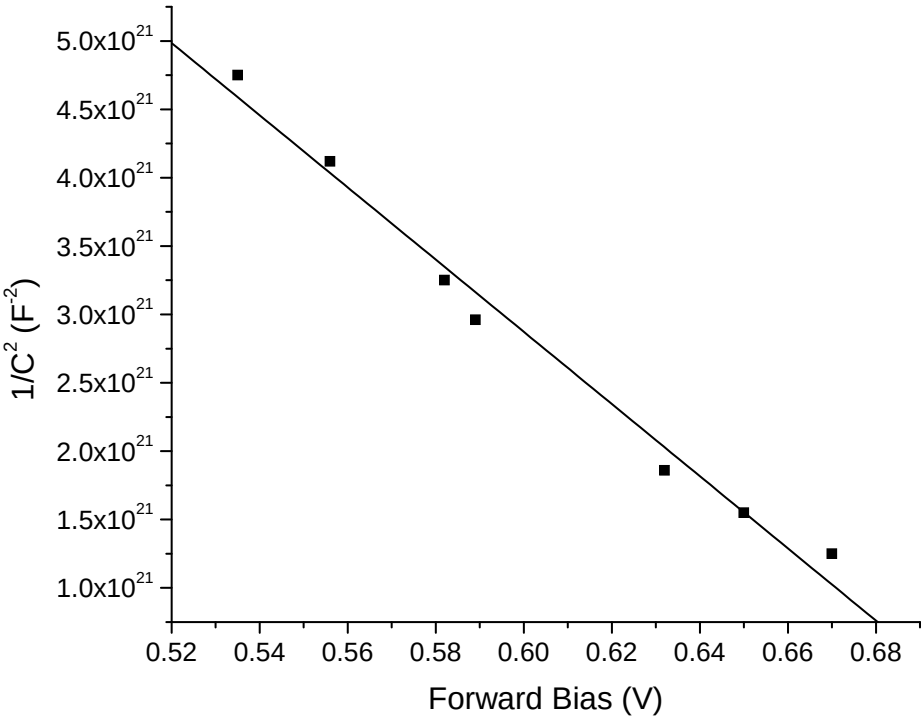

Figure 3.4: C-V characteristic for a Pt metal-semiconductor junction deposited on a high purity GaAs sample. The slope corresponds to a space charge concentration of 5×10^{11} cm^{-3}.

3.3.3 Magnetophotoluminescence characterization of residual impurities

Magnetophotoluminescence (MPL) characterization of several high purity films to identify the primary impurity species was performed by the group of M. Thewalt at Simon Fraser University, Burnaby, Canada . Standard photoluminescence spectroscopy of donors relies on the difference in the binding energy of excitons which are bound to specific donor species. Shallow donor species in GaAs, however, have very similar exciton binding energies due to the small electron effective mass and correspondingly large Bohr radii, as discussed in Appendix A. This makes the identification of specific donor species difficult due to the overlap of their photoluminescence peaks. The application of a magnetic field causes additional separation of the binding energy of excitons bound to various donor species by distorting the exciton wavefunction such that the electron becomes localized closer to the impurity center [68, 5]. The effect of the central cell on the exciton binding energy is enhanced, and the chemical shift of individual donor species can be more easily identified.

The main residual donor impurity species in several otherwise undoped high purity films was found to be S. A smaller MPL peak was also identified for Si donors. This finding is consistent with the experimental observation that the free electron concentration of the high purity films was found to be lower after the baking of the graphite crucible since baking is believed to most efficiently remove sulfur due to its high vapor pressure. Carbon was identified as the main acceptor peak in all high purity films.

3.4 Growth and characterization of doped GaAs LPE films

For proper operation, the absorbing region of a BIB detector must be doped at a concentration which is below the metal-insulator transition (MIT). For Te in GaAs, as discussed in Chapter 1, the MIT occurs at approximately 2×10^{16} cm^{-3}. The doping of LPE GaAs films with Te for this purpose was studied by the addition of two types of Te sources to the Ga melt: high purity (7N) Te metal and pieces of commercial Te doped substrates. The addition of 8 mg of high purity Te metal to the melt combined with GaAs source material resulted in a film with a free carrier concentration of 7×10^{18} cm^{-3} and an electron mobility of 943 cm$^2/Vs$. Analysis of the film by Rutherford backscattering spectrometry (RBS) was performed, and revealed a Te concentration of approximately 1×10^{21} cm^{-3}. This value corresponds to the solubility limit of Te in GaAs of 2%. The addition of Te directly to the Ga melt was found to be unsuitable for growth of the BIB absorbing region because extremely small amounts of the metal are required to limit the Te concentration in the film to acceptable levels. Doping at the moderate levels required for the BIB absorbing region using this technique is made difficult since it requires the preparation and weighing of very small pieces of Te metal.

The addition of commercial, 3×10^{18} cm^{-3} Te-doped GaAs to the Ga melt was found to offer the best control over the resulting concentration in the film. This technique allows for the introduction of a sufficiently small amount of Te into the melt without the difficulty of isolating and weighing extremely small amounts of material. The resulting free electron concentrations of films doped in this manner are shown as a function of the Te concentration in the Ga solution in Figure 3.5. A linear relationship is achieved over

Sample	**Te source**	**Te source mass** $[mg]$	n_{300} $[\mathrm{cm}^{-3}]$	μ_{300} $[\mathrm{cm}^2/\mathrm{V\ s}]$	Θ
248	Te metal	4.0	1.0×10^{18}	1530	0.6
251	Te metal	9.0	5.9×10^{18}	1510	0.55
288	GaAs:Te wafer	20	1.1×10^{16}	5450	0.55
292	GaAs:Te wafer	1.7	1.0×10^{15}	6550	0.77
293	GaAs:Te wafer	71	6.5×10^{16}	4380	0.35
273	GaAs:Te wafer	480	3.7×10^{17}	3390	0.3
274	GaAs:Te wafer	364	3.9×10^{17}	3240	0.35
275	GaAs:Te wafer	254	1.8×10^{17}	3750	0.31
276	GaAs:Te wafer	164	1.98×10^{17}	2630	0.58
277	GaAs:Te wafer	92	6.7×10^{16}	4330	0.34
278	GaAs:Te wafer	20	1.4×10^{16}	5080	0.55
279	GaAs:Te wafer	10	5.3×10^{15}	5480	0.73
281	GaAs:Te wafer	12	5.9×10^{15}	5570	0.65
284	GaAs:Te wafer	10	5.1×10^{15}	5140	0.75
285	GaAs:Te wafer	16	7.9×10^{15}	5150	0.67
292	GaAs:Te wafer	1.7	1.0×10^{15}	6550	0.78

Table 3.3: Free carrier concentration, Hall mobility, and calculated compensation ratio for Te doped LPE GaAs samples grown in a sapphire crucible. Samples were doped by adding either Te metal or pieces of commercial [Te]=3×10^{18} cm^{-3} GaAs:Te.

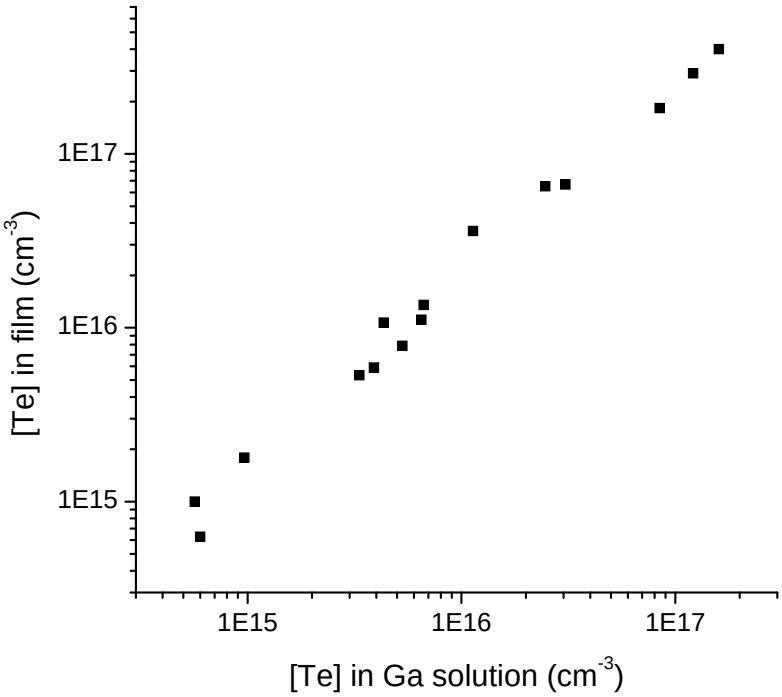

Figure 3.5: Free electron concentration measured by Hall effect in LPE GaAs films as a function of the Te concentration in the growth solution.

all film concentrations grown in the study. The scatter of the data is due the variation in the compensation level, which causes the free electron concentration to deviate from the Te concentration in the film. Table 3.3 shows the results of Hall effect and resistivity characterization of several films doped by the two techniques discussed.

3.4.1 Optical characterization of Te doped LPE GaAs films

Since the GaAs films grown for this study are intended for use as the absorbing layer of a far-infrared BIB device, it is important to characterize their far-infrared optical absorption properties. The determination of the far-infrared absorption spectrum as a function of donor concentration was found to be a necessary step toward determining the optimal doping level for proper GaAs BIB device operation, as will be shown in the following

Sample	**Thickness** [μm]	n_{300} [cm^{-3}]	μ_{300} [cm^2/V s]	**FWHM** [cm^{-1}]	**Theory FWHM** [cm^{-1}]
286	40	1.0×10^{15}	5680	13	0.15
294	66	2.1×10^{16}	4490	55	68
295	62	6.7×10^{15}	5280	28	13
191	62	1.0×10^{14}	7440	N/A	N/A
Ref.	N/A	SI	N/A	N/A	N/A

Table 3.4: Free carrier concentration, Hall mobility, and calculated compensation ratio for the Te doped GaAs LPE films used for absorption studies. Also shown are the values for a high-purity, unintentionally doped film used for photoconductivity measurements. All films are grown on semi-insulating GaAs substrates.

paragraphs. The absorption coefficients α of three LPE GaAs:Te films containing different concentrations of Te were determined using Fourier transform infrared spectrometry. Details about the spectrometer that was used for these measurements are given in Appendix C.5. All films were grown on semi-insulating GaAs wafers and their Te content estimated by Hall effect. Relevant information about each sample is given in Table 3.4. Prior to analysis, all films were lapped and polished to reduce their thickness and generate a flat surface. Lapping using 0.3μm alumina grit slurry was followed by colloidal silica chemo-mechanical polishing on a rotary polishing machine. Lapping was performed to adjust the total absorbance (αx) of each sample in order to optimize the sensitivity of absorption measurements and to achieve as flat a film surface as possible. The substrate face of each sample was lapped at a 1° angle towards the epilayer to avoid Fabry-Perot oscillations within the sample. Absorption measurements were taken at 1.35 K in a pumped liquid He test dewar, using the stepping mirror Fourier transform infrared spectrometer described in Appendix C.5, with a 50 μm thick Mylar beamsplitter. Cold black polyethylene and a cold 100 cm^{-1} low pass filter [1] were inserted into the beam path to reject band-edge light and to increase the

signal to noise ratio in the spectral band of interest. Transmission was measured using a neutron transmutation doped (NTD) Ge bolometer detector. The light source, a mercury arc lamp, was chopped at 13 Hz.

The substrate absorption was cancelled by taking a ratio of the total transmitted intensities of the film+substrate to that of a semi-insulating GaAs reference substrate of the same wedged configuration, $I_{\text{film+sub}}/I_{sub}$. The relation of the absorption coefficient to the transmission signal and sample thickness is given by Equation 1.7, repeated here for a film of thickness t_{film}, absorption coefficient α_{film}, and reflectivity R.

$$\frac{I_{\text{film+sub}}}{I_{\text{sub}}} = \frac{(1-R)^2 e^{-\alpha_{\text{film}} t_{\text{film}}}}{1 - R^2 e^{-2\alpha_{\text{film}} t_{\text{film}}}} \quad , \tag{3.4}$$

The absorption coefficient of the semi-insulating substrate is assumed to be negligibly small. This assumption is justified by the low extinction coefficient of the material in the range of 10 to 100 cm^{-1} (1.2 to 3.6$\times 10^{-3}$) giving rise to an absorption coefficient of α=.34 cm^{-1}. Such a small value can be neglected compared to the absorption of the doped films. The reflectivity is estimated to be R=0.317 based on measurements of the index of refraction for semi-insulating GaAs in the frequency range of interest [51].

The absorption spectra obtained from the three films after performing a ratio with the reference sample are shown in Figure 3.6 at a resolution of 2 cm^{-1}. For comparison the photoconductivity spectrum of a 1$\times 10^{14}$ cm^{-3} unintentionally doped n-type film (sample 191) is also shown in Figure 3.6. The sharp photoconductivity peak at 35.5 cm^{-1} is due to the 1s-2p bound excited state transition followed by thermal ionization or tunneling into the conduction band. A second, broader peak at 49 cm^{-1} represents 1s-continuum transitions. The deliberately Te doped samples 286, 294 and 295 show absorption maxima near

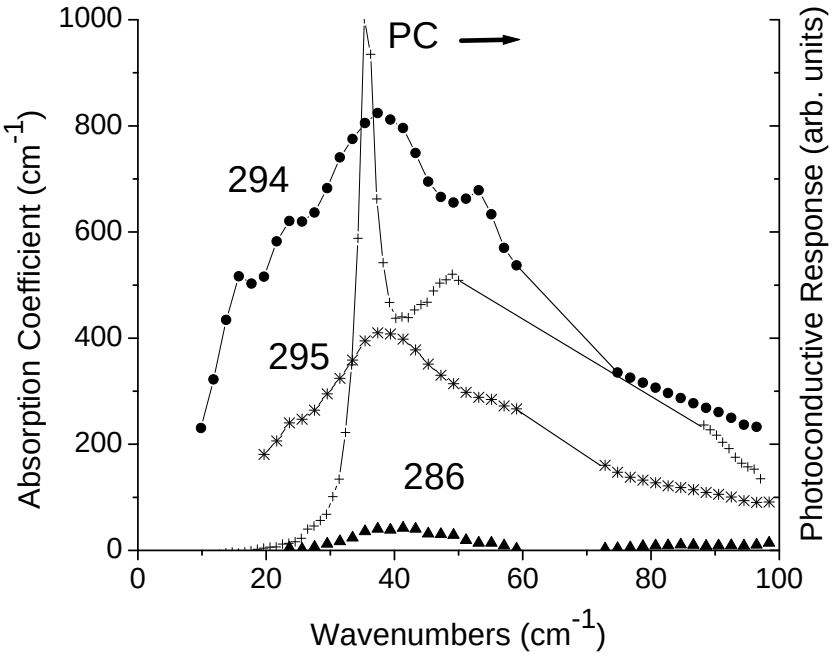

Figure 3.6: The spectral depencence of the absorption coefficient for samples 286 (1×10^{15} cm^{-3}), 295 (6.7×10^{15} cm^{-3}), and 294 (2.1×10^{16} cm^{-3}), and the photoconductivity of sample 191 (1×10^{14} cm^{-3}). The dashed lines indicate loss of data due to a beamsplitter minimum.

37 cm^{-1}, between the 1s-2p and 1s-continuum transition energies, and represent a combination of both types of excitation. The broadening of the absorption spectra with increasing doping concentration shown in Figure 3.6 is a result of impurity band formation. Two mechanisms form and broaden impurity bands in this material. The first is due to the exchange interaction between neighboring electronic states associated with individual Te impurities. This mechanism is discussed in detail in Appendix B. The second mechanism is due to the Coulomb interaction between neutral and ionized impurities. The relative importance of this effect, known as Stark broadening, depends on the compensation level of the material [43]. At low temperatures, the concentration of ionized impurities is approximately equal to the concentration of compensating acceptors. The electric field associated with each ionized impurity causes a Stark shift of the electronic energy levels of its neighbors. Since ionized

impurities are randomly distributed, electrons bound to donor atoms will occupy a range of energies which depend upon the proximity to localized electric fields. This causes line broadening in optical absorption and emission experiments, which measure the combined optical interaction of many donor electrons.

Broadening due to exchange interaction for a donor electron is related to the overlap integral with its nearest neighbors (coordination number z=6 for simple cubic) B=2zI, as discussed in Appendix B. The overlap integral of Equation B.6 can be approximated by

$$I = 5E_{\mathrm{ry}}e^{\frac{b}{a}} \tag{3.5}$$

where E_{ry} is the Rydberg energy (≈4.6 meV for donors in GaAs), b is the average impurity spacing, and a is the donor electron Bohr radius. Upon applying this theory (Table 3.4) to the three absorption samples, relatively good agreement is found only at the higher concentrations. The reason for the large underestimation of the broadening at 1×10^{15} cm^{-3} is most likely due to Stark broadening as discussed above. At the higher concentrations, impurity band broadening has occurred to a much more significant extent, and begins to outweigh the effect of the random electric field dispersion.

The broadening of the impurity band at higher doping concentrations leads to a significant extension of the far-infrared response of a detector that is fabricated from such material. The maximum absorption at 37 cm^{-1} corresponds to a wavelength of approximately 270 μm. This shows that a GaAs BIB detector will have a response at wavelengths significantly greater than the 220 μm limit characteristic of uniaxially stressed Ge:Ga photoconductors. The absorption coefficient falls to half of its peak value at 30 cm^{-1} (333 μm) for sample 286, and at 20 cm^{-1} (500 μm) for sample 295. This means that a GaAs BIB

with an absorbing layer concentration of 6.7×10^{15} cm^{-3} should be sensitive to photons of wavelength as large as 500 μm.

3.4.2 Variable temperature Hall effect and resistivity of GaAs:Te

Variable temperature Hall effect and resistivity measurements were performed using the Hall effect system described in Section 3.3.1. For low temperature measurements, the sample was secured to a copper cold finger in contact with a liquid helium flow cooling system. The temperature was monitored by two Lakeshore [42] DT-470 Si diodes that have been calibrated for use between 350 K and 1.3 K. One diode was positioned outside of the magnetic field to allow proper temperature monitoring during Hall effect measurements. Temperature control is attained by flowing current through a Ni-Cr heating wire wrapped around the cold finger. A Lakeshore model 331 temperature controller, interfaced with the computer via GPIB, was used to maintain the temperature at a desired value below 100 K. Above 100 K, the temperature is controlled by the regulation of He flow through the system by the operator. The sample space is surrounded by two radiation shields which are maintained at the cryostat temperature. The outside of the cryostat is an aluminum vacuum enclosure. Sample, heater, and temperature sensor contacts are brought through a vacuum feedthrough. The system was evacuated by a turbomolecular pump, backed by a mechanical pump.

Impurity band formation in GaAs:Te is evident from electronic transport measurements. Figure 3.7 displays the free electron concentration of the three samples as a function of inverse temperature. As the temperature is lowered the concentration of electrons in the conduction band decreases as electrons freeze-out onto donor states, as discussed in

Appendix D. This is seen clearly in the free electron concentration of sample 286 in Figure 3.7. Since the samples are highly compensated, the slope of the freeze-out curves of Figure 3.7 are proportional to the thermal binding energy of electrons within the impurity band. Using the relations of Appendix D.3.2, the thermal binding energies for samples 286 and 295 are determined to be 3 meV and 2.3 meV, respectively. The decrease in binding energy with increasing donor concentration reflects the broadening of isolated energy levels into a band with the upper most states closer to the conduction band edge. In the most lightly doped sample, 286 (1×10^{15} cm^{-3}), freeze-out of shallow donors continues down to a temperature of approximately 67 K. Below this point the impurity band is sufficiently populated with carriers such that electron hopping within the impurity band becomes the dominant conduction mechanism (instead of electron motion within the conduction band).

The formation of impurity bands is further demonstrated by temperature dependent resistivity measurements. It is discussed in Appendix B that the total resistivity of an n-type semiconductor is the sum of three major components: electron travel within the conduction band (ρ_1), the upper Hubbard band (ρ_2), and hopping between ionized donor atoms (ρ_3). Each conduction mechanism has an activation energy associated with it equal to the energy required to excite an electron from a bound state to a conducting state. The transition from electron travel within the conduction band to hopping between impurity centers is clearly seen by examining the temperature dependence of the resistivity as shown in Figure 3.8. A change in slope of the Arrhenius plot indicates a shift in the conduction mechanism to nearest neighbor hopping as the conduction band is depopulated of electrons.

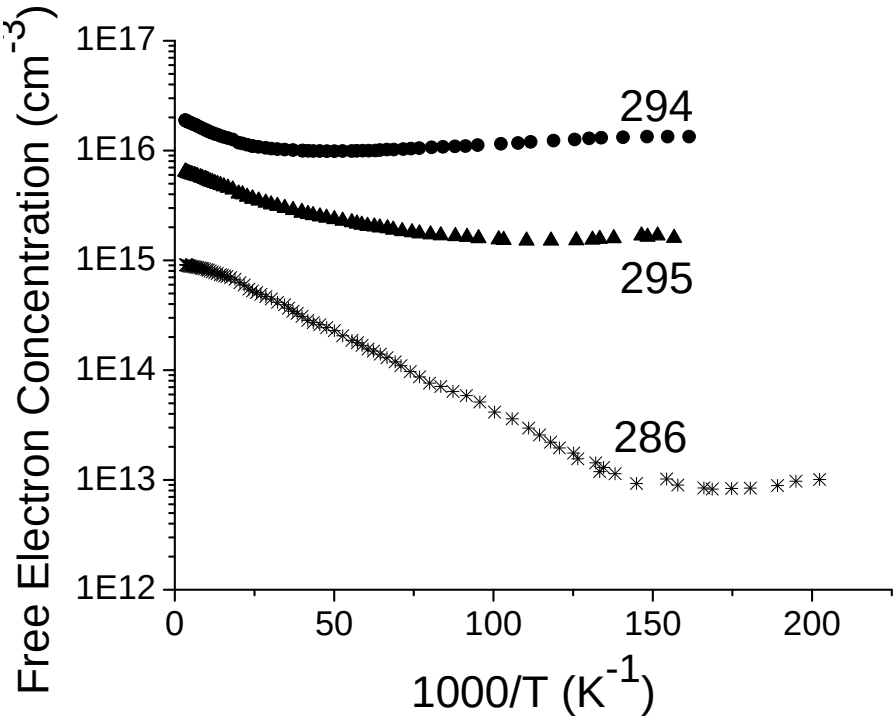

Figure 3.7: Variable temperature Hall effect results.

The dominance of hopping conductivity at very low temperatures indicates that there are not a large number of empty, conduction-band-like states mixed with the impurity band. The two bands are quite distinct. The activation energy for hopping conduction, ϵ_3, can be estimated from the slope of this curve at low temperatures. The activation energies, estimated from the data of Figure 3.8 are 0.27 meV for 1×10^{15} cm^{-3}, 0.018 meV for 6.7×10^{15} cm^{-3}, and 0.005 meV for 2×10^{16} cm^{-3}. The activation energies are strong functions of the impurity concentration as well as the compensation. This is because the nearest neighbor hopping process, which involves the absorption and re-emission of a phonon, requires an empty donor site to jump into. At low temperatures, the ionized donor concentration is very nearly equal to the concentration of compensating acceptors.

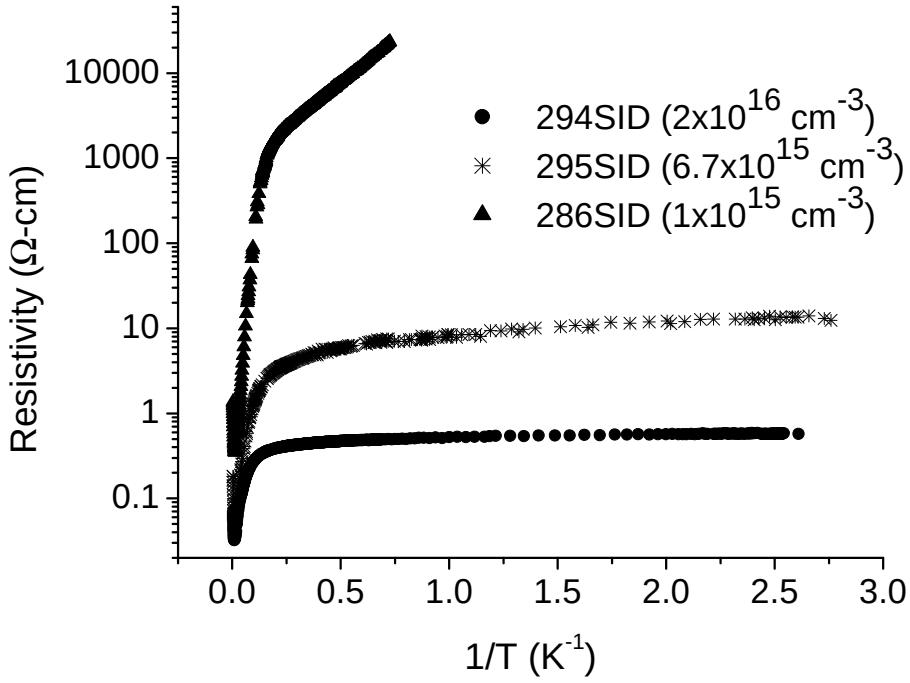

Figure 3.8: The temperature dependence of the resistivity of doped GaAs samples.

Chapter 4

BIB device fabrication and testing

4.1 Introduction

The optimized dopant concentration for a BIB absorbing layer can be estimated based on the absorption spectra of Figure 3.6 and the electrical transport data of Figure 3.7 and Figure 3.8. The most lightly doped sample, 286 (1×10^{15} cm^{-3}), shows a sharp absorption cutoff near 26 cm^{-1}, a clear freeze-out region in the variable temperature Hall effect results, and a characteristic hopping dependence of the resistivity. For sample 295 (6.7×10^{15} cm^{-3}), the separation of the conduction and impurity bands, although smaller than for sample 286, is still evident. The well defined thermal activation energy for hopping and band conduction present in these samples, combined with well defined absorption maxima, suggests a clean separation of the impurity band states from the conduction band, as required for BIB operation.

The absorption spectrum of the most heavily doped sample (294) extends to very low energy while its free electron concentration shows only very slight freeze-out behavior.

Furthermore the resistivity of this sample is nearly constant with decreasing temperature, and the hopping activation energy is practically zero, indicating the dominance of conduction band conductivity over hopping in the impurity band. This suggests that sample 294 is approaching the metallic conduction regime. Since the freeze-out region of sample 294 is not well defined, a meaningful value of the activation energy cannot be extracted from the Hall effect data. It can therefore be inferred that the impurity band extends very close to the conduction band at the concentration of 2×10^{16} cm^{-3}, as predicted by the theory of Mott (Appendix B).

An active layer doped between the concentrations of 1×10^{15} cm^{-3} (sample 286) and 6.7×10^{15} cm^{-3} (sample 295), appears to be a good candidate for a GaAs BIB detector. In this range, a clear absorption maximum and shallow donor thermal activation energy exists. The linear absorption coefficients for this range vary between approximately 100 and 800 cm^{-1} for photons of 37 cm^{-1}, far greater than the values that could be achieved by a standard GaAs photoconductor. Below a doping concentration of 1×10^{15} cm^{-3}, the width of the impurity to conduction band absorption peak narrows, limiting the optical bandwidth of the detector. Furthermore, the absorption coefficient near 40 cm^{-1} of GaAs with doping less than 1×10^{15} cm^{-3} is relatively low, meaning that a BIB detector fabricated from such material would need a very thick depletion layer to have acceptable quantum efficiency. Above 6.7×10^{15} cm^{-3}, the impurity band to conduction band energy gap approaches zero.

4.2 BIB device fabrication

Based on the optical absorption and variable temperature transport results of Chapter 3, a Te donor doping value of 5×10^{15} cm^{-3} was targeted as the absorbing layer concentration. The proper amount of GaAs:Te wafer was added to the Ga melt in order to achieve this doping concentration, based on the results of Figure 3.5. It was found, however, that the resulting Te concentration in the film varied by up to a factor of 3 about the targeted value. This variation is believed to be due to the variation of the compensation ratio between growth runs.

This problem was circumvented by acquiring a commercially prepared, sulfur doped chloride vapor phase epitaxial (VPE) film grown on a 250 mm conducting GaAs substrate. The VPE technique, while not able to achieve as high purity GaAs films as tipping boat LPE, allows much greater control over impurity incorporation and film thickness (see Chapter 2). A 40 μm thick epitaxial GaAs film, grown onto a conducting n-type, 200 mm GaAs substrate, and containing 5×10^{15} cm^{-3} sulfur was acquired from the Sumitomo corporation [60]. The VPE film has a flatness of $\pm$ 2μm.

A BIB device was fabricated by growth of a high purity blocking layer onto the commercial VPE absorbing layer. Blocking layer growth was performed at a maximum temperature of 700°C with a temperature ramp of 30°C per hour under hydrogen ambient. Growth was begun at lower than the usual temperature of 800°C to reduce the film thickness. After growth, the LPE film, initially 45 μm thick, was lapped using 1 μm alumina grit on a glass plate to reduce it to 20 μm. Next, the film was polished on a rotary polishing machine using a slurry of water, Syton, and liquid bleach (sodium hypochlorite) (200:150:10) until the

thickness was 10 μm. This ratio of the Syton and bleach slurry was found to reproducibly yield a high quality surface. The bleach is a weak chemical etchant of GaAs. After polishing, the thickness of the blocking layer was measured by comparing the blocking layer+absorbing layer+substrate thickness to another piece of the absorbing layer+substrate taken from the same wafer. Thickness measurements were performed using a depth gauge with a resolution of approximately 1μm. The blocking layer was found to be sloped, its thickness ranging from 10 μm at the thickest to 0 μm at the thinnest. A 6 mm $\times$ 4 mm section of the sample which had a uniform blocking layer thickness of 10 $\pm$1 μm was cut out and used to fabricate the BIB device.

Once the high purity film was prepared and polished, the blocking layer top contact was formed by ion-implantation of sulfur. A total sulfur dose of 4×10^{12} cm^{-2} was implanted at an energy of 32 keV, at an angle of 7° to prevent ion channeling. The implanted contact over the entire top surface of the blocking layer is important for efficient charge collection. The sulfur concentration within the contact must be limited because of optical absorption since photons must traverse through the top contact and blocking layer before interacting with the absorbing layer of the device. Following ion-implantation, the device was annealed at 800°C for 10 s in an Ar ambient to activate the sulfur and repair crystalline damage. Finally, ohmic Ni/Ge/Au contacts were evaporated over the substrate back side and over a small section of the blocking layer. The contacts were annealed at 450°C in nitrogen ambient. A schematic of the BIB detector cross-section is displayed in Figure 4.1.

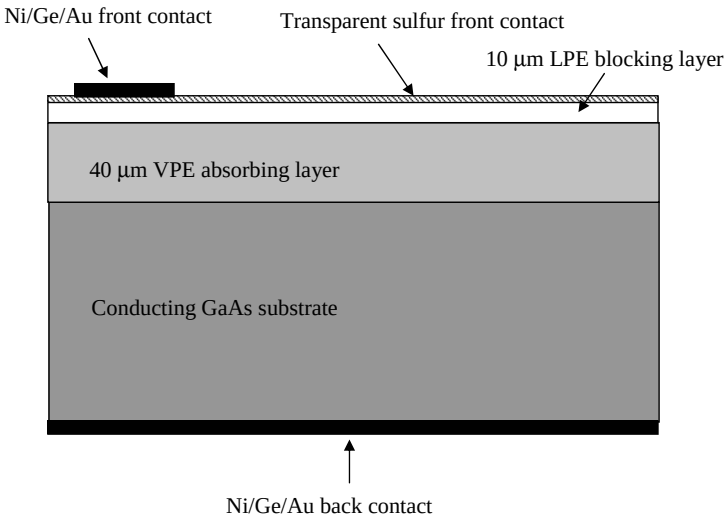

Figure 4.1: Schematic cross-section of the fabricated BIB detector.

4.3 BIB device testing

4.3.1 Cryogenic optical and electrical measurement apparatus

Both the electrical and optical characteristics of the GaAs BIB detector were studied at low temperature. Measurements were performed in two dewars acquired from Infrared Laboratories [35], one which is capable of reaching a minimum temperature of 1.2 K and one which can attain 0.3 K. Both dewars contain a liquid helium vessel that is in direct contact with a copper plate onto which the detector and optics are mounted. The plate is surrounded by an aluminum radiation shield that is at the same temperature. The dewars also contain a separate liquid nitrogen vessel which is attached to a radiation shield surrounding the liquid helium system. The liquid nitrogen shield serves as an intermediate shield between the 300 K outer vacuum chamber of the dewar, and the 4.2 K to 1.2 K liquid helium stage. The 1.2 K dewar contains a polyethylene optical window, allowing spectral

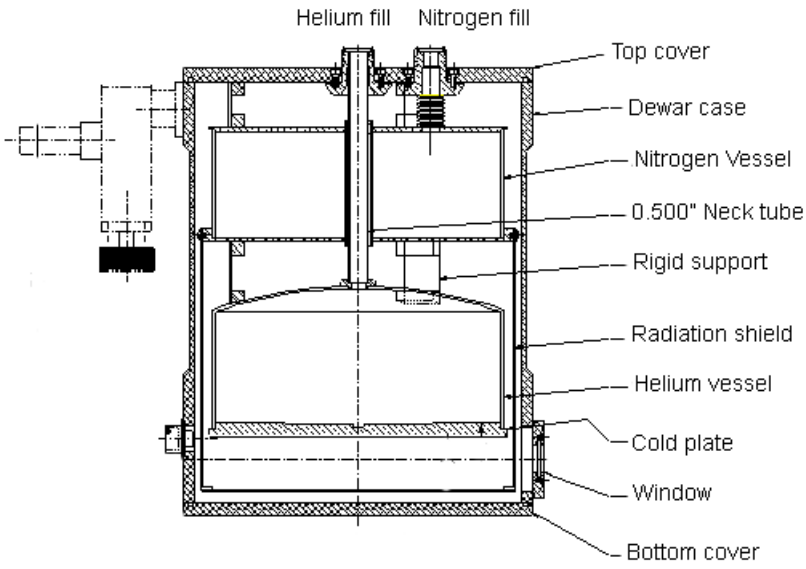

Figure 4.2: Cross-sectional drawing of an Infrared Laboratories dewar used for BIB detector characterization. Drawing by Infrared Laboratories, Inc. [35].

information to be determined. The polyethylene window is transparent for long wavelength photons in the infrared, and has been mechanically polished at a low angle to eliminate Fabry-Perot oscillations. A schematic drawing of this dewar is shown in Figure 4.2. The 0.3 K dewar has no optical window and is therefore useful for electrical measurements in the dark only. It incorporates a ^{3}He absorption refrigerator in which cooling is accomplished by the condensation of ^{3}He vapor onto a metal surface kept at 1.2 K. Both dewars must be evacuated prior to cooling to reduce conductive thermal coupling between the liquid helium, liquid nitrogen, and ambient containers.

Both dewars contain transimpedance amplifier (TIA) readout electronic circuits. The circuit diagram of a TIA is displayed in Figure 4.3. The most important components of the TIA circuit are an operational amplifier, a set of two depletion mode junction field effect transistors (JFETs) with common drains, and a feedback resistor R_F. The feedback

resistor and JFETs are mounted inside the dewar. The JFETs are are maintained at 70 K for proper operation by a heating resistor. The feedback resistor is kept at 4.2 K or colder to reduce Johnson noise. The BIB device backside contact is connected to the gate of one of the JFETs and the feedback resistor. Bias is applied to the blocking layer contact of the device. A modulation of the current through the detector causes a change in potential at the gate of the JFET, resulting in a change in the source to drain voltage (V_{sd}). The two JFETs are specially chosen such that their electrical characteristics are similar, so that their channel resistances will be similar. The voltage change at the source of the JFET due to the change of gate voltage is sensed at the inverting input of the op-amp. The output of the op-amp is proportional to the difference in bias between the inverting and non-inverting inputs. Feedback from the op-amp output acts to eliminate this difference in bias. Therefore the shift in V_{sd} causes the op-amp to output current to flow through $\mathrm{R_F}$ which is exactly equal to the photocurrent through the BIB device. The detector output signal corresponds to the bias across $\mathrm{R_F}$. This circuit allows for the observation of very small photocurrents if a large value of $\mathrm{R_F}$ is used. The feedback of the op-amp output to the JFET gate maintains a constant bias on the detector. In all experiments to be discussed, a feedback resistor with a value of $\mathrm{R_F}$=10^9 Ω was used.

4.3.2 Electrical testing

The dark current-voltage characteristics of the GaAs BIB device for several temperatures are shown in figure 4.4. To judge the effectiveness of the blocking layer, a device consisting of two ohmic contacts (Ni/Ge/Au) deposited on opposite sides of a piece of the absorbing epitaxial layer and conducting substrate was fabricated and its electrical prop-

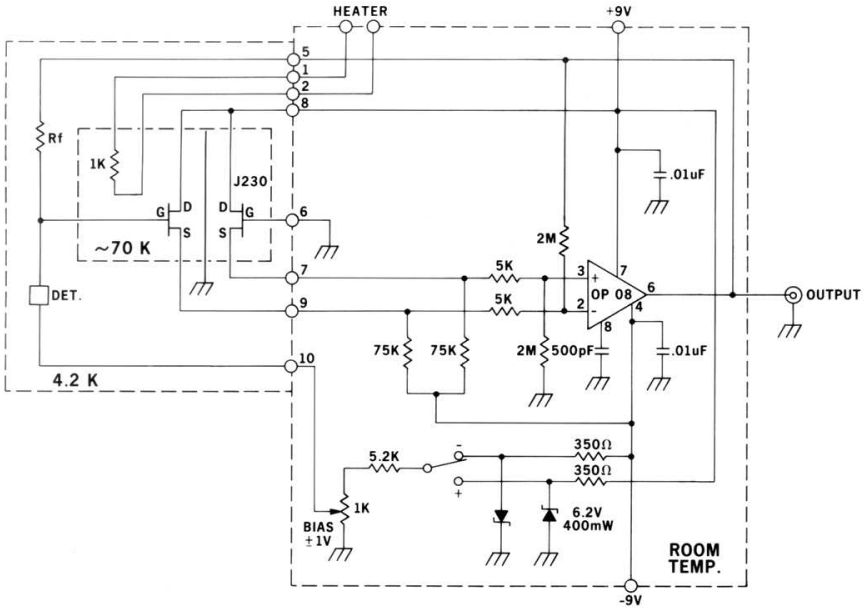

Figure 4.3: Circuit diagram of the transimpedance amplifier readout used for BIB device characterization.

erties measured at 1.3 K. The I-V curve for this structure is highly linear. The I-V curves for the BIB device are shown with the bias applied to the blocking region, and appear significantly different due to the presence of the blocking layer. At 4.2 K, many electrons within the absorbing layer are not yet bound to donor impurities. These electrons, which occupy the conduction band, are free to travel through the blocking layer and constitute a dark current. The dark current is only slightly reduced by the blocking layer. As the temperature is reduced, however, more electrons become bound within the impurity band of the absorbing layer, and are therefore blocked from traveling to through the blocking layer where no impurity band exists. At 1.3 K, the dark current through the BIB device is greatly reduced compared to the bare absorbing layer structure, demonstrating the significant effect of the blocking layer. The BIB device current at 1.3 K is also much smaller than it is at 4.2 K, demonstrating the effect of electron freeze-out within the absorbing layer. At 420 mK,

the I-V curve is nearly constant over an even wider bias range than at 1.3 K, indicating efficient blocking of electrons from the absorbing layer. At such low temperatures, the dark I-V curve for the BIB device is representative of hopping current through the blocking layer.

At sufficiently high positive bias a sharp increase in the current is observed for the lowest temperature BIB device I-V curves. This increase is most likely due to the breakdown of the blocking layer as the electric field becomes higher. The electric field within the blocking layer may be increased by the diffusion of sulfur impurities from the absorbing layer. A gradual decrease in the donor concentration from the absorbing layer to the blocking layer is believed to cause a sharp increase in the electric field at the interface. Bandaru et al. have shown that this effect is important in Ge:Sb BIB detector development [7]. The I-V curve for the BIB device is highly asymmetric about zero bias at the lowest temperatures of 1.3 K and 420 mK. The origin of the asymmetry of the device is not well understood. One possible cause is inhomogeneous doping within the blocking layer. Regions of p-type GaAs within the blocking layer could result in an asymmetric I-V curve, similar to a diode.

4.3.3 Optical testing

Optical testing was only possible at a minimum temperature of 1.3 K because of the lack of a window in the dewar containing the ^{3}He refrigerator. Far infrared spectra were recorded using the spectrometer described in Appendix C.5. The photoconductivity spectrum of the GaAs BIB device is shown in Figure 4.5. The spectrum was recorded using a 50 μm Mylar beamsplitter, a 200 μm black polyethylene filter to eliminate band gap light, and with 30 mV positive bias applied to the blocking layer. The sharp peak at 35.5 cm^{-1}

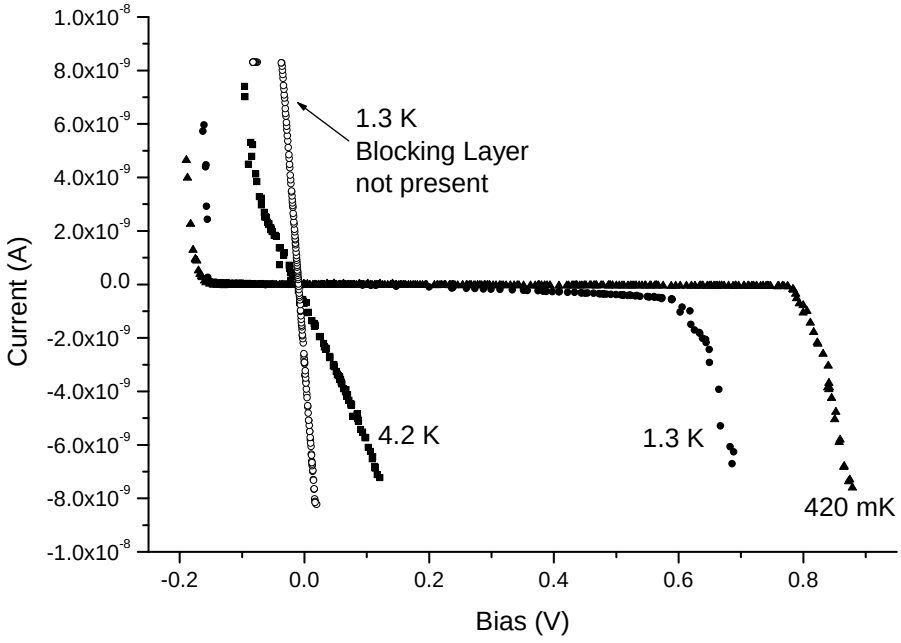

Figure 4.4: Dark current versus voltage characteristics for the GaAs BIB as a function of temperature.

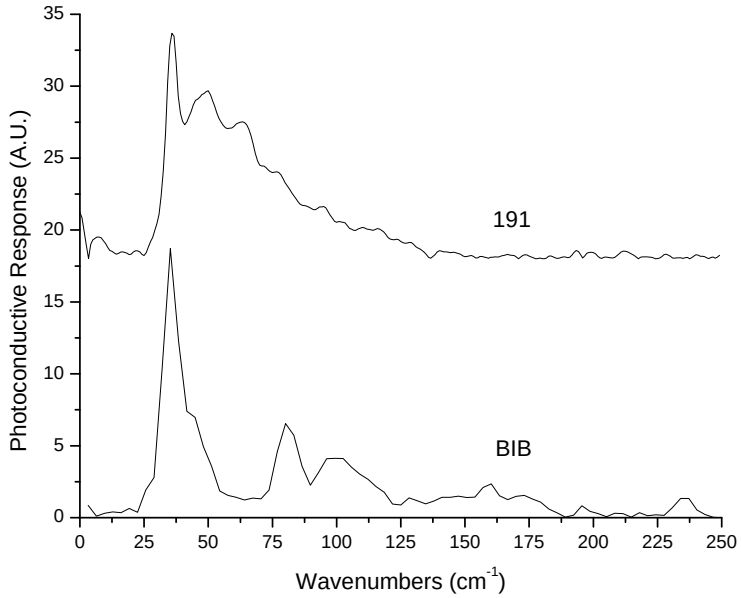

Figure 4.5: Comparison of the photoconductivity spectra for the high purity sample 191 and a GaAs BIB device. The sharp peak at 35.5 cm^{-1} is due to the 1s-2p excited state transition. A 25 μm thick beamsplitter was used for sample 191 and a 50 μm beamsplitter was used to characterize the BIB device.

represents the 1s-2p transition of Te donors in GaAs. Its presence indicates that most of the optical response is due to absorption within the high purity blocking layer, and not within the absorbing layer. The sharp 1s-2p photoconductivity peak is not expected to be present in GaAs doped at 5×10^{15} cm^{-3} due to impurity band formation and broadening. Extended optical response at lower energy than the 1s-2p transition would be expected from such a film based on the absorption experiments of Figure 3.6. The lack of extended absorption indicates that the depletion region within the absorbing layer is extremely thin due, most likely, to high compensation of the material. The photoconductive response of sample 191, a high purity (1×10^{14} cm^{-3}) n-type LPE film is shown for comparison.

4.3.4 Compensation in doped LPE GaAs films

All LPE GaAs films grown in this study are believed to have compensation ratios between 0.1 and 0.9. This has important consequences for a BIB detector. As discussed in Chapter 1, the depletion region thickness of a BIB detector is inversely proportional to the square root of the minority doping concentration. An absorbing layer film of 50% compensation, doped with a donor concentration near 5×10^{15} cm^{-3} has an acceptor concentration of 2.5×10^{15} cm^{-3}. Using Equation 1.19, the corresponding depletion region width w for a GaAs BIB detector with 400 mV of applied bias, the limit of breakdown at 1.3 K according to Figure 4.4, and a 10 μm thick blocking layer is 14 nm. Taking the maximum value of the absorption coefficient of 400 cm^{-1} from Figure 3.6, αw=5.6×10^{-5}. Neglecting absorption within the blocking layer, 0.07% of incident photons will be absorbed within the depletion region of such a highly compensated device (Equation 1.7). Improvement can be made by further cooling the device, allowing higher bias to be applied without a large increase in

dark current, as shown in Figure 4.4. For an applied bias of 700 mV the depletion region thickness will be 25 nm, resulting in an absorption efficiency of 0.12%. This small absorption efficiency points to the importance of obtaining low compensation GaAs for the development of a high sensitivity BIB detector.

It has been observed that the compensation ratio, as determined based on the carrier concentration and Hall mobility within the model of Walukiewicz et al. [67], is always between 10 and 90% for LPE GaAs films regardless of the majority dopant concentration. To investigate the cause of the compensation, a film was grown with sufficiently high Te concentration such that the concentration could be determined by secondary ion mass spectrometry (SIMS). Hall effect analysis of the sample revealed a free electron concentration of 4×10^{17} cm^{-3} and a Hall mobility of μ=3240 cm$^2/Vs$ with an estimated compensation ratio of 0.35. The calculated compensation ratio was experimentally verified by SIMS analysis, which yielded a Te concentration of approximately 6×10^{17} cm^{-3}, indicating a compensation ratio of 0.33. SIMS analysis showed that the concentrations of the potential acceptor impurity species Mg, C, Si, Ge, and Zn were all below their respective detection limits, which range from 2×10^{16} cm^{-3} for C to 2×10^{15} cm^{-3} for Mg. All common GaAs acceptor species were therefore found to be of too low of concentration to account for the high compensation ratio of the film. This result suggests that a native defect is responsible for the compensation.

The self-compensation of heavily doped GaAs is explained by the Amphoteric Native Defect (AND) model [65], which proposes that as the Fermi level approaches a band edge the driving force for the creation of compensating vacancy and/or interstitial related

native defects increases. The formation of these defects counteracts the effect of adding donors or acceptors on the position of the Fermi level. In heavily doped n-type GaAs, as the Fermi level approaches the conduction band, the formation energy of As vacancy acceptor defects is reduced. This leads to an increase in the concentration of these defects during crystal growth, or during irradiation and annealing. If sufficient energy is added to the system, for example, by heavy electron irradiation, the Fermi level will approach a final Fermi stabilization energy which is a constant of the host material. It has been suggested by several authors [33, 22, 26] that the dominant compensating acceptor species in n-type GaAs samples is a Ga vacancy-donor complex. While the AND model does not apply to intermediately doped samples such as the absorbing layer of a GaAs BIB detector, the lack of evidence of a high concentration of an acceptor impurity and the scaling of the acceptor concentration with donor concentration is strong evidence suggesting a major role is played by native defects even at lower donor concentrations.

Neutron Transmutation Doping of GaAs

Neutron transmutation doping (NTD) of several high purity GaAs films grown on semi-insulating substrates was performed with the goal of producing homogeneous n-type doping with low compensation. NTD involves the absorption of a neutron by Ga and As atoms, resulting in transmutation by beta decay into Ge and Se, respectively. This occurs according to the reactions of Table 4.1 [2]. The GaAs NTD process creates only donor species. However, Ge is amphoteric and can act as an acceptor if it switches lattice sites to the As sublattice. The films were exposed to a thermal neutron flux inside a nuclear reactor at the UC Davis McClellan Nuclear Radiation Center [63]. The GaAs samples, sealed in

Reaction	**Neutron Capture cross-section [barns]**	**half-life**	**natural abundance**
$Ga^{69} \xrightarrow{n} Ga^{70} \xrightarrow{\beta} Ge^{70}$	1.68	21 min	0.6
$Ga^{71} \xrightarrow{n} Ga^{72} \xrightarrow{\beta} Ge^{72}$	4.86	14 h	0.4
$As^{75} \xrightarrow{n} As^{76} \xrightarrow{\beta} Se^{76}$	4.30	26 h	1.0

Table 4.1: The major transmutation reactions occurring in GaAs absorbing thermal neutrons. After [2].

welded Al tubing for water tightness, were held near the circumference of the cylindrical reactor vessel for 13 hours in a thermal neutron flux of approximately 6×10^{11} $cm^{-2}s^{-1}$. The total neutron dose was 3×10^{16} cm^{-2}. Placing the samples as far from the reactor core as possible is important for the reduction of the flux of fast neutrons, which have kinetic energies of over 1 MeV. Such neutrons can cause significant crystal damage upon impact with a lattice atom. The McClellan reactor neutron flux contains approximately 10% fast neutrons at the circumference.

Following irradiation the samples were isolated for 6 weeks to allow their radioactivity to decrease to acceptable levels. As irradiated, all samples were insulating due to significant crystalline damage incurred within the reactor. An annealing experiment was performed on sample 312, which was initially p-type with a free hole concentration of 2×10^{12} cm^{-3}. Four Ni/Ge/Au contacts were applied to the corners of the sample via electron beam evaporation. The sample was annealed for 30 seconds at a series of successively higher temperatures in a rapid thermal annealer (RTA) under an Ar ambient. A GaAs proximity cap was placed over the film surface during annealing to minimize the loss of As. The Hall effect and resistivity were measured at room temperature between each anneal. Anneal-

annealing temp [°C]	n_{300} [cm^{-3}]	ρ_{300} [Ω cm]	μ_{300} [cm^2/V s]	Θ
450	4.1×10^{7}	3.9×10^{7}	4300	
550	1.0×10^{8}	1.5×10^{7}	4230	
600	7.0×10^{8}	2.6×10^{6}	3370	
625	7.8×10^{13}	35.5	2250	
650	6.5×10^{14}	2.0	4820	
675	1.7×10^{15}	0.62	5970	0.85
700	2.3×10^{15}	0.41	6480	0.65
725	2.8×10^{15}	0.35	6515	0.55
750	2.9×10^{15}	0.33	6455	0.59

Table 4.2: Free carrier concentration, Hall mobility, and calculated compensation ratio for the NTD sample 312. The sample was initially p-type, with a free hole concentration of 2×10^{12} cm^{-3}. All anneals were performed in succession on the same sample.

ing continued until the resistivity became constant with annealing temperature. The free electron concentration of sample 312 as a function of annealing temperature is displayed in Figure 4.6. The Hall mobility and resistivity measured after each anneal is displayed in Table 4.2, along with the compensation ratio determined from [67]. The free electron concentration and other transport properties of the sample saturate at annealing temperatures above 725°C, with a compensation ratio of between 0.55 and 0.6. The films are highly compensated despite that the NTD process creates only donors. This is due either to the formation of compensating native defects, or to the migration of transmutation formed Ge atoms from the Ga to the As sublattice.

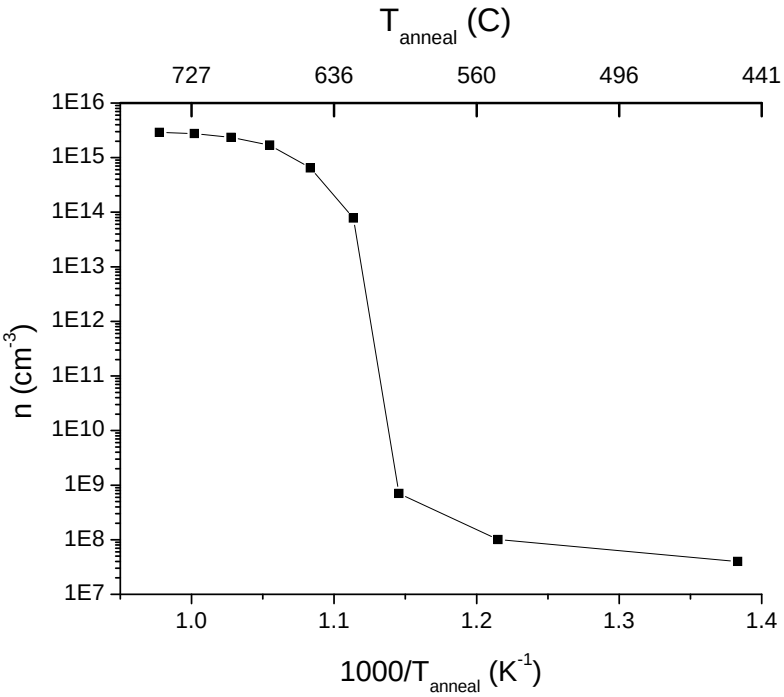

Figure 4.6: Free carrier concentration as a function of inverse annealing temperature for the NTD GaAs sample 312. The anneals were performed in succession on the same sample.

Chapter 5

Conclusion

It has been shown that the growth of GaAs films of sufficient purity to form the blocking layer of a BIB detector is possible by LPE. Extensive studies of the active impurity concentrations in these films by Hall effect and capacitance-voltage measurements have demonstrated that film purity near 1×10^{13} cm^{-3} can be repeatedly achieved. Te doped GaAs films with free electron concentrations between 2×10^{14} cm^{-3} and 2×10^{17} cm^{-3} have been grown by introducing bulk GaAs:Te into the Ga melt; however, the doping of these films could not be controlled with sufficient precision from run to run for the use as the BIB detector absorbing layer. The spectral dependence of the far-infrared absorption coefficient of n-type GaAs as a function of doping concentration has been determined by Fourier transform infrared spectrometry. While higher doping concentrations are desired to increase the absorption efficiency of the device, limitations exist due to the requirement that the impurity band and conduction band remain distinct. The measurement of the temperature dependence of the Hall effect and resistivity of a series of donor doped GaAs

films has revealed that the optimal doping concentration for the absorbing layer of a GaAs BIB detector lies between 1×10^{15} cm^{-3} and 7×10^{15} cm^{-3} since in this range the absorption coefficient is large but low temperature conduction is dominated by hopping in the impurity band.

A commercially grown VPE GaAs film doped with 5×10^{15} cm^{-3} sulfur, with more accurate doping and thickness control compared to LPE films, was obtained for use as the absorbing layer and as a substrate for the LPE blocking layer growth. This resulted in a functional BIB device in which the high purity blocking layer caused a significant reduction in the dark current when compared to the bare absorbing layer. The device did not exhibit extended far-infrared response, however, due to the high level of compensation within the absorbing layer. This meant that a high space charge concentration due to ionized minority acceptors limited the absorbing layer depletion width to values on the order of 10 nm.

Several high purity films were doped by neutron transmutation to a level of approximately 3×10^{15} cm^{-3} in an attempt to generate low compensation GaAs. After annealing of NTD sample 312, however, the mobility was found to be relatively low, most likely due to high compensation. The compensation in NTD and LPE grown films is believed to be due to the presence of native acceptor defects such as the Ga vacancy, the concentration of which scales with the donor doping concentration.

Chapter 6

Future Work

The results presented here have demonstrated the effectiveness of a GaAs BIB device in blocking the dark current that would otherwise limit the development of a standard photoconductor made from GaAs that has been doped between 1×10^{15} cm^{-3} and 1×10^{16} cm^{-3}. To measure the spectral response of the absorbing layer of the device, it will be necessary to either install an optical window or to place a far-infrared source such as an electrically heatable metal film [28] into the dewar containing a ^{3}He refrigerator capable of cooling to 300 mK. Based on the I-V curves of Figure 4.4 this will allow a significantly higher bias to be placed on the blocking layer without a large increase in dark current, than was possible in the 1.3 K photoconductivity measurements of Figure 4.5. Considerable effort is still required, however, to attain low compensation GaAs doped epitaxial films if the BIB device is to become a viable far-infrared detector. A study of compensation of LPE films as a function of the initial growth temperature and donor concentration would allow insight into the mechanism of acceptor formation and may reveal methods that could be used to

minimize it.

Additionally, further efforts are required to improve the lapping and polishing process used to acheive a blocking layer film of well controlled thickness and flatness. The polishing difficulties described in Section 4.2 include sloping of the blocking layer and use of a poor resolution thickness measurement system. An optical measurement system has been requisitioned which will improve the accuracy and precision of the blocking layer thickness measurement.

If the problems impeding the production of a single highly sensitive GaAs BIB detector can be solved, the production of arrays will require the use of a system capable of growing high-quality GaAs epitaxial films on larger substrates than are used in the LPE reactor used for this work. A centrifuge LPE system has been developed which is capable of film growth on 50 mm substrates. The centrifuge system has the potential to develop GaAs BIB detector arrays akin to those Si based BIB arrays that have become the most important detector in the mid-infrared (Figure 1.7).

Appendix A

Hydrogenic donor impurities in GaAs

A.1 The hydrogenic model

The electrical resistivity is a property that can vary over many orders of magnitude for different types of solids. The resistivity of insulating materials such as quartz is approximately 10^{20} Ωcm. Well conducting metals such as Cu and Au have resistivities as low as $10^{-6}\Omega$cm. These two types of materials differ in their resistivity by a factor of 10^{26}, more than any other physical material property in nature. High purity semiconductors such as Si and GaAs have a relatively high electrical resistivity at room temperature however the resistivity can be greatly reduced by the addition of certain types of impurities. For example the addition of group VI donor impurities such as Se or Te into GaAs can decrease the resistivity because they have an extra valence electron compared to the As they replace

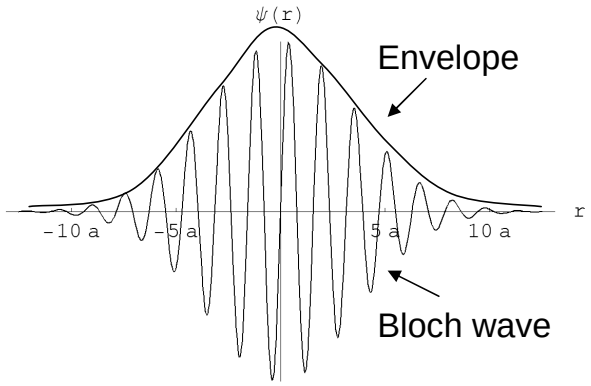

Figure A.1: The ground state wavefunction of a shallow donor electron in GaAs is a Bloch function modulated by a 1s hydrogenic envelope function.

substitutionally. The addition of acceptor impurities such as Zn and Mg have one fewer valence electron compared to Ga and contribute a positive hole as a charge carrier, which can also decrease the resistivity. The theoretical treatments of both of these types of impurities are fundamentally similar. Because the BIB device is entirely n-type, only the former will be discussed here. In the following section, a simple model describing the effect of such impurity substitutions is described.

A Te atom which occupies a substitutional site on the As sublattice of GaAs acts as an electron donor because it has six valence electrons in its outermost orbital compared to only five for As. It also has an extra proton compared to the As atom which it replaces. The sixth impurity electron cannot participate in bonding between the Te atom and its neighboring Ga atoms; however, it still interacts with the coulomb field of the excess proton. The electron-proton coulomb interaction within the GaAs matrix can be modeled as a hydrogen atom that has been screened by the lattice. The wavefunction of a donor electron is of the form of a Bloch function that has been modulated by a hydrogenic envelope function localized at the defect center (Figure A.1). Such donors are therefore frquently referred to

as hydrogenic, or shallow level impurities. The energy states of an electron interacting with a proton in a Hydrogen atom are given by

$$E_n = \frac{1}{n^2}\frac{mq^4}{8\epsilon_o h} \quad , \tag{A.1}$$

where n is the principal quantum number, m is the electron mass, and h is the Planck constant. Equation A.1 can be applied to hydrogenic donors in a semiconductor if the effects of screening of the coulomb potential from the surrounding lattice and the change in electron mass due to the periodic potential of the crystal are accounted for. These effects can be calculated within the effective mass approximation (EMA). For a review of Effective Mass theory, see Reference [71]. The EMA is particularly well suited for semiconductors that have an isotropic, nondegenerate conduction band minimum, such as GaAs. The effective mass of an electron occupying a state inside a spherically symmetric conduction band minimum is related to the curvature of the band

$$m^* = \hbar^2 \left[\frac{d^2E}{dk^2}\right]^{-1} . \tag{A.2}$$

The effective mass of an electron in GaAs is only a fraction of the free electron mass, m^*=.0665m_o.

The screening of the electron-proton interaction can be accounted for by the static dielectric constant of GaAs. The relative static dielectric constant is a complex function of position within in the unit cell, and depends upon the charge polarization due to the proton-like impurity center, the valence band electrons localized in bonds, and the weakly bound donor electron. The average dielectric constant ϵ_{GaAs} can be used as an approximation, however, if the electron probability density is assumed to be widely spread over many

thousand lattice points. Due to the relatively weak interaction between the electron and Te impurity, the electron Bohr radius is expected to be much larger than in the hydrogen atom (of the order of 10 or more times the lattice constant). The use of the average dielectric constant of GaAs is therefore justified by the wide distribution of the electron probability density. By substiting m=m^* and ϵ=$\epsilon_o\epsilon_{GaAs}$, the hydrogen atomic energy states of Equation A.1 are representative of the energy states of a hydrogenic donor in GaAs

$$E_n = \frac{1}{n^2}\frac{m^* q^4}{32\pi^2(\epsilon_o\epsilon_{GaAs})^2\hbar^2} \ . \tag{A.3}$$

The corresponding effective Bohr radii are:.

$$a_n = n^2\frac{4\pi\epsilon_o\epsilon_{GaAs}\hbar^2}{m^* q^2} \ . \tag{A.4}$$

The ground state binding energy (n=0) for hydrogenic donors in GaAs, calculated using m^*=.0665m_o and ϵ_{GaAs}=12.56ϵ_o, is found to be 5.71 meV, with an effective Bohr radius of 103 Å. This agrees well with the experimental value of 5.9 meV determined by photoconductivity measurements on high purity, unintentionally sulfur doped GaAs, shown in Figure A.2. The hydrogenic impurity model yields an energy of 4.29 meV for the transition from the n=1 ground state to the n=2 excited state (1s-2p). This transition is observed at approximately 4.4 meV in the spectrum of Figure A.2. The binding of the electron to an impurity donor atom is relatively weak, and at room temperature the donor will be ionized with the electron lifted into the conduction band.

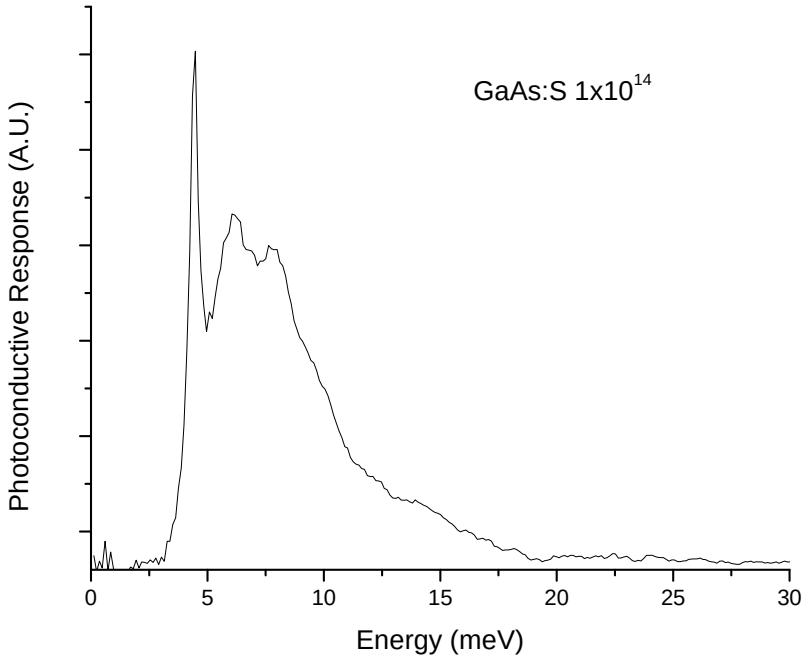

Figure A.2: Photoconductivity spectrum of a high-purity, n-type GaAs homoepitaxial LPE film at T=4.2K. The 1s to conduction band transition is centered at 5.9 meV and the 1s to 2p excited state transition is at 4.4 meV.

A.2 The central cell correction

The hydrogenic model is valid as long as the wavefunction of the donor electron is spread over many unit cells. When the probability density is far removed from the donor atom, it interacts only weakly with the local hydrogenic potential. Under these circumstances, the electron wavefunction and its corresponding eigenvalues do not have a strong dependence on the chemical identity of the impurity atom. This is found to be the case for GaAs, in which the ground state ionization energies for many shallow dopants are very similar to each other and are well predicted by the hydrogenic model. In other semiconductor materials, such as Si and Ge, the electron is more strongly bound to the impurity center due to its larger effective mass. In this case, the electron probability density is on average

Impurity	Binding Energy (meV)	Central Cell Correction (meV)
Si_{Ga}	5.84^b	0.059^c
S	5.87^b	0.11^c
Sn	5.88^b	0.07^a

Table A.1: Experimentally determined binding energies and central cell corrections of shallow level donors in GaAs. References: a) [5], b) [3], c) [31].

closer to the impurity center, and the local potential surrounding the donor atom has a significant effect. This effect poses a limitation to the validity of the hydrogenic model for the ground state. In Si and Ge, it is found that the experimentally determined ionization energies vary with the donor species and differ from the value predicted by the hydrogenic model even when the anisotropy and degeneracy of the conduction band minimum are taken into account [71]. The difference in the experimental ionization energy from the theoretical value is known as the central cell correction.

The central cell correction is believed to be due to the lattice distortion caused by the size and electronegativity mismatch of the substitutional impurity compared to the host material [36]. Since donor ionization energies in GaAs are relatively insensitive to the impurity species, the central cell corrections are small. The ionization energies and central cell corrections of Si, S, and Sn impurities in GaAs, which have been determined by high resolution photoluminescence spectroscopy are given in Table A.1 [3]. Excited states of a donor electron wavefunction may be well predicted by the hydrogenic model even if the ground state binding energy of a donor is not. This is due to the smaller binding energy and correspondingly larger Bohr radius associated with the excited states, which reduces the effect of the central cell compared to the ground state. Additionally, states with p-orbital symmetry are expected to be better fit by the hydrogenic model because they contain a

node at the origin, in contrast to s-orbital states.

Appendix B

Impurity conduction in semiconductors

B.1 Low temperature conduction in doped semiconductors

Hydrogenic impurities, in the limit of low concentration, create discrete electronic energy states within a semiconductor host. These states typically occupy the forbidden energy gap near one of the band edges. The low temperature electrical properties of a doped semiconductor depend greatly upon the concentration of both the majority and minority impurity species. Considering the case of donor impurities with no compensating acceptors electrical conduction can occur via two mechanisms. The first is the thermal excitation of a bound electron (by absorption of an acoustic phonon) into the conduction band. The conductivity due to this mechanism depends exponentially on the ratio of the

donor electron binding energy ϵ_1 to the available thermal energy, $k_{\mathrm{B}}T$ (Equation B.1).

$$\sigma = \sigma_1 e^{-\frac{\epsilon_1}{k_{\mathrm{B}}T}} \tag{B.1}$$

At very low temperature, the thermal energy required for electronic excitation into the conduction band is not available and all donor states will be occupied by electrons. Under these circumstances electrical conduction is believed to occur by removing an electron from a neutral donor site and transferring it to neighboring sites, creating an overcharged impurity state[50]. The characteristic excitation energy for this process ϵ_2 is a function of the average distance between impurity centers. This thermally activated form of conduction has is similar to the ϵ_1 conduction described above.

$$\sigma = \sigma_2 e^{-\frac{\epsilon_2}{k_{\mathrm{B}}T}} \tag{B.2}$$

In the presence of compensating acceptor impurities a third conduction mechanism becomes active. The minority acceptors will be ionized by electrons, creating an equal number of ionized donors. Under an applied electric field, an electron in a neutral donor state can move to a neighboring empty site via the absorption and subsequent emission of a phonon. This process is shown in Figure B.1. The electron is excited into an intermediate state * by the absorption of a phonon. Hopping conduction occurs by the relaxation of this electron into a neighboring ionized donor site. As in the case for ϵ_2 type conduction, the activation energy ϵ_3 depends on the average distance between impurity centers. In addition, ϵ_3 is a function of the compensation ratio, which determines the concentration of empty states into which an electron can move. This conduction mechanism is known as nearest neighbor hopping, and has a mathematical form given by Equation B.3.

$$\sigma = \sigma_3 e^{-\frac{\epsilon_3}{k_{\mathrm{B}}T}} \tag{B.3}$$

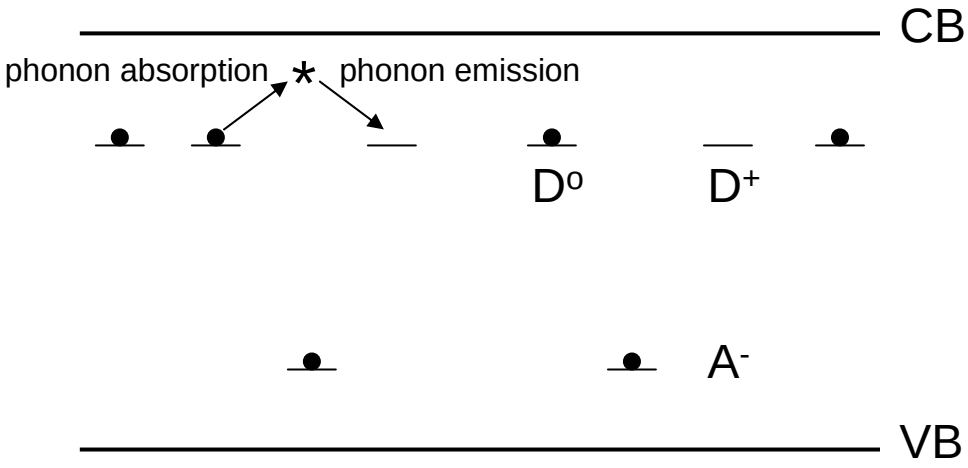

Figure B.1: Schematic band diagram of an n-type semiconductor showing the process of nearest neighbor hopping conduction. Both neutral (D^o) and empty donor sites (D^+) exist as some donors have lost their electrons to compensating acceptors (A^-).

At still lower temperatures another mechanism known as variable-range hopping can become significant. Variable-range hopping occurs when only a very small amount of thermal energy exists for excitation of an electron. The electron is then limited to hopping to available states which are within an energy $k_B T$ of its original energy. The neighboring available states may not satisfy this condition, meaning that the electron must hop to a free state that could be several neighbor spacings away.

Nearest neighbor hopping conduction in semiconductors can be studied by examining the temperature dependence of the resistivity. The results of Fritzsche and Cuevas [25], who studied the resistivity of neutron transmutation doped, p-type germanium, are given in Figure B.2. The resistivity of the most lightly doped sample (7.5×10^{14} cm^{-3}) reveals two predominant conduction mechanisms. At higher temperatures, conduction is thermally activated with an activation energy ϵ_1 corresponding to the donor ground state to valence band transition. As the temperature is lowered, the slope of the resistivity curve shifts to

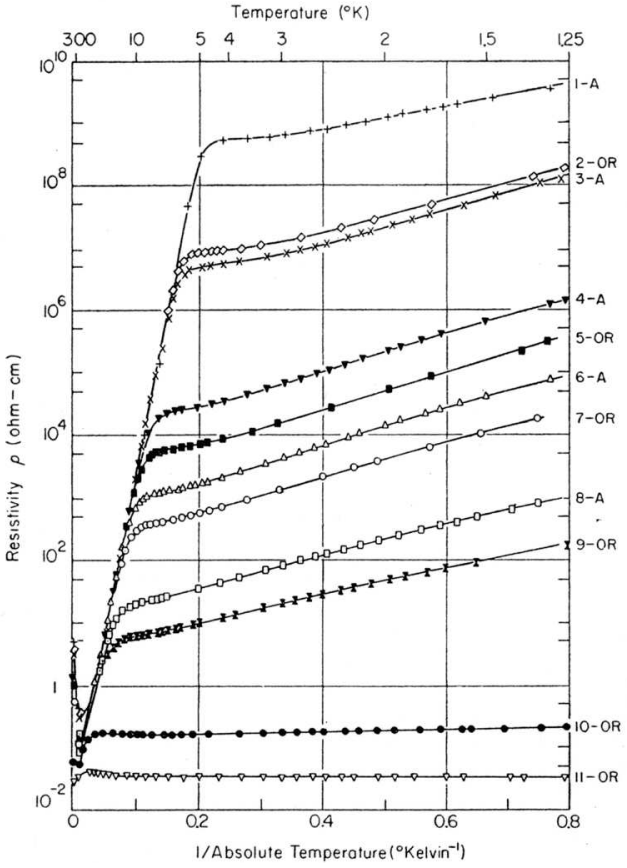

Figure B.2: The temperature dependence of the resistivity of neutron transmutation doped, p-type Ge for acceptor concentrations ranging from 1.35×10^{18} (sample 11-OR) to 7.5×10^{14} (sample 1-A). After [25].

a much smaller value, indicating the transition to hopping conduction, with an activation energy $\epsilon_3 < \epsilon_1$. The resistivity of the most heavily doped sample (1.35×10^{18} cm^{-3}) is independent of temperature, indicative of metallic conduction. An excellent review of hopping conduction in semiconductors is given by Shklovskii and Efros [59].

B.2 Delocalization and the transition to metallic conduction

In the low concentration limit discussed in Section B.1 the overlap between the valence electronic wavefunctions of neighboring donor centers is weak and electrons are localized at a single donor site. Within this regime, the conduction of localized electrons is thermally activated. When the doping is increased beyond a critical value that depends upon the semiconductor and dopant species under study, the conductivity switches to metallic in character. This phenomenon is known as a metal-insulator transition (MIT). Despite many years of research into the MIT some questions remain. Two simplified models proposed by Mott [49] and Anderson [4] yield predictions for the critical concentration that agree reasonably well with experiment. The Mott model is based on the electron-electron interaction within an ordered array of atoms. The Anderson model is based on a single electron approximation, and localization is caused by disorder in the location of dopant atoms within the semiconductor host.

B.2.1 The Mott transition

At donor concentrations that are high compared to those discussed in Section B.1, electronic wavefunctions associated with each donor center will overlap, leading to a

dispersion of their eigenvalues according to the Pauli exclusion principle. At a sufficiently high concentration a continuous band of states will form. The activation energy ϵ_2 for conduction in the low temperature, no compensation case described above can be modeled as a band gap separating the neutral donor band D^o and the overcharged band D^-. These two bands are commonly called the lower and upper Hubbard bands, respectively. Figure B.3 shows the density of states of the Hubbard bands as a function of impurity concentration. At very low concentration, the neutral and overcharged states are discrete and separated by an energy U. Mott [49] estimated the so called Hubbard U as the energy required to remove an electron from one neutral donor atom and place it on another neutral donor atom, creating the overcharged state. This estimate is given in Equation B.4, where κ is the dielectric constant of the host material and e is the electronic charge.

$$U = \frac{5e^2}{8\kappa a} \tag{B.4}$$

Mott also suggested that the Hubbard U is equivalent to the ϵ_2 activation energy discussed above [49]. As the concentration is increased, the levels broaden into bands, and at a critical concentration, given by n_c in the Figure, the two bands will merge.

We can obtain a more detailed understanding of impurity band formation by considering the model of donor atoms with Bohr radius a occupying a simple cubic lattice of spacing b, within a semiconductor host. The lattice is a periodic series of potential wells in which electron wavefunctions take the form of a Bloch function, defined by Equation B.5, where $\mathbf{k}$ is the wavevector, $\mathbf{R}_n$ is the site of the nth lattice site, ϕ is the atomic wavefunction, and $\mathbf{r}$ is the relative spatial position.

$$\psi_k = \sum_n e^{i\mathbf{k}\cdot\mathbf{R}_n}\phi(\mathbf{r} - \mathbf{R}_n) \tag{B.5}$$

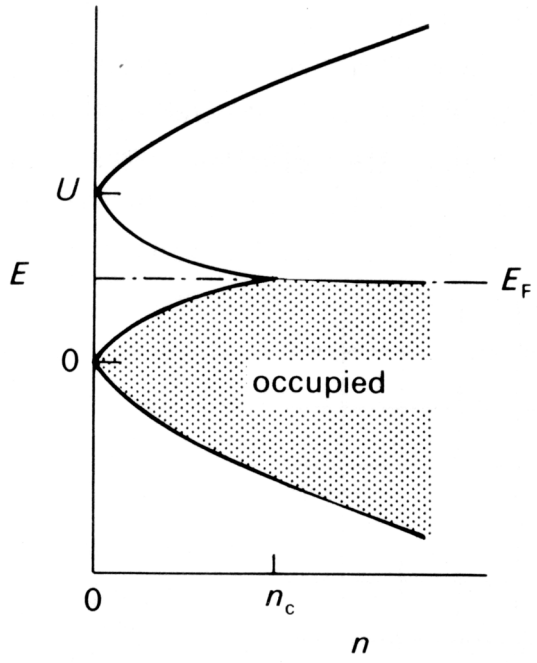

Figure B.3: Schematic density of states for the lower and upper Hubbard bands as a function of doping concentration. The concentration at which the two bands merge is given by n_c. After [38].

The matrix element corresponding to the Hamiltonian between neighboring lattice sites is given by the overlap integral (I), and gives a measure of the degree of interaction between neighboring states.

$$I = \langle \phi^* | H | \phi \rangle = \int \phi^*(\mathbf{r} - \mathbf{R}_\mathrm{n}) H \phi(\mathbf{r} - \mathbf{R}_\mathrm{n}) d\mathbf{r} \tag{B.6}$$

For the case of hydrogenic donors, the overlap integral has been estimated to be exponentially proportional to the ratio of the Bohr radius to the lattice spacing, times a numerical constant β [59].

$$I \propto exp^{\frac{-\beta b}{a}} \tag{B.7}$$

At low doping concentration the impurity spacing b will be large, and I will be relatively small. At sufficiently high concentration, the dispersion that results from the proximity of the electrons at each potential leads to the formation of a continuous impurity band, with a bandwidth of approximately B=$2zI$, where z is the coordination number (number of nearest neighbors). Mott considered this band to be the lower Hubbard band described above. In the absence of compensation, the impurity band will be full of electrons, with the Fermi level situated at the top of the lower Hubbard band, and the system will be an insulator. The transition to metallic behavior, or Mott transition, occurs when the top of the lower Hubbard band merges with the bottom of the upper Hubbard band. This causes the activation energy ϵ_2 to vanish, allowing electrons near the Fermi level to become delocalized.

Once the electrons are delocalized, the system becomes metallic, exhibiting a finite conductivity at T=0 K. The critical concentration of the metal-insulator transition in the

Material	a (Å)	n_c (cm^{-3})
Si	19	2.26×10^{18}
Ge	39	2.62×10^{17}
GaAs	100.5	1.54×10^{16}

Table B.1: Approximate metal-insulator transition critical concentrations for n-type and p-type impurities in Si, Ge, and GaAs calculated using Equation B.8.

Mott model is given by Equation B.8.

$$n_c = \left(\frac{.25}{a}\right)^3 \tag{B.8}$$

The Mott critical concentration for common dopants in Si, Ge, and GaAs are given in Table B.1.

B.2.2 The Anderson transition

Within the Anderson model [4], electron localization in an n-type semiconductor occurs due to the disorder of donor impurity states in the crystalline host. For a perfect lattice of donor atoms in a semiconductor with high enough doping concentrations such that electronic overlap is significant, electrons will be delocalized, their probability densities spread evenly throughout. As disorder is introduced into the system however, the phase factor of Equation B.5 becomes a random function, and the spread of electron wavefunctions within the crystal will decrease. In order to examine the effects of disorder on the perfectly periodic system described above, Anderson considered a random variation in the potential well depth, while maintaining a regular well spacing. In this analysis, the well potential was taken to be $V + V_o$ where V_o represents the spread of potential well values. According to the theory, the state of electrons in a system depends on the size of the dimensionless ratio V_o/I. For a system of a given potential spacing, electrons will be localized at high

levels of disorder (when V_o is large), or at low donor concentration, when the overlap is small. As the lattice sites are brought closer together, the degree of overlap will cause I to increase and lead to delocalization. Anderson predicted a critical value for V_o/I, known as the Anderson transition, similar to the Mott transition, below which electrons will be delocalized. The critical value of Anderson's parameter has been estimated to be V_o/I=15 for impurities on a simple cubic lattice. This corresponds to a critical value of V_o/B=1.25, where B is the impurity bandwidth.

Within an impurity band, extended and localized states may coexist. As the impurity band broadens with increasing impurity concentration, only states near the band edges will have a value of V_o/I high enough to ensure localization. The middle of the band will contain extended states, as illustrated in Figure B.4. In this case, localized and extended states are separated by a critical energy E_c which is known as the mobility edge. The MIT occurs when the Fermi level crosses over the mobility edge, by means of increased doping or temperature, from a state that is localized, having zero conductivity at T=0 K to one that is extended, having a finite conductivity at all temperatures.

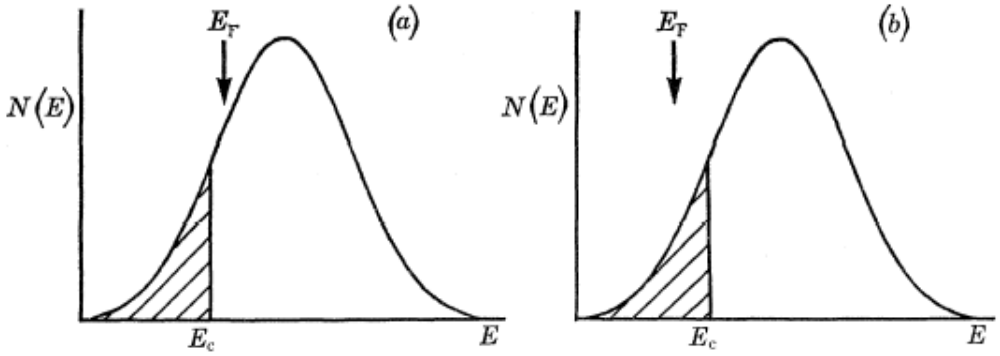

Figure B.4: Density of states for an impurity band in a semiconductor. Shaded areas contain Anderson localized states while the unshaded are delocalized. The system is metallic when the Fermi level is outside the shaded region as in (a). In (b) the Fermi level is within the localized states and the system is insulating. After [48].

Appendix C

Fourier transform spectroscopy

Energy dispersion in optical spectrometers is usually obtained by directing a broad-band, high-intensity light source through a monochrometer. In the monochrometer, the light is dispersed by a prism or grating, and the specific frequency desired is selected using a slit that intersects the emission from the dispersive element at a certain angle. The resolution depends on the width of the slit, and can be improved by adding additional dispersion elements, which divide the light even further. Such systems are known as double or triple monochrometers. This technique of frequency selection, however, causes the beam to be greatly attenuated upon reaching the sample. Contrary to dispersive optical spectrometers, Fourier transform spectrometers incorporate a Michelson interferometer which creates energy resolution via interference instead of gratings or prisms. The operation of Fourier transform spectrometers and their advantages over dispersive spectrometers are discussed here.

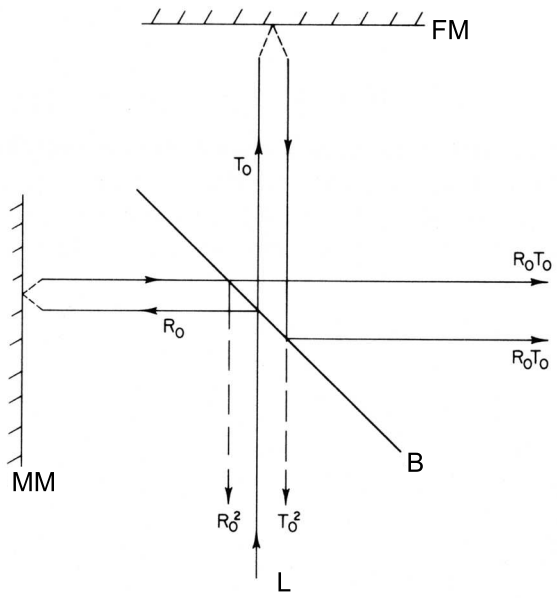

Figure C.1: Schematic drawing of a Michelson interferometer showing the reflected (R) and transmitted (T) intensities resulting from a light source (L) incident on the beamsplitter (B). The fixed mirror (FM) and moving mirror (MM) are perpendicular. After [11].

C.1 The Michelson Interferometer

The interferometer is the most important part of a FTS system. It was conceived of by Michelson in 1891 and consists of a light source, a semi-reflecting membrane known as a beamsplitter, and two mirrors. One mirror is stationary and one is movable. The beamsplitter is positioned typically at 45° to the two mirrors, which are perpendicular to each other. A schematic of an interferometer is shown in Figure C.1. In the following analysis adapted from Bell [11], consider a beam of monochromatic light from the source L that is incident on the beamsplitter (B). At the beamsplitter a fraction R_o of the source intensity is reflected toward the moving mirror and a fraction T_o is transmitted to the fixed mirror, as detailed in Figure C.1. The split photon fluxes reflect off their respective mirrors and recombine at the beamsplitter, where they again undergo partial transmission

and reflection. At the output of the interferometer, each beam has a fraction R_oT_o of the initial intensity, giving a total intensity of $2R_oT_o$. The maximum possible output for the interferometer occurs if $R_o = T_o$=0.5. Bell [11] has defined the relative efficiency (RE) of an interferometer as the ratio of the actual output intensity to the ideal value of 50% of the source intensity.

$$RE = \frac{2R_oT_o}{(2R_oT_o)_{\text{ideal}}} = 4R_oT_o \tag{C.1}$$

If the mirrors are equidistant from the beamsplitter, the two split beams will be exactly in-phase when they exit the interferometer, resulting in constructive interference and the brightest possible output. This position is known as "zero path", since the path difference between the two beams is zero. If the movable mirror is shifted by a distance d, there will be a path difference δ=2d between the two beams. The path difference results in partial deconstructive interference between the two beams and a decrease in the output intensity. The interference pattern that results from the motion of the mirror is known as an interferogram (intensity vs. mirror position). For a monochromatic beam, the interferogram is a pure cosine function (Figure C.2(a)). The spectrum is generated by computing the Fourier transform of the interferogram. In the limit of infinite mirror motion, the spectrum (intensity vs. frequency), takes the form of a delta function at the frequency of the source.

To determine the output intensity (I) of a Michelson interferometer for a polychromatic source we will consider a single photon energy in detail, and generalize it to the broadband case. The electric fields of two photons of wavenumber σ that have been phase shifted by the beamsplitter with a path difference δ are

$$E_1 = E_o(\sigma)e^{i2\pi\sigma z} \tag{C.2}$$

$$E_2 = E_{\rm o}(\sigma)e^{i2\pi\sigma(z-\delta)} \ . \tag{C.3}$$

The intensity (or irradiance) of a photon is determined by Maxwell's equations to be $\frac{1}{2}c\epsilon_{\rm o}\left|E\right|^2$, where E is the photon electric field, $\epsilon_{\rm o}$ is the permittivity of free space, and c is the speed of light. By the principle of superposition, the total photon intensity is additive, and the sum of the intensity of two photons is

$$\begin{aligned} I_1 + I_2 &= \frac{1}{2}c\epsilon_{\rm o}\left|E_1(\sigma) + E_2(\sigma)\right|^2 & \text{(C.4)} \\ &= \frac{1}{2}c\epsilon_{\rm o}\left[E_1(\sigma)\cdot E_1^*(\sigma) + 2E_1(\sigma)\cdot E_2^*(\sigma) + E_2(\sigma)\cdot E_2^*(\sigma)\right] & \text{(C.5)} \\ &= \frac{1}{2}c\epsilon_{\rm o}\left[E_{\rm o}^2 + 2E_{\rm o}^2 e^{i2\pi\sigma\delta} + E_{\rm o}^2\right] & \text{(C.6)} \\ &= c\epsilon_{\rm o}E_{\rm o}^2(\sigma)\left[1+\cos(2\pi\sigma\delta)\right] \ . & \text{(C.7)} \end{aligned}$$

The interferometer output intensity for a broadband source as a function of the path difference is determined by taking the sum of the intensity over all wavenumbers

$$\begin{aligned} I_{\rm T}(\delta) &= \int_0^\infty I(\sigma,\delta)d\sigma & \text{(C.8)} \\ &= c\epsilon_{\rm o}\left(\int_0^\infty E_{\rm o}^2(\sigma)d\sigma + \int_0^\infty E_{\rm o}^2(\sigma)\cos(2\pi\sigma\delta)d\sigma\right) \ . & \text{(C.9)} \end{aligned}$$

Since the intensity at zero path difference (δ=0) is

$$I_{\rm T}(0) = 2c\epsilon_{\rm o}\int_0^\infty E_{\rm o}^2(\sigma)d\sigma, \tag{C.10}$$

we can write

$$\begin{aligned} F(\delta) &= I_{\rm T}(\delta) - \frac{1}{2}I_{\rm T}(0) & \text{(C.11)} \\ &= c\epsilon_{\rm o}\int_0^\infty E_{\rm o}^2(\sigma)\cos(2\pi\sigma\delta)d\sigma & \text{(C.12)} \end{aligned}$$

for the interferogram. The spectrum is obtained by taking the Fourier transform of Equation C.12

$$F(\sigma) = c\epsilon_{\mathrm{o}} \int_0^\infty F(\delta) \cos(2\pi\sigma\delta) d\delta \ . \tag{C.13}$$

Equation C.13 is the fundamental equation for Fourier transform spectroscopy which relates the spectral intensity of the interferometer output to the change of position of the moving mirror. The interferogram is recorded by an optical detector and the transformation is performed numerically by a computer. The lack of availability of computers of high enough speed to perform the numerical transform delayed the development of Fourier transform spectroscopy until recent decades.

Figures C.2(b) and C.2(c) demonstrate the interferograms resulting from two different kinds of polychromatic spectra. The peak of finite width in Figure C.2(b) is composed of multiple Fourier cosine components. This is generated by a modulated interferogram with complete constructive interference at δ=0 . The interference becomes increasingly destructive, however, as the path difference is increased, at a rate that is proportional to the bandwidth. For the broadband spectrum of Figure C.2(c), the interferogram amplitude is quickly reduced to half the value at zero path difference due to the large bandwidth.

C.2 Advantages of Fourier transform spectroscopy

In Fourier transform spectroscopy (FTS), light reaches the sample after traveling through an interferometer. The spectrum is obtained by taking the Fourier transform of the sample's response to the interferometer output. FTS offers two major advantages over conventional dispersive spectroscopy, as discussed by Bell [11]. The first advantage is that

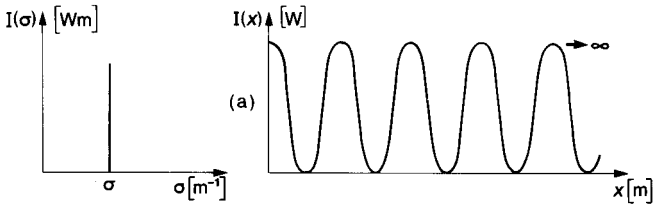

(a)

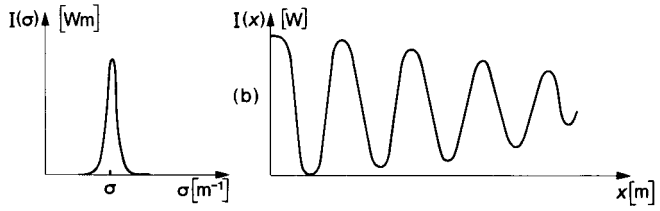

(b)

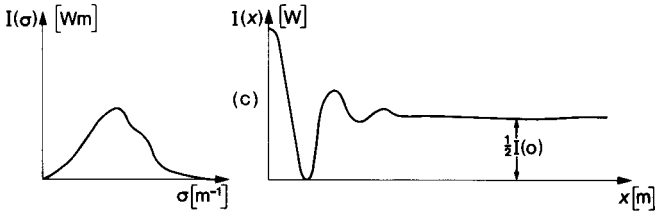

(c)

Figure C.2: Examples of three different spectra and their interferograms: a) a monochromatic spectrum , b) a single peak of finite width, c) broadband response. After [17].

each measurement of the output intensity contains information about all light frequencies emitted from the source. In a conventional spectrometer, only the narrow spectral region that is selected by the instrument is observed at any given time. A conventional spectrometer requires 10,000 separate measurements to obtain the intensity of 10,000 separate frequencies. In contrast, a 10,000 point interferogram recorded by a FTS system will have sampled each frequency 10,000 times. This is known of the Fellgett or multiplex advantage [24]. The second advantage is due to the higher brightness of the light incident on the sample from an interferometer source. The resolution of a conventional spectrometer increases as the slit width is made smaller, which reduces the total power on the sample. In an FTS system, the resolution is determined by the total length over which the moving mirror travels, allowing high intensity even at very high resolution. The increased intensity from a FTS system leads to a higher signal to noise ratio. This is known as the Jacquinot or throughput advantage.

C.3 The effect of the beamsplitter

The power output of the interferometer is not the same for all frequencies. The output bandwidth is determined both by the spectrum emitted by the source lamp and the type of beamsplitter used. The latter effect is due to interference and absorption effects within the beamsplitter. When light encounters a beamsplitter surface it is partially reflected and partially transmitted. The relative amounts of reflection and transmission depend on the reflectivity and hence upon the refractive index of the beamsplitter material. Figure C.3 shows the ray trace for light incident on a Mylar beamsplitter at 45°, with a

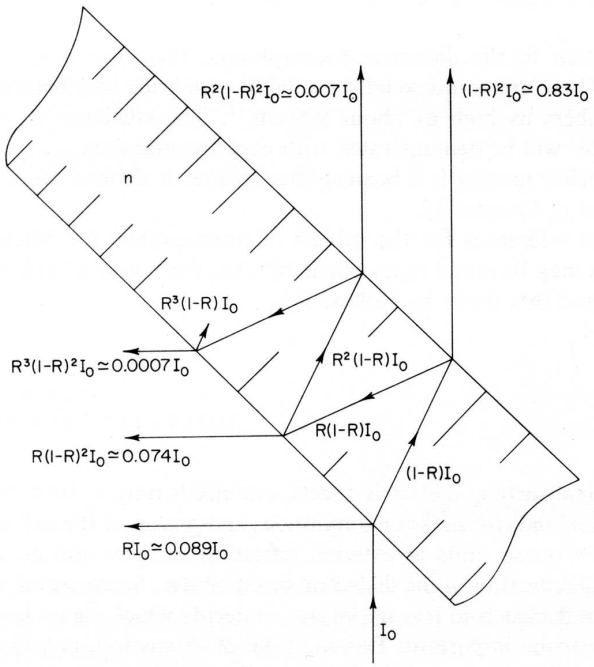

Figure C.3: The initial intensity I_o of a beam incident upon a Mylar beamsplitter at 45° is divided into several reflected and transmitted beams. After [11].

reflectivity of R=0.089. A fraction R of the initial beam intensity I_o is reflected at the beamsplitter outer surface. The transmitted beam has an intensity of $(1 - R)I_o$. This process is repeated each time the light encounters an interface.

In the example of Figure C.3, light of intensity I_o incident on the first surface is partially reflected ($0.089I_o$) before being transmitted into the Mylar film. The beam is transmitted through the beamsplitter body and again partially reflected at the back surface. The transmitted beam that exits the beamsplitter after these first two reflections contains 0.83% of the initial intensity. The second reflected beam undergoes successive transmissions and reflections at the two surfaces in a process known as multiple internal reflection. It is important to note that the primary transmission of 83% completely dominates the secondary transmission of $0.007I_o$, while the first two reflected beams of intensity $0.089I_o$ and $0.074I_o$

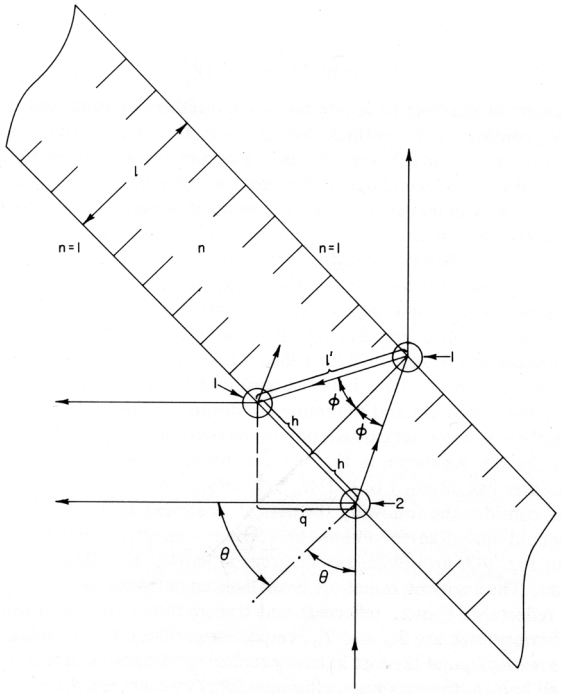

Figure C.4: Detailed ray trace of the first two reflected beams from a beamsplitter of refractive index n, and thickness l, angled at 45°. The circled points labeled 1 represent internal reflection. The circled point 2 is an external reflection, giving a phase shift of π. After [11].

are similar in magnitude. The first two reflected beams, which are now phase shifted due to the 45° angle of the beamsplitter, will undergo interference. This process is shown in greater detail in Figure C.4.

Since the two reflected beams are of nearly the same intensity, we can take R_o=2R, where R is the reflectivity of the beamsplitter material. Furthermore, since the first transmitted beam is much more intense than the successive beams, and since it has undergone two reflections, one at the exterior surface, and one at the interior surface, before exiting the beamsplitter, we can relate T_o=(1-R)^2.

The distance traveled by the second beam, within the beamsplitter bulk, is rep-

resented by $2l'$ in Figure C.4. For the external reflection at point 2 there is a phase shift of π, but no phase shift occurs for the internal reflections at either point labeled 1. The path difference between the two beams is determined by the extra distance traveled by the secondary beam, $2l'$, scaled by the refractive index. From this value, the distance q, which is due to the angle of the beamsplitter, is subtracted to give the total path difference (Equation C.14).

$$\delta = 2nl' - q \tag{C.14}$$

Because of the π phase shift between the two beams, constructive interference will occur when the path difference is equal to a half integer value of the wavelength. Destructive interference will occur for path differences of whole integer values of the wavelength. The interference condition can be related to the beamsplitter material and physical dimensions by applying Snell's law to the geometry of figure C.4. If the two reflected beams are approximated to have the same intensity, their phase relation ρ, according to Bell [11], is given by Equation C.15.

$$\rho = 2\pi \left[\sigma l \left(n^2 - \frac{1}{2} \right)^{\frac{1}{2}} + \frac{1}{4} \right] \tag{C.15}$$

Taking the approximation that the two reflected beams are of the same amplitude, the intensity of the beam resultant from their interference, I_r, depends on the phase difference according to Equation C.16.

$$\frac{I_\mathrm{r}}{I_\mathrm{o}} = 4\cos^2\rho \tag{C.16}$$

Combining the results of Equations C.15, C.16, and the relations for R_o and T_o in terms of R with Equation C.1, the relative efficiency of a beamsplitter as a function of photon

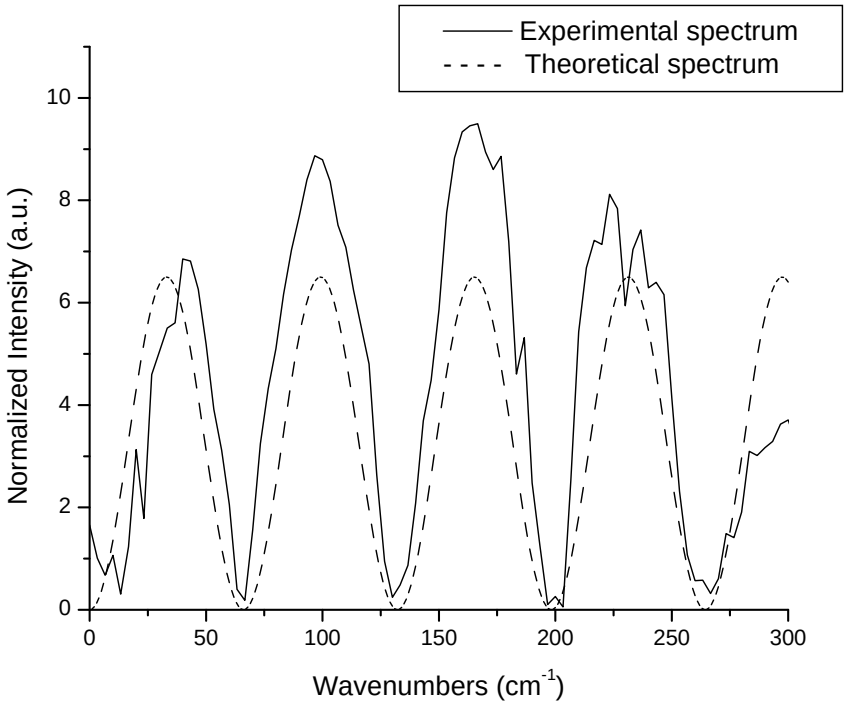

Figure C.5: The experimental interferometer intensity curve for a 51 μm thick Mylar beamsplitter along with the theoretical prediction of Equation C.17.

energy is obtained.

$$RE = 8\left(1-R\right)^2 R\cos^2\left\{2\pi\left[\sigma\left(n^2-\frac{1}{2}\right)^{\frac{1}{2}}+\frac{1}{4}\right]\right\} \tag{C.17}$$

Equation C.17 is plotted in Figure C.5 for a 51 μm thick Mylar beamsplitter along with the experimentally determined intensity curve. The reflectivity of Mylar for wavelengths in the far-infrared is approximately R=0.16, and the refractive index is n=1.67 [20]. The intensity minima are well predicted. The beamsplitter material and thickness must be chosen to provide intensity in the bandwidth of interest. Common types of beamsplitters that have been adopted for use in FT spectrometer systems include dielectric sheets, such as Mylar and polyethylene, and metal films deposited on various substrates.

C.4 Apodization

The Fourier integral of Equation C.13 is defined over an infinite limit. Since the travel distance of the moving mirror is finite the computed transform will vary from the actual spectrum. The effect of having finite integration limits is to broaden and distort the spectrum. As an example, consider the case of a 7 cm^{-1} monochromatic source with a moving mirror travel distance of 7 cm. The interferogram for this case, as stated earlier, is a cosine function. The actual spectrum for a monochromatic source is a delta function; however, the calculated spectrum shows a broadened peak. The solid line of Figure C.6(b) shows the resulting spectrum for the case of no apodization. It contains significant side lobes and non-physical negative values away from the primary peak. The spectrum artifacts caused by the finite motion of the mirror are reduced by manipulating the interferogram and forcing it to zero at the limit of travel. This can be accomplished by multiplying the interferogram by a function such as a triangle, which has zero value at the extreme of the mirror motion distance, as shown in Figure C.6(a). The dashed line of Figure C.6(b) is the spectrum that results from the Fourier transform of this apodized interferogram. While the central peak has widened somewhat, the side lobes have been greatly reduced in intensity and there are no longer negative values in the spectrum. As a rule, apodization causes a reduction in resolution but is important for the removal of artifacts. The apodization process also has the benefit of favoring the higher intensity fringes (those closer to the zero path) in the interferogram. These fringes have a better signal to noise ratio compared to those recorded at large δ, and their augmentation leads to a cleaner, lower noise spectrum.

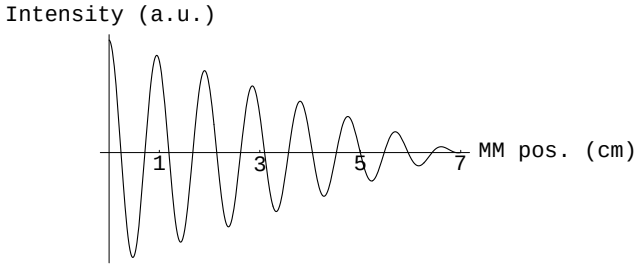

(a)

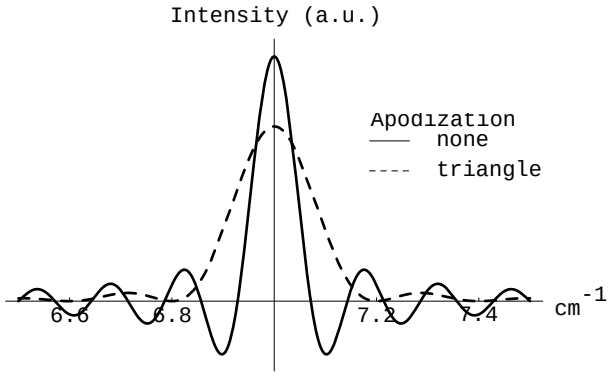

(b)

Figure C.6: a) The interferogram (Intensity vs. position of the moving mirror) for a monochromatic source modified by a triangle apodization function. b) The calculated spectrum from a monochromatic 7 cm^{-1} source with a mirror travel of 14 cm. The case of no apodization and apodization by a triangle function are shown.

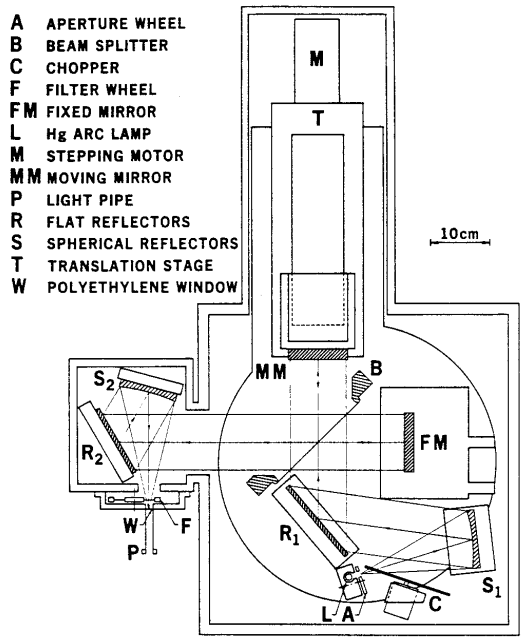

Figure C.7: A schematic of the Michelson interferometer used for FTIR spectroscopy studies. After [37]

C.5 Fourier transform spectrometer description

Far-infrared absorption and photoconductivity experiments were performed using a Fourier transform spectrometer constructed by J.M. Kahn [37], which is shown schematically in Figure C.7. The light source (L) is a Hg arc lamp, which is broadband in the far-infrared. Light from the source passes through a mechanical chopper (C) before being reflected toward the beamsplitter by a spherical mirror (S_1) and a subsequent flat mirror (R_1). The Mylar film beamsplitter (B) is removable, and can be chosen from a variety of thicknesses ranging from 3 μm to 250 μm. Each beamsplitter has efficiency maxima at different wavenumbers, as discussed in Section C.3, with the thickest beamsplitter giving the brightest transmission at low energy. The moving mirror (MM) is mounted to a translation stage controlled by a screw having a maximum travel of 25 cm. It is controlled by a step-

ping motor assembly that has 0.1 μm motion resolution. The length of the screw gives the spectrometer a theoretical maximum resolution of 0.012 cm^{-1}. The sum of the beams that reflect from the MM and fixed mirror (FM) and transmit through the beamsplitter, travel through a filter wheel before impinging on the sample. The interferometer is kept under vacuum during use in order to minimize absorption due to the excitation of vibrational and rotational modes in water vapor and other molecules, and to reduce the acoustic coupling of the optical components to room noise.

The transducer (usually a photoconductor, bolometer, or Golay cell) output signal is fed through a lock-in amplifier that contains a bandpass filter and phase sensitive detector that are tuned to the frequency of the chopper. The interferogram is recorded from the lock-in amplifier by a computer equipped with data acquisition (DAQ) hardware. The computer also controls the stepper motor and provides real time Fourier analysis of the interferogram during measurement.

Appendix D

Electrical transport characterization of semiconductors

A rigorous treatment of electrical transport in semiconductors requires a fully quantum mechanical theory. For many practical applications, however, such as the measurement of the resistivity and free carrier concentration, a quasi-classical treatment can be successfully applied. Within this treatment, electrons and holes are assumed to drift under an applied electric field as free particles traveling inside a solid medium, and have an effective mass described by the band structure of the material. The average velocity at which charge carriers travel within a semiconductor is called the drift velocity $\mathbf{v}_\mathrm{d}$. The current density $\mathbf{J}$ for both electron and hole drift is the product of the charge carrier density and the drift velocity, where n and p are the free electron and hole concentrations, respectively,

and q is the electronic charge

$$\mathbf{J}_{\mathrm{d}} = qn\mathbf{v}_{\mathrm{d}} \tag{D.1}$$

$$\mathbf{J}_{\mathrm{d}} = qp\mathbf{v}_{\mathrm{d}} \ . \tag{D.2}$$

The drift velocity of electrons or holes in response to an applied electric field **E** is approximated by Ohm's law

$$\mathbf{v}_{\mathrm{d}} = \mu\mathbf{E} \ . \tag{D.3}$$

The proportionality constant that determines the electron or hole velocity in a semiconductor as a function of electric field is called the carrier mobility μ. The mobility of a carrier having effective mass m^* is determined by the frequency that carriers undergo scattering, which is characterized by a scattering lifetime τ.

$$\mu = \frac{q\tau}{m^*} \tag{D.4}$$

The primary scattering mechanisms in a semiconductor crystal such as GaAs are ionized-impurity, neutral-impurity, and phonon scattering. Scattering by the absorption and emission of phonons is most important at higher temperatures while ionized-impurity scattering is typically the dominant scattering process below 300 K. Neutral-impurity scattering is only of significance at very low temperatures, usually less than 10 K. The details of scattering will not be discussed here; however, an excellent review of these scattering mechanisms and their effects on the electron and hole mobility is provided in the book by Ridley [56].

D.1 Electrical resistivity of semiconductors

The resistivity ρ is a materials property that is a measure of the current density which flows in response to an applied electric field. The resistivity in a solid depends on the concentration of free charge carriers and their mobility. For an n-type semiconductor with a parabolic, non-degenerate conduction band, the resistivity is defined according to Equation D.5

$$\rho = \frac{1}{nq\mu_{\mathrm{n}}} = \frac{m_{\mathrm{e}}^*}{nq^2\tau} \tag{D.5}$$

where n is the density of free electrons and m_{e}^* is the electron effective mass. The resistivity of semiconductors can be varied over several orders of magnitude because the free carrier concentration is a strong function of the temperature and the concentration of electrically active impurities. In semiconductors which are doped with shallow donor impurities, such as GaAs:Te, the concentration of electrons will be approximately $N_{\mathrm{D}} - N_{\mathrm{A}}$ at room temperature, where N_{D} is the donor concentration and N_{A} is the concentration of the acceptors present in the sample. In cases of low compensation, $n \approx N_{\mathrm{D}}$. At low to moderate doping levels, the resistivity is linearly dependent on the free carrier concentration, and will therefore vary according to the net dopant concentration.

The resistivity of a sample is independent of the geometry. For a perfectly uniform material, ρ can be obtained by measuring the resistance for a sample of known geometry. Equation D.6 relates the resistivity to the resistance (R), length (l), and cross-sectional area (A) of the sample

$$\rho = R\frac{A}{l} \ . \tag{D.6}$$

A standard resistance measurement yields the sum of the contributions from the sample and

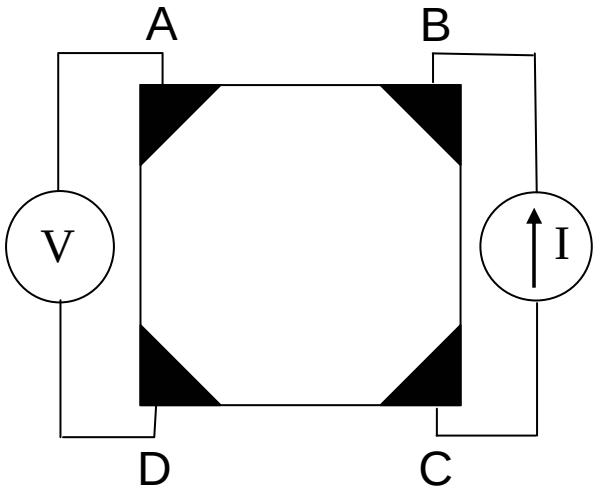

Figure D.1: The configuration for resistivity measurements using four probes to eliminate contact resistance. Current is supplied by the source I and the voltage is measured by meter V.

the contacts to the probes. Since the contact resistance is often the dominant contribution to the total resistance, a more sophisticated technique using separate current supplying and voltage sensing contacts is used. The so called four-point probe eliminates the contact resistance since virtually no current flows through the voltage sensing contacts. For a thin sheet or film of material of constant thickness, which is commonly encountered in the characterization of semiconductors, a typical contact scheme is displayed in Figure D.1, and the resistivity is found to be

$$\rho = \frac{V}{I}\frac{\pi t}{\ln 2}, \tag{D.7}$$

where t is the film thickness, and V is the voltage across contacts A and D that is formed when a current I is supplied through contacts B and C. This type of measurement has been adapted to simply connected samples of constant thickness and arbitrary shape, by van der Pauw [64]. The resistivity within the van der Pauw formulation is given by Equation D.8, where $R_{\mathrm{BC,AD}}$ represents the ratio of the voltage across contacts A and D to the

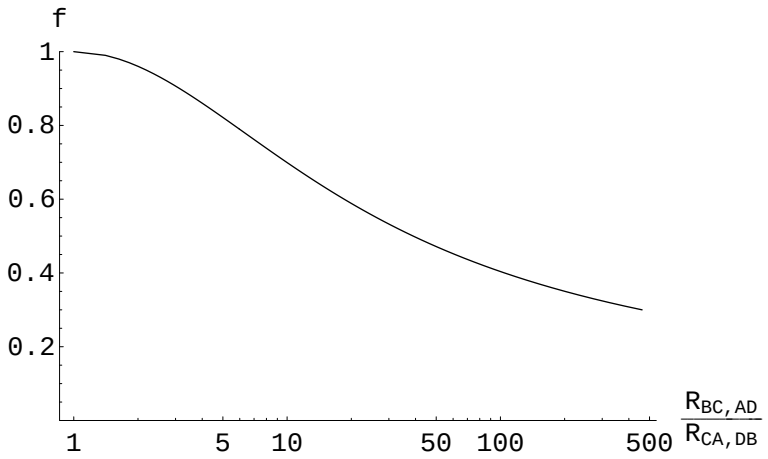

Figure D.2: The function f used in van der Pauw calculations, determined by the ratio $R_{\mathrm{BC,AD}}/R_{\mathrm{CA,DB}}$.

current supplied through contacts B and C, $R_{\mathrm{CA,DB}}$ represents the ratio of the voltage across contacts D and B to the current supplied through contacts C and A, and the factor f is a function of the ratio $R_{\mathrm{BC,AD}}/R_{\mathrm{CA,DB}}$, which depends on the sample geometry

$$\rho = \frac{\pi t}{\ln 2} \frac{R_{\mathrm{BC,AD}} + R_{\mathrm{CA,DB}}}{2} f \ . \tag{D.8}$$

According to van der Pauw [64], the factor f can be approximated:

$$f \approx 1 - \left(\frac{R_{\mathrm{BC,AD}} - R_{\mathrm{CA,DB}}}{R_{\mathrm{BC,AD}} + R_{\mathrm{CA,DB}}} \right)^2 \frac{\ln 2}{2} - \left(\frac{R_{\mathrm{BC,AD}} - R_{\mathrm{CA,DB}}}{R_{\mathrm{BC,AD}} + R_{\mathrm{CA,DB}}} \right)^4 \left(\frac{(\ln 2)^2}{4} - \frac{(\ln 2)^3}{12} \right) \ . \tag{D.9}$$

The plot of f in Figure D.2 shows the relative insensitivity to asymmetry of the contacts. When the resistances $R_{\mathrm{BC,AD}}$ and $R_{\mathrm{CA,DB}}$ differ by a factor of 5, f is only reduced from 1.0 to 0.8.

In practice, within the van der Pauw scheme, the resistances are measured for the four different configurations given in Table D.1. The resistance is measured twice in each configuration, once for each current direction. This allows verification that the contacts are of high quality and are ohmic in character.

configuration mode	voltage nodes	current nodes	current direction
1	CD	BA	+
2	CD	BA	-
3	AB	DC	+
4	AB	DC	-
5	DA	CB	+
6	DA	CB	-
7	BC	AD	+
8	BC	AD	-

Table D.1: Configuration modes for resistivity measurements by the van der Pauw technique. The contact nodes are as displayed in Figure D.1. Configuration mode 1 refers to $R_{\mathrm{BA,CD}} = V_{\mathrm{CD}}/I_{\mathrm{BA}}$.

D.2 The Hall effect

D.2.1 Carrier drift in a magnetic field

Under steady state conditions the drift velocity of electrons under applied electric (**E**) and magnetic (**B**) fields is determined by the Lorentz equation.

$$\mathbf{v}_{\mathrm{d}} = \frac{-e\tau}{m_{\mathrm{e}}^*}\left[\mathbf{E} + (\mathbf{v}_{\mathrm{d}} \times \mathbf{B})\right] \tag{D.10}$$

Taking the magnetic field in the z-direction B_{z}, the components of the current density are obtained by combining Equations D.10 and D.1.

$$J_{\mathrm{x}} = \frac{nq^2\tau}{m_{\mathrm{e}}^*}E_{\mathrm{x}} - \frac{qB_{\mathrm{z}}\tau}{m_{\mathrm{e}}^*}J_{\mathrm{y}} \tag{D.11}$$

$$J_{\mathrm{y}} = \frac{nq^2\tau}{m_{\mathrm{e}}^*}E_{\mathrm{y}} - \frac{qB_{\mathrm{z}}\tau}{m_{\mathrm{e}}^*}J_{\mathrm{x}} \tag{D.12}$$

$$J_{\mathrm{x}} = \frac{nq^2\tau}{m_{\mathrm{e}}^*}E_{\mathrm{z}}\ . \tag{D.13}$$

In the absence of a magnetic field, Equation D.11 becomes

$$J_{\mathrm{x}} = \frac{1}{\rho_{\mathrm{o}}}E_{\mathrm{x}}, \tag{D.14}$$

where

$$\sigma_{\mathrm{o}} = \frac{nq^2\tau}{m_{\mathrm{e}}^*} \tag{D.15}$$

is the zero-field conductivity, which is the inverse of the resistivity (Equation D.5). The second coefficient of Equations D.11 and D.12 is the cyclotron frequency of electrons traveling within the solid, in the presence of a field B_{z}.

$$\omega_{\mathrm{c}} = \frac{qB_{\mathrm{z}}}{m_{\mathrm{e}}^*} \ . \tag{D.16}$$

The magnetoconductivity tensor is determined by solving Equations D.11,D.12, and D.13.

$$\sigma(\mathrm{B_z}) = \frac{\sigma_{\mathrm{o}}}{1+(\omega_{\mathrm{c}}\tau)^2} \begin{pmatrix} 1 & \omega_{\mathrm{c}}\tau & 0 \\ \omega_{\mathrm{c}}\tau & 1 & 0 \\ 0 & 0 & 1+(\omega_{\mathrm{c}}\tau)^2 \end{pmatrix} .$$

The magnetic field applied in the z-direction has the effect of decreasing the conductivity in the x- and y-directions by the factor $1+(\omega_{\mathrm{c}}\tau)^2$ (according to the diagonal elements of the tensor). The off-diagonal elements indicates that under a magnetic field, currents are generated in the directions perpendicular to the applied electric field.

D.2.2 Measurement of the Hall effect

The Hall effect arises due to the finite off-diagonal terms of the magnetoconductivity tensor described in Section D.2.1. The measurement of the Hall effect yields the free carrier concentration, the carrier mobility, and majority carrier type of metals and semiconductors, making it one of the most powerful electrical characterization techniques. Under an applied magnetic field **B**, charge carriers flowing through a solid at velocity **v** (due to

an applied current) will be subjected to a Lorentz force

$$\mathbf{F} = -q\,(\mathbf{v}_\mathrm{d} \times \mathbf{B}) \tag{D.17}$$

where q is the electronic charge. As an example consider the sample of n-type semiconductor shown in Figure D.3. Electrons flowing through the sample along the x-direction due to an applied current I are deflected in the negative y-direction by the magnetic field, which is applied in the z-direction. This causes an accumulation of negative charges at the bottom of the sample and positive charges at the top, resulting in an electric field $\mathbf{E}_\mathrm{H}$=V_H/t known as the Hall field.

The magnitude of the Hall field is determined by the magnetic field and the current since a steady state is achieved when the electrostatic and magnetic forces balance.

$$q\mathbf{E}_H = q\,(\mathbf{v}_\mathrm{d} \times \mathbf{B}) \tag{D.18}$$

$$V_\mathrm{H} = B_\mathrm{z}\mathbf{v}_\mathrm{d}t\ . \tag{D.19}$$

The free electron concentration in an n-type semiconductor can be determined by measuring the Hall voltage and using Equation D.1.

$$n = \frac{wB_\mathrm{z}\mathbf{J}_\mathrm{d}}{qV_\mathrm{H}} = \frac{B_\mathrm{z}I}{qV_\mathrm{H}t} \tag{D.20}$$

The majority carrier type determines the sign of the Hall voltage. In the experimental setup of Figure D.3, the Hall voltage is positive for an n-type semiconductor and negative for a p-type semiconductor. In practice, within the van der Pauw scheme the current is applied diagonally across the sample. The order of measurements used for measuring the Hall effect in this work is summarized in Table D.2. Once the carrier concentration and resistivity

configuration mode	voltage nodes	current nodes	B	current direction
1	DB	CA	+	+
2	DB	CA	+	-
3	AC	DB	+	+
4	AC	DB	+	-
5	DA	CB	-	+
6	DA	CB	-	-
7	AC	BD	-	+
8	AC	BD	-	-

Table D.2: Configuration modes for Hall effect measurements by the van der Pauw technique. The contact nodes are as displayed in Figure D.1. Configuration mode 1 refers to $R_{\mathrm{DB,CA}} = V_{\mathrm{DB}}/I_{\mathrm{CA}}$.

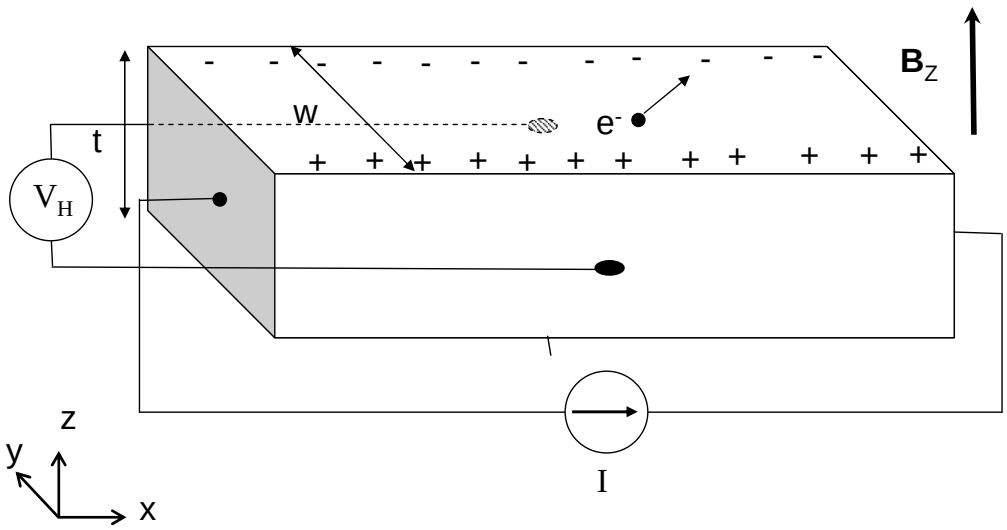

Figure D.3: The Hall voltage $\mathrm{V_H}$ is measured across an n-type semiconductor Hall bar sample of thickness t and width w, with magnetic field **B** directed into the page. A current I is supplied and electrons are deflected in the negative y-direction.

have been measured, it is possible to determine the Hall mobility μ_{H}.

$$\mu_{\mathrm{H}} = \frac{1}{nq\rho} \ . \tag{D.21}$$

D.2.3 The Hall factor correction

The Hall effect analysis of Section D.2.2 is only valid within the approximation that all electrons have the same energy. Realistically, electrons occupy a range of energies and therefore undergo a variety of scattering mechanisms. This causes a variation in the average value of the scattering time τ. The effect of the variation of the scattering time with carrier energy can be accounted for by the introduction of a numerical Hall factor

$$r_{\mathrm{H}} = \frac{\langle \tau^2 \rangle}{\langle \tau \rangle^2} \tag{D.22}$$

which is of the order of unity. When one scattering mechanism is strongly dominant, the Hall factor is close to unity. However when the probability of carrier scattering from multiple mechanisms are of the same order of magnitude, the Hall factor can introduce substantial deviations between the true and Hall effect determined values of the mobility and free carrier concentration. The Hall factor is therefore a function of the temperature and dopant concentration of a material since these two factors determine the magnitude of the primary scattering mechanisms. Calculations of the Hall factor for high purity n-type GaAs reveal a maximum value of $r_{\mathrm{H}} \approx 1.6$ at 10 K (Figure D.3). The true free carrier concentration and mobility are related to the Hall effect values by the Hall factor according

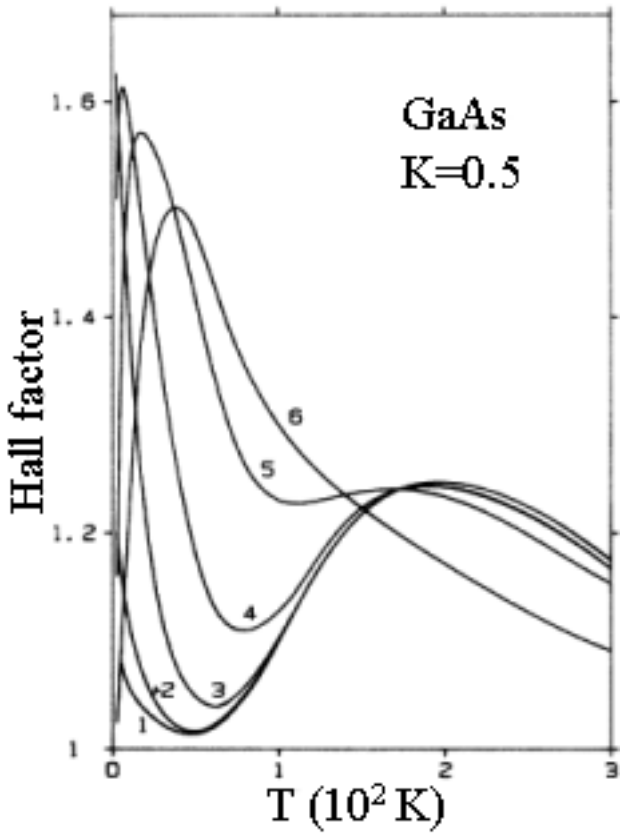

Figure D.4: Calculated values of the Hall factor for n-type GaAs as a function of temperature and donor concentration. N_d= 1) 0, 2) 10^{12}, 3) 10^{13}, 4) 10^{14}, 5) 10^{15}, 6) 10^{16}. [12]

to Equations D.23 and D.24.

$$n_{\mathrm{H}} = \frac{n}{r_{\mathrm{H}}} \tag{D.23}$$

$$\mu_{\mathrm{H}} = \mu r_{\mathrm{H}} \tag{D.24}$$

$$\tag{D.25}$$

In the limit of high magnetic field and mobility ($\mu B_{\mathrm{z}} \gg 1$) the Hall factor approaches unity. Therefore the Hall factor is usually taken as 1 for high purity samples of GaAs in moderate to high magnetic fields.

D.3 Free carrier statistics and variable temperature Hall effect

The concentration of electrons at a given energy within a semiconductor is determined by the density of states available and the probability of those states being filled at the given temperature. The density of states is determined by the band structure of the pure material and the presence of defects such as impurities. The probability of occupation of a state is determined by Fermi-Dirac statistics. The electron distribution within a band of energy dE at energy E is:

$$n(E)dE = G(E)F(E)dE \tag{D.26}$$

where $G(E)$ is the density of states and $F(E)$ is the Fermi function, given by Equation D.27.

$$F(E) = \frac{1}{e^{\frac{E-E_{\mathrm{F}}}{k_{\mathrm{B}}T}} + 1} \tag{D.27}$$

The Fermi function defines the probability that a state at energy E will be occupied by a carrier. The energy at which the probability of occupation is 50% is called the Fermi level E_{F}, which defines the chemical potential of the system. For energies significantly greater than E_{F} ($E - E_{\mathrm{F}} \approx 3k_{\mathrm{B}}T$ or greater) the Fermi function is well approximated by the Boltzmann distribution.

$$B(E) = e^{-\frac{E-E_{\mathrm{F}}}{k_{\mathrm{B}}T}} \quad . \tag{D.28}$$

For a pure semiconductor with no defects, the density of states is zero in the bandgap between the valence and conduction bands. The three dimensional density of states within a parabolic band is:

$$G(E)dE = \frac{1}{2\pi}\left(\frac{2m^*}{\hbar^2}\right)^{\frac{3}{2}}\sqrt{E - E_{\mathrm{c}}}dE \tag{D.29}$$

where E_{c} is the energy of the bottom of the band. For a derivation of Equation D.29 consult the book by Böer [14]. Equation D.29 is a good approximation for the conduction band of GaAs. The concentration of electrons in the conduction band as a function of temperature can be calculated by integrating Equation D.26 over the width of the band and using the Boltzmann approximation of Equation D.28. The upper limit of the integral can be taken as infinity since the Fermi function decreases rapidly above the Fermi level.

$$n = \int_{E_{\mathrm{c}}}^{\infty} G(E)B(E)dE \tag{D.30}$$

Using Equations D.28 and D.29, Equation D.30 becomes

$$n = N_{\mathrm{c}}e^{-\frac{E_{\mathrm{c}}-E_{\mathrm{F}}}{k_{\mathrm{B}}T}} \tag{D.31}$$

where the effective density of states with an electron effective mass m_{e}^*, N_{c}, is defined by

$$N_{\mathrm{c}} = 2\left(\frac{m_{\mathrm{e}}^* k_{\mathrm{b}} T}{2\pi\hbar^2}\right)^{\frac{3}{2}} \quad . \tag{D.32}$$

An equivalent analysis for a parabolic valence band gives the free hole concentration as

$$p = N_{\mathrm{v}} e^{-\frac{E_{\mathrm{F}}-E_{\mathrm{v}}}{k_{\mathrm{B}}T}} \tag{D.33}$$

$$N_{\mathrm{v}} = 2\left(\frac{m_{\mathrm{h}}^{*} k_{\mathrm{b}} T}{2\pi\hbar^{2}}\right)^{\frac{3}{2}} \tag{D.34}$$

where m_{h}^{*} is the hole effective mass and E_{v} is the highest energy in the valence band.

The temperature dependence of the equilibrium concentration of carriers in each band can be determined if the Fermi level is known. The position of the Fermi level depends strongly on the concentration of crystal defects, and their energy levels in the band gap. The equilibrium carrier concentrations are determined for the case of intrinsic and extrinsic semiconductors in the following sections.

D.3.1 The temperature dependence of the intrinsic carrier concentration

Within a perfect semiconductor at T=0 K each bond contains two electrons, and the valence band is exactly full. The conduction band is empty, and is separated from the valence band by the bandgap energy E_{g}. Above 0 K there exists a finite probability for an electron to be freed and thermally excited into the conduction band, creating a free hole in the valence band. Since the concentrations of holes and electrons in an intrinsic semiconductor are equal, the Fermi level will be near the middle of the bandgap at low temperatures. The temperature dependence of the Fermi level in an intrinsic semiconductor is determined by equating Equations D.31 and D.33.

$$E_{\mathrm{F}} = \frac{E_{\mathrm{g}}}{2} + \frac{3}{4} k_{\mathrm{B}} \ln \frac{m_{\mathrm{h}}}{m_{\mathrm{e}}} \tag{D.35}$$

The deviation from the middle of the bandgap is a linear function of the temperature, and depends on the ratio of the electron and hole effective masses.

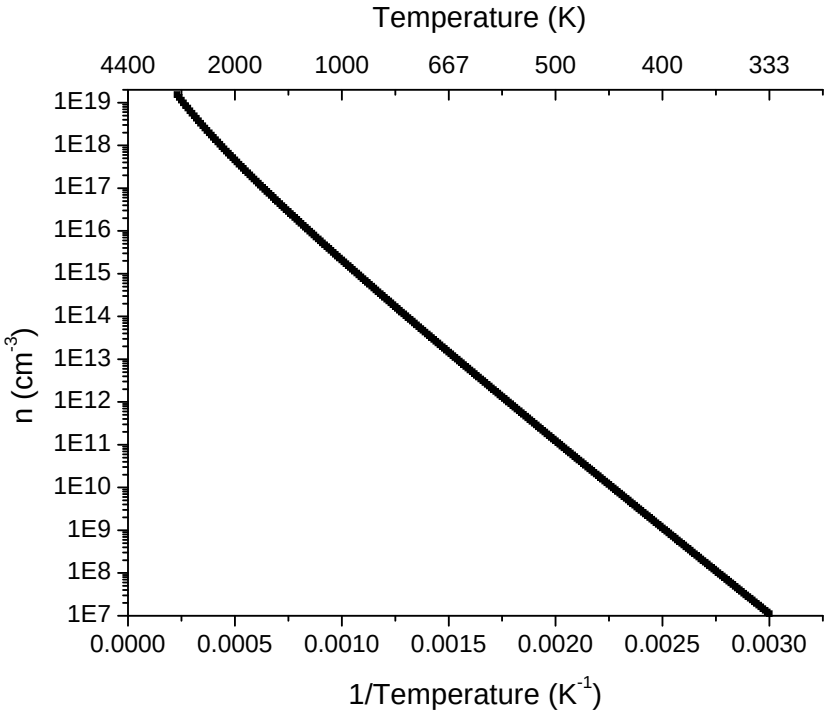

Figure D.5: The intrinsic carrier concentration for GaAs as a function of inverse temperature. The temperature dependence of the bandgap energy has been neglected.

The intrinsic carrier concentration, equal to the concentration of holes or electrons, is determined using Equations D.31 and D.33.

$$n_{\mathrm{i}} = \sqrt{N_{\mathrm{c}} N_{\mathrm{v}}} e^{\frac{-E_{\mathrm{g}}}{2k_{\mathrm{B}}T}} \tag{D.36}$$

Since the intrinsic carrier concentration increases mostly exponentially with temperature, a plot of n_{i} versus $1/T$ is approximately a straight line with a slope of $-E_{\mathrm{g}}/2k_{\mathrm{B}}$. The intrinsic carrier concentration for GaAs, with the bandgap assumed to be 1.45 eV and independent of temperature, is shown in Figure D.5. The deviation from linearity of this curve originates from the $T^{3/2}$ factor describing the effective density of states for the conduction and valence bands.

D.3.2 The temperature dependence of the extrinsic carrier concentration

In extrinsic, n-type GaAs there exist more donors than acceptors, and at T=0 K the number of electrons bound to donor impurities will be $N_{\mathrm{D}} - N_{\mathrm{A}}$. At finite temperature these electrons can be thermally excited into the conduction band without the simultaneous creation of a positively charged donor, not a hole, in contrast to the intrinsic case. The concentration of electrons in the conduction band is a function of the concentration of donor and acceptor impurities, the donor binding energy, and the temperature. Furthermore, free electrons occupying the conduction band due to excitation from impurity levels will greatly outnumber the intrinsic electron hole pairs at lower temperatures because the bandgap energy is much greater than the donor ionization energy.

For an n-type semiconductor ($N_{\mathrm{D}} - N_{\mathrm{A}} > 0$) with one type of monovalent donor species, the total concentration of electrons available to be excited into the conduction

band is $N = N_{\mathrm{D}} - N_{\mathrm{A}}$ since each acceptor impurity will be ionized by an electron from a donor. The N total electrons are distributed between the conduction band (n) and the donor impurity level (N^*):

$$N = N^* + n \ . \tag{D.37}$$

N^* is determined by the Fermi function at the donor ground state binding energy E_D, taking into account the spin degeneracy of 2 for donor levels in most semiconductors [13].

$$N^* = \frac{N_{\mathrm{D}}}{1 + \frac{1}{2} e^{-\frac{E_{\mathrm{F}} - E_{\mathrm{D}}}{k_{\mathrm{B}} T}}} \tag{D.38}$$

From Equation D.31 (with E_{c} taken as 0), the Fermi level within the Boltzmann approximation is found to be:

$$E_{\mathrm{F}} = k_{\mathrm{B}} T \ln \frac{n}{N_{\mathrm{c}}} \tag{D.39}$$

Inserting Equations D.38 and D.39 into Equation D.37 yields:

$$\frac{n \left(N_{\mathrm{D}} - N + n \right)}{N - n} = \frac{N_{\mathrm{c}}}{2} e^{\frac{E_{\mathrm{D}}}{k_{\mathrm{B}} T}} \tag{D.40}$$

Solving Equation D.40 for the free electron concentration, one finds:

$$n = \frac{\gamma + N_{\mathrm{A}}}{2} \left[\sqrt{1 + \frac{4 \left(N_{\mathrm{D}} - N_{\mathrm{A}} \right) \gamma}{\left(\gamma + N_{\mathrm{A}} \right)^2}} - 1 \right] \tag{D.41}$$

with

$$\gamma = \frac{N_{\mathrm{c}}}{2} e^{\frac{E_{\mathrm{D}}}{k_{\mathrm{B}} T}} \tag{D.42}$$

For the case of low compensation ($N_{\mathrm{D}} \gg N_{\mathrm{A}}$) and sufficiently low temperature such that most electrons are bound to donor impurities ($n \gg N_{\mathrm{D}}$), Equation D.41 can be approximated with:

$$n = \sqrt{\frac{N_{\mathrm{D}} N_{\mathrm{c}}}{2}} e^{\frac{E_{\mathrm{D}}}{2 k_{\mathrm{B}} T}} \tag{D.43}$$

The free electron concentration depends exponentially on the inverse absolute temperature with a pre-factor of $E_{\mathrm{D}}/2k_{\mathrm{B}}$. Curve (A) of Figure D.6 shows the calculated free electron concentration versus $1000/T$ for GaAs with no compensation. The slope of curve (A) is equal $E_{\mathrm{D}}/2k_{\mathrm{B}}$ as predicted by Equation D.43.

For the realistic case in which compensating acceptors are present, the free electron concentration becomes

$$n = \frac{N_{\mathrm{c}}}{2}\frac{N_{\mathrm{D}} - N_{\mathrm{A}}}{N_{\mathrm{A}}}e^{\frac{E_{\mathrm{D}}}{k_{\mathrm{B}}T}} \tag{D.44}$$

at sufficiently low temperatures such that $n \ll N_{\mathrm{D}}, N_{\mathrm{A}}$. The slope of line (C) of Figure D.6, which is representative of a highly compensated sample, is $E_{\mathrm{D}}/k_{\mathrm{B}}$. As the temperature is increased the free electron concentration will increase. When n becomes larger than N_{A}, but is still less than N_{D}, the free electron concentration is approximated by Equation D.45.

$$n = \sqrt{\frac{N_{\mathrm{D}}N_{\mathrm{c}}}{2}}e^{\frac{E_{\mathrm{D}}}{2k_{\mathrm{B}}T}} \tag{D.45}$$

This case is shown by curve (B) of Figure D.6, in which the slope changes from $E_{\mathrm{D}}/k_{\mathrm{B}}$ to $E_{\mathrm{D}}/2k_{\mathrm{B}}$ as the temperature is increased. The slope change occurs at $n = N_{\mathrm{A}}$.

At still higher temperature, nearly all electrons will be excited from donor states into the conduction band, and $n = N_{\mathrm{D}} - N_{\mathrm{A}}$. The electron concentration becomes constant until the temperature is high enough such that the intrinsic carrier concentration becomes comparable to or larger than $N_{\mathrm{D}} - N_{\mathrm{A}}$.

D.3.3 Variable temperature Hall effect

The calculated curves of Figure D.6 can be experimentally determined by measuring the Hall effect as a function of temperature. This allows for the calculation of the

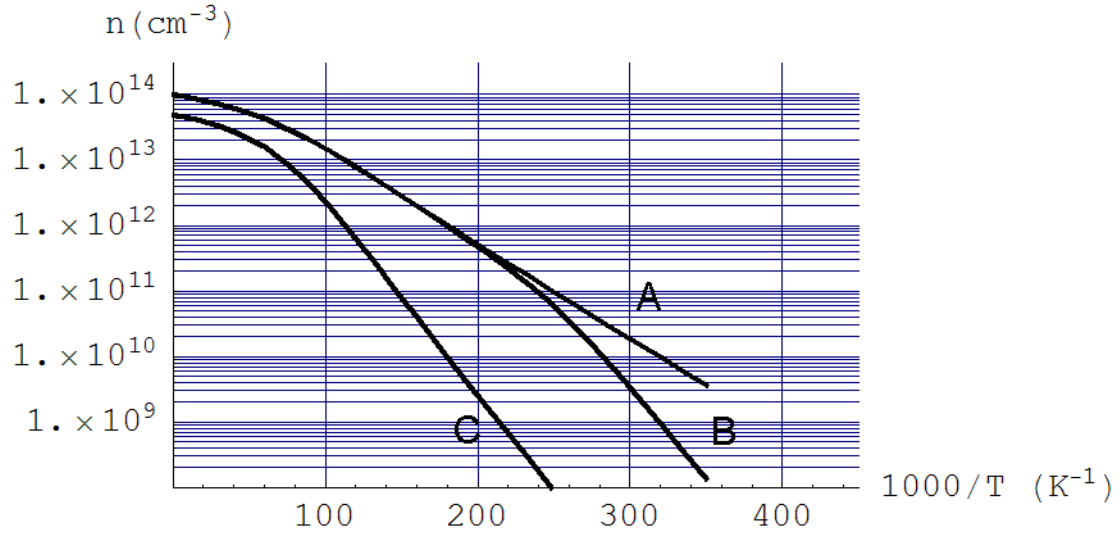

Figure D.6: Calculated temperature dependence of the electron concentration in n-type (N_{D}=1×10^{14} cm^{-3}) GaAs as a function of the compensation ratio. A) N_{A}=0, B) $N_{\mathrm{A}}/N_{\mathrm{D}}$=.01, C) $N_{\mathrm{D}}/N_{\mathrm{A}}$=.5.

majority dopant binding energy and concentration. When the compensation is sufficiently low ($N_A/N_D \leq .01$) the minority concentration can be determined by the location of the change in slope from $E_D/2k_B$ to E_D/k_B, as seen in curve (B) of Figure D.6.

Appendix E

GaAs LPE results

The following table contains a list of GaAs films grown by liquid-phase epitaxy. The sample names are classified according the substrate type as follows:

SI: semi-insulating

C: conducting

Samples which were intentionally doped with Te are designated by D. For example, sample 293 SID is an intentionally Te doped film, grown on a semi-insulating substrate. Samples grown on semi-insulating substrates were characterized by Hall effect. Samples grown on conducting substrates were characterized by capacitance-voltage measurements after deposition of a platinum Schottky barrier. Samples that have not been characterized by hall effect or capacitance-voltage were grown to study effects of growth parameters on the film morphology. Measurement of several samples was not possible because of irregular film growth, due to the incomplete coverage of the Ga+As solution over the substrate, or to the presence of a temperature gradient across the substrate during growth. These samples are

labeled IG in the table. The compensation ratio Θ has been estimated using the theoretical results of [66] for samples that have been measured at 77 K.

Sample	**Date**	**Crucible**	**Thickness** $[\mu m]$	$\mathbf{n}_{300}$ $[cm^{-3}]$	μ_{300} $[cm^2/V\ s]$	$\mathbf{n}_{77}$ $[cm^{-3}]$	μ_{77} $[cm^2/V\ s]$	Θ	**Type**	**Notes**
196 SI	5/24/01	graphite	70	1.15×10^{13}	8110	8.79×10^{12}	125000	0.9	n	
197 SI	5/29/01	graphite	86	1.22×10^{13}	8120	1.09×10^{13}	115000	0.9	n	
198 SI	5/30/01	graphite	110	3.33×10^{13}	8320	3.01×10^{13}	103000	0.78	n	
199 SI	5/31/01	graphite	180	2.80×10^{13}	6810	2.20×10^{13}	103000	0.76	n	
200 SI	6/4/01	graphite	86	7.45×10^{13}	6090	5.72×10^{13}	95400	0.7	n	
201 SI	6/10/01	graphite	118	5.33×10^{13}	6350	3.84×10^{13}	87700	0.83	n	
202 SI	6/11/01	graphite	54	4.75×10^{15}	7700					
203 SI	6/27/01	graphite	52	1.63×10^{15}	7400	1.32×10^{15}	49300	0.2	n	
204 SI	7/6/01	graphite								
205 SI	7/8/01	graphite								
206 SI	7/9/01	graphite								
207 SI	7/12/01	graphite								
208 SI	7/13/01	graphite								

Sample	**Date**	**Crucible**	**Thickness** $[\mu m]$	$\mathbf{n}_{300}$ $[cm^{-3}]$	μ_{300} $[cm^2/V\ s]$	$\mathbf{n}_{77}$ $[cm^{-3}]$	μ_{77} $[cm^2/V\ s]$	Θ	**Type**	**Notes**
209 SI	8/1/01	graphite								
210 C	8/12/01	graphite								
211 SI	8/15/01	graphite	60	1.80×10^{11}	8500				n	sent for PL
212 C	8/17/01	graphite								
213 C	8/18/01	graphite								
214 SI	8/19/01	graphite	75	7.70×10^{13}	7690	4.13×10^{13}	125000	0.59	n	
215 C	8/20/01	graphite								
216 SI	8/21/01	graphite	140	4.85×10^{13}	8790	4.37×10^{13}	124000	0.58	n	
217 SI	8/22/01	graphite	105	2.00×10^{13}	5040	1.43×10^{13}	73400	0.93	mixed	
218 SI	8/27/01	graphite								
219 C	8/28/01	graphite								
220 C	8/29/01	graphite								IG
221 SI	9/5/01	graphite								

Sample	**Date**	**Crucible**	**Thickness** $[\mu\text{m}]$	$\mathbf{n}_{300}$ $[\text{cm}^{-3}]$	μ_{300} $[\text{cm}^2/\text{V s}]$	$\mathbf{n}_{77}$ $[\text{cm}^{-3}]$	μ_{77} $[\text{cm}^2/\text{V s}]$	Θ	**Type**	**Notes**
222 SI	9/7/01	graphite	80			5.86×10^{13}	117000	0.56	n	
223 SI	9/21/01	graphite								
224 SI	9/24/01	graphite	85	1.55×10^{13}	8100	1.12×10^{13}	153000	0.76	n	
225 SI	9/25/01	graphite	90	1.68×10^{14}	6610	1.12×10^{14}	99000	0.50	n	
226 SI	9/26/01	graphite								
227 SI	10/4/01	graphite								
228 SI	10/8/01	graphite								
229 SI	10/9/01	graphite	100	1.63×10^{13}	8760	1.67×10^{13}	122000	0.81	n	
230 C	10/10/01	graphite								IG
231 SI	10/14/01	graphite								
232 C	10/15/01	graphite								IG
233 SI	10/17/01	graphite	65	4.34×10^{13}	7150	4.23×10^{13}	100000	0.75	n	
234 SI	10/31/01	graphite								

Sample	**Date**	**Crucible**	**Thickness** $[\mu\text{m}]$	$\mathbf{n}_{300}$ $[\text{cm}^{-3}]$	μ_{300} $[\text{cm}^2/\text{V s}]$	$\mathbf{n}_{77}$ $[\text{cm}^{-3}]$	μ_{77} $[\text{cm}^2/\text{V s}]$	Θ	**Type**	**Notes**
235 C	11/2/01	graphite								
236 SI	11/5/01	graphite	80	1.25×10^{13}	8250	1.21×10^{13}	117000	0.88	n	
237 C	11/15/01	graphite								
238 SI	11/17/01	graphite								
239 C	11/19/01	graphite								IG
240 C	11/27/01	graphite								
241 SI	11/28/01	graphite								IG
242 C	12/6/01	graphite								
243 SI	3/9/02	sapphire								IG
244 SI	3/11/02	sapphire	110	2.45×10^{15}	6770				n	
245 SI	4/24/02	sapphire								
246 C	4/28/02	sapphire								
247 SI	5/1/02	sapphire	120	1.93×10^{13}	8090	1.87×10^{13}	166000	0.53	n	

Sample	**Date**	**Crucible**	**Thickness** $[\mu m]$	$\mathbf{n}_{300}$ $[cm^{-3}]$	μ_{300} $[cm^2/V\ s]$	$\mathbf{n}_{77}$ $[cm^{-3}]$	μ_{77} $[cm^2/V\ s]$	Θ	**Type**	**Notes**
248 SID	5/4/02	sapphire	100	1.04×10^{18}	1530				n	
249 SID	5/6/02	sapphire								IG
250 SID	5/10/02	sapphire	50	1.55×10^{17}	3400				n	
251 SID	5/15/02	sapphire	170	5.89×10^{18}	1510				n	
252 SI	5/22/02	sapphire								
253 SI	5/28/02	sapphire								
254 SID	5/30/02	sapphire								
255 SID	6/2/02	sapphire	65	9.32×10^{14}	7500	6.15×10^{14}	27800	0.76	n	
256 SID	6/5/02	sapphire	150	1.69×10^{16}	5060				n	
257 SID	6/7/02	sapphire	80	1.20×10^{16}	5410				n	
258 SID	6/9/02	sapphire	150	1.63×10^{15}	3750	1.63×10^{15}	56300	0.09	n	
259 SID	6/11/02	sapphire	220	1.76×10^{16}	2800				n	
260 SID	7/9/02	sapphire								IG

Sample	**Date**	**Crucible**	**Thickness** $[\mu m]$	$\mathbf{n}_{300}$ $[cm^{-3}]$	μ_{300} $[cm^2/V\ s]$	$\mathbf{n}_{77}$ $[cm^{-3}]$	μ_{77} $[cm^2/V\ s]$	Θ	**Type**	**Notes**
261 SI	7/15/02	graphite								
262 SI	7/16/02	graphite								
263 SI	7/17/02	graphite								IG
264 SI	7/18/02	graphite	100	1.38×10^{14}	8440	1.26×10^{14}	106000	0.28	n	
265 SID	7/22/02	sapphire								IG
266 SID	7/24/02	sapphire	100	3.98×10^{17}	2730				n	
267 SID	7/29/02	sapphire								IG
268 SID	7/31/02	sapphire								
269 SI	8/5/02	graphite								
270 SI	8/7/02	graphite								
271 SI	8/12/02	sapphire								
272 SID	8/15/02	sapphire	127	2.28×10^{18}	1290				n	
273 SID	8/20/02	sapphire	93	3.70×10^{17}	3390				n	sent for PL

Sample	**Date**	**Crucible**	**Thickness** $[\mu m]$	$\mathbf{n}_{300}$ $[cm^{-3}]$	μ_{300} $[cm^2/V\ s]$	$\mathbf{n}_{77}$ $[cm^{-3}]$	μ_{77} $[cm^2/V\ s]$	Θ	**Type**	**Notes**
274 SID	8/12/02	sapphire	135	3.93×10^{17}	3240				n	
275 SID	8/29/02	sapphire	121	1.83×10^{17}	3750				n	
276 SID	9/1/02	sapphire	99	1.98×10^{17}	2630				n	
277 SID	9/3/02	sapphire	107	6.66×10^{16}	4330				n	sent for PL
278 SID	9/5/02	sapphire	118	1.35×10^{16}	5080				n	
279 SID	9/8/02	sapphire	175	5.32×10^{15}	5480				n	
280 SID	9/10/02	sapphire								
281 SID	9/13/02	sapphire	129	5.90×10^{15}	5570				n	
282 SI	9/15/02	graphite								
283 SI	9/17/02	graphite								
284 SID	9/19/02	sapphire	203	5.08×10^{15}	5140	3.71×10^{15}	20400	0.40	n	
285 SID	9/23/02	sapphire	123	7.86×10^{15}	5150				n	
286 SID	9/25/02	sapphire	48	1.00×10^{15}	5680	7.60×10^{14}	23600	0.77	n	

Sample	**Date**	**Crucible**	**Thickness** $[\mu\text{m}]$	$\mathbf{n}_{300}$ $[\text{cm}^{-3}]$	μ_{300} $[\text{cm}^2/\text{V s}]$	$\mathbf{n}_{77}$ $[\text{cm}^{-3}]$	μ_{77} $[\text{cm}^2/\text{V s}]$	Θ	**Type**	**Notes**
287 SID	10/3/02	sapphire								
288 SID	10/5/02	sapphire								
289 SI	10/14/02	graphite								
290 SI	10/23/02	graphite								
291 SI	12/6/02	sapphire	63	6.23×10^{12}	7900				n	
292 SID	12/9/02	sapphire	83	1.00×10^{15}	6550				n	
293 SID	12/11/02	sapphire	85	6.50×10^{16}	4380				n	
294 SID	12/13/02	sapphire	66	2.10×10^{16}	4490				n	
295 SID	12/15/02	sapphire	62	6.70×10^{15}	5280				n	
296 CD	12/17/02	sapphire								
297 SI	1/22/02	graphite								
298 SI	1/23/02	graphite								
299 SI	1/26/02	graphite								

Sample	**Date**	**Crucible**	**Thickness** $[\mu m]$	$\mathbf{n}_{300}$ $[cm^{-3}]$	μ_{300} $[cm^2/V\ s]$	$\mathbf{n}_{77}$ $[cm^{-3}]$	μ_{77} $[cm^2/V\ s]$	Θ	**Type**	**Notes**
300 SI	3/4/03	graphite	41	1.00×10^{12}	5200				mixed	
301 SI	3/5/03	graphite	31	1.86×10^{13}	5440				mixed	
302 SI	3/17/03	graphite								
303 SID	3/18/03	graphite	22	4.60×10^{14}	7030				n	
304 SID	3/19/03	graphite	28	1.22×10^{15}	8230	1.08×10^{15}	40500	0.45	n	
305 SID	3/20/03	graphite	32	6.55×10^{15}	5380			0.75	n	sent for PL
306 SID	3/25/03	graphite								
307 CD	4/2/03	graphite								
308 SID	4/6/03	graphite	13	1.08×10^{16}	4300			0.75	n	sent for PL
309 SID	4/9/03	graphite	15	8.90×10^{15}	5150			0.65	n	
310 SID	4/14/03	graphite	2	3.68×10^{15}	5660			0.70	n	
311 SID	4/15/03	graphite							n	
312 SI	5/17/03	graphite	87	1.90×10^{11}	2430				mixed	

Sample	**Date**	**Crucible**	**Thickness** $[\mu m]$	$\mathbf{n}_{300}$ $[cm^{-3}]$	μ_{300} $[cm^2/V\ s]$	$\mathbf{n}_{77}$ $[cm^{-3}]$	μ_{77} $[cm^2/V\ s]$	Θ	**Type**	**Notes**
313 SI	5/18/03	graphite	75	2.30×10^{14}	330				p	
314 C	5/20/03	graphite								
315 C	5/22/03	graphite								
316 SI	5/28/03	graphite	73	1.45×10^{13}	425				p	
317 SI	5/29/03	graphite	79	3.57×10^{13}	384				p	sent for PL
318 SI	6/5/03	graphite	87	5.60×10^{13}	439				p	
319 SI	6/9/03	graphite								
320 SI	6/12/03	sapphire	81	2.88×10^{14}	411				p	
321 SI	7/14/03	sapphire	85	5.39×10^{14}	227				p	
322 SI	7/17/03	sapphire	80	5.41×10^{14}	274				p	
323 SI	8/7/03	sapphire	70	9.31×10^{14}	383				p	
324 SI	9/8/03	graphite	80	3.27×10^{13}	390				p	
325 SI	9/9/03	graphite								

Sample	**Date**	**Crucible**	**Thickness** $[\mu\text{m}]$	$\mathbf{n}_{300}$ $[\text{cm}^{-3}]$	μ_{300} $[\text{cm}^2/\text{V s}]$	$\mathbf{n}_{77}$ $[\text{cm}^{-3}]$	μ_{77} $[\text{cm}^2/\text{V s}]$	Θ	**Type**	**Notes**
326 SI	9/20/03	graphite	76	2.55×10^{13}	430				p	
327 SI	9/24/03	graphite	71	3.60×10^{14}	388				p	
328 SI	9/30/03	sapphire	83	9.90×10^{14}	404				p	
329 SI	10/7/03	sapphire	80	5.06×10^{13}	8410				n	
330 SI	10/9/03	sapphire	74	1.67×10^{13}	7490	1.78×10^{13}	116000	0.80	n	
331 SI	10/13/03	sapphire								
332 SI	10/20/03	graphite								
333 SI	10/21/03	graphite								
334 SI	10/28/03	graphite	70	1.67×10^{13}	200				p	
335 SI	10/29/03	graphite								
336 SI	10/30/03	graphite								
337 SI	11/17/03	sapphire	83	1.43×10^{13}	8080	1.08×10^{13}	124000	0.88	n	
338 SI	11/19/03	sapphire	90	1.50×10^{13}	7800				n	

Sample	**Date**	**Crucible**	**Thickness** $[\mu\text{m}]$	$\mathbf{n}_{300}$ $[\text{cm}^{-3}]$	μ_{300} $[\text{cm}^2/\text{V s}]$	$\mathbf{n}_{77}$ $[\text{cm}^{-3}]$	μ_{77} $[\text{cm}^2/\text{V s}]$	Θ	**Type**	**Notes**
339 SI	11/23/03	sapphire	103	4.50×10^{12}	6500				mixed	
340 SI	11/25/03	sapphire	85	3.34×10^{12}	5100				mixed	
341 CD	12/11/03	sapphire								
342 SI	2/18/04	graphite								
343 SI	2/19/04	graphite								
344 SI	2/20/04	graphite								
345 SI	2/25/04	sapphire								
346 C	3/31/04	sapphire								
347 CD	4/21/04	sapphire								
348 CD	4/26/04	sapphire								
349 CD	4/29/04	sapphire								
350 CD	5/1/04	sapphire								
351 CD	5/15/04	sapphire		3.36×10^{16}					n	

Sample	**Date**	**Crucible**	**Thickness** $[\mu\text{m}]$	$\mathbf{n}_{300}$ $[\text{cm}^{-3}]$	μ_{300} $[\text{cm}^2/\text{V s}]$	$\mathbf{n}_{77}$ $[\text{cm}^{-3}]$	μ_{77} $[\text{cm}^2/\text{V s}]$	Θ	**Type**	**Notes**
352 CD	6/2/04	sapphire								
353 CD	6/4/04	sapphire		2.59×10^{16}					n	
354 CD	6/8/04	sapphire								
355 CD	6/15/04	sapphire		1.45×10^{16}					n	
356 CD	7/2/04	sapphire		5.45×10^{15}					n	
357 CD	7/5/04	sapphire		1.44×10^{15}					n	
358 CD	7/7/04	sapphire		1.17×10^{16}					n	
359 SI	7/12/04	sapphire								
360 SI	7/22/04	sapphire	88	6.00×10^{12}	1000				mixed	

Bibliography

[1] P. Ade. Cardiff University, UK.

[2] D. Alexiev, K. S. A. Butcher, M. Edmondson, and T. L. Tansley. Neutron transmutation doping of liquid phase epitaxial gallium arsenide. *Nuclear Inst. and Methods in Phys. Res. B*, **86**:288–292, (1994).

[3] R. J. Almassy, D. C. Reynolds, C. W. Litton, K. K. Bajaj, and G. L. McCoyu. Observation of shallow residual donors in high purity epitaxial GaAs by means of photoluminescence spectroscopy. *Solid State Communications*, **38**:1053–1056, (1981).

[4] P. W. Anderson. Absence of diffusion in certain random lattices. *Phy. Rev.*, **109**:1492–1505, (1958).

[5] C. J. Armistead, P. Knowles, S. P. Najda, and R.A. Stradling. Far-infrared studies of central-cell structure of shallow donors in gaas and inp. *Journal of Physics C: Solid State Physics*, **17**:6415–6434, (1984).

[6] M. G. Astles. *Liquid-Phase Epitaxial Growth of III-V Compound Semiconductor Materials and their Device Applications.* Adam Hilger, Bristol, UK, (1990).

[7] J. Bandaru, J. W. Beeman, E.E. Haller adn S. Samperi, and N. M. Haegel. Influence of the Sb dopant distribution on far infrared photoconductivity in Ge:Sb blocked impurity band detectors. *Infrared Physics & Technology*, **43**:353–360, (2002).

[8] E. Bauser. Atomic mechanisms in semiconductor liquid phase epitaxy. In D. T. J. Hurle, editor, *Handbook of Crystal Growth*, volume **3**, pages 880–939. Elsevier, Amsterdam, (1994).

[9] E. Bauser and W. Hagen. X-ray topography of growth step sources in LPE gallium arsenide. *Journal of Crystal Growth*, **50**:771–773, (1980).

[10] E. Bauser and H. P. Strunk. Microscopic growth mechanisms of semiconductors: experiments and models. *Journal of Crystal Growth*, **69**:561–580, (1984).

[11] R. J. Bell. *Introductory Fourier Transform Spectroscopy.* Academic Press, New York, (1972).

[12] M. Benzaquen, D. Walsh, and K. Mazuruk. Hall factor of doped n-type GaAs and n-type InP. *Physical Review B*, **12**:8947–8949, (1986).

[13] J. S. Blakemore. *Semiconductor Statistics.* Dover, New York, (1987).

[14] K. W. Böer. *Survey of Semiconductor Physics.* Van Nostrand Reinhold, New York, (1990).

[15] P. R. Bratt. Impurity germanium and silicon infrared detectors. In R. K. Willardson and A. C. Beer, editors, *Infrared Detectors II*, volume **12** of *Semiconductors and Semimetals*, pages 39–142. Academic Press, New York, (1977).

[16] W.K. Burton, N. Cabrera, and F.C. Frank. The growth of crystals and the equilibrium structure of their surfaces. *Philosophical Transactions of the Royal Society of London. Series A, Mathematical and Physical Sciences*, **243**:299–358, (1951).

[17] J.E. Chamberlain. *The Principles of Interferometric Spectroscopy*. Wiley, New York, (1979).

[18] J.W. Christian. *The Theory of Phase Transformations in Metals and Alloys*. Pergamon Press, Oxford, (1965).

[19] J. E. Van Cleve, T. L. Herter, R. Butturini, G. E. Gull, J. R. Houck, B. Pirger, and J. Schoenwald. Evaluation of Si:As and Si:Sb blocked-impurity-band detectors for SIRTF and WIRE. *Proceedings of the SPIE*, **2553**:502–513, (1995).

[20] Dupont Corporation. Mylar: Optical properties.

[21] E. Czech, G. Gotz, G. Cristiani, and M. Konuma. Residual impurities in high purity GaAs layers grown by liquid phase epitaxy in H_2-Ar atmosphere. *Journal of Crystal Growth*, **198 − 199**:1087–1091, (1999).

[22] C. Domke, Ph. Ebert, M. Heinrich, and K. Urban. Microscopic identification of the compensation mechanisms in Si-doped GaAs. *Physical Review B*, **54**:10288–10299, (1996).

[23] K.E. Easterling and D.A. Porter. *Phase Transformations in Metals and Alloys*. Chapman & Hall, New York, (1992).

[24] P. Fellgett. Multiplex interferometric spectrometry for infrared measurements on stars. *Journal de Physique et le Radium*, **19**:187, (1958).

[25] H. Fritzsche and M. Cuevas. Impurity conduction in transmutation-doped p-type germanium. *Physical Review*, **119**:1238–1245, (1960).

[26] J. Gebauer and E.R. Weber. Determination of the charge carrier compensation mechanism in Te-doped GaAs by scanning tunneling microscopy. *Applied Physics Letters*, **82**:2059–2061, (2003).

[27] E. E. Haller. Physics and design of advanced IR bolometers and photoconductors. *Infrared Physics*, **25**:257–266, (1985).

[28] P. C. Hargrave, J. W. Beeman, P. A. Collins, I. Didschuns, M. J. Griffin, B. Kiernan, and G. Pisano. In-flight calibration sources for Herschel-SPIRE. In *Proceedings of the SPIE*, volume **4850**, pages 638–649, (2003).

[29] H. Hasegawa. Theory of cyclotron resonance in strained Si crystals. *Physical Review*, **129**:1029–40, (1963).

[30] G. B. Heim, M. L. Henderson, K. I. Macfeely, T. J. Mcmahon, D. Michika, R. J. Pearson, G. H. Rieke, J. P. Schwenker, D.W. Strecker, C.L. Thompson, R.M. Warden, D. A. Wilson, and E. T. Young. Multiband imaging photometer for SIRTF. *Proceedings of the SPIE*, **3356**:985–1000, (1998).

[31] R. J. Heron, R. A. Lewis, P. E. Simmonds, R. P. Starrett, A. V. Skougarevsky, R. G. Clark, and C. R. Stanley. Central-cell corrections for Si and S in GaAs in a strong magnetic field. *Journal of Applied Physics*, **85**:893–896, (1999).

[32] http://mips.as.arizona.edu.

[33] D. T. J. Hurle. A comprehensive thermodynamic analysis of native point defect and dopant solubilities in gallium arsenide. *Journal of Applied Physics*, **85**:6957–7022, (1999).

[34] B. Iannotta. Seeing stars with SOFIA. *Aerospace America*, pages 39–42, (2002).

[35] Infrared Laboratories, Inc. Tucson, AZ.

[36] S. Geradin Jayam and K. Navaneethakrishnan. Central-cell corrections and shallow donor states in strong magnetic fields. *Journal of Applied Physics*, **89**:6198–6203, (2001).

[37] J.M. Kahn. *Hydrogen-related acceptor complexes in germanium.* PhD thesis, University of California at Berkeley, (1986), unpublished.

[38] H. Kamimura and H. Aoki. *The physics of interacting electrons in disordered systems.* Clarendon Press, Oxford, (1989).

[39] A. G. Kazanskii, P. L. Richards, and E. E. Haller. Far-infrared photoconductivity of uniaxially stressed germanium. *Applied Physics Letters*, **31**:496–97, (1977).

[40] C. Kittel. *Introduction to solid state physics.* 7th Edition, Wiley, New York, (1996).

[41] M. Konuma, I. Silier, E. Czech, and E. Bauser. GaAs layers grown on 100 mm diameter substrates in a liquid phase epitaxy centrifuge. *Proceedings of the Twentieth International Symposium on Gallium Arsenide and Related Compounds*, pages 829–830, (1994).

[42] Lake Shore Cryotronics, Inc. Westerville, OH.

[43] D. M. Larsen. Inhomogeneous broadening of the Lyman-series absorption of simple hydrogenic donors. *Physical Review B*, **13**:1681–91, (1976).

[44] J. Leotin. Far infrared photoconductivity studies in silicon blocked impurity band structures. *Infrared Physics and Technology*, **40**:153–60, (1999).

[45] N. Lum, J. Asbrock, R. White, R. Kelchner, L. Lum, L. Pham, C. McCreight, M. McKelvey, R. McMurray, W. Forrest, and J. Garnett. Low-noise, low-temperature, 256x256 Si:As IBC staring FPA. In *Proceedings of the SPIE*, volume **1946**, pages 100–109, (1993).

[46] T. B. Massalski. *Binary Alloy Phase Diagrams*. American Society for Metals, Materials Park, OH, USA, (1986).

[47] L. Mo, K.S.A. Butcher, and D. Alexiev. Effect of crucible materials on impurities in LPE-GaAs. *Journal of Crystal Growth*, **160**:7–12, (1996).

[48] N. Mott, M. Pepper, S. Pollitt, R. H. Wallis, and C.J. Adkins. The Anderson transition. *Proc. Royal. Soc. A*, **345**:169–205, (1975).

[49] N. F. Mott and E. A. Davis. *Electronic processes in non-crystalline materials*. Clarendon Press, Oxford, (1979).

[50] H. Nishimura. Impurity conduction in the intermediate concentration range. *Physical Review*, **138**:A815–A821, (1965).

[51] E. D. Palik. *Handbook of Optical Constants of Solids.* Academic Press, New York, (1985).

[52] S. Pasquier, G. Sirmain, C. Meny, A. Murray, M. Griffin, P. Ade, L. Essalch, J. Galibert, and J. Leotin. Low compensation impurity band photoconductors. In *Proceedings of the SPIE*, volume **2211**, pages 634–48, (1994).

[53] M. D. Petroff and M. G. Stapelbroek. Blocked impurity band detectors. US Patent no. 4568960, (1980).

[54] W.T. Read. *Dislocations in Crystals.* McGraw Hill, New York, (1953).

[55] P. L. Richards. Bolometers for infrared and millimeter waves. *Journal of Applied Physics*, **76**:1–24, (1994).

[56] B.K. Ridley. *Quantum processes in Semiconductors.* Clarendon Press, Oxford, (1988).

[57] G. H. Rieke. *Detection of Light from the Ultraviolet to the Submillimeter.* Cambridge University Press, Cambridge, UK, (1994).

[58] R. Schnurr, C. L. Thompson, J. T. Davis, J. W. Beeman, J. Cadien, E. T. Young, E. E. Haller, and G. H. Rieke. Design of the stressed Ge:Ga far-infrared array for SIRTF. In *Proceedings of the SPIE*, volume **3354**, pages 322–31, (1998).

[59] B. I. Shklovskii and A. L. Efros. *Electronic Properties of Doped Semiconductors*, volume 45 of *Springer series in solid state sciences.* Springer-Verlag, Berlin, (1984).

[60] Sumitomo Corporation. Tokyo, Japan.

[61] C. H. Townes and R. Genzel. What is happening at the center of our galaxy? *Scientific American*, **262**:46–55, (1990).

[62] W. A. Traub and M. T. Stier. Theoretical atmospheric transmission in the mid- and far-infrared at four altitudes. *Applied Optics*, **15**:364–77, (1976).

[63] UC Davis McClellan Nuclear Research Center. Sacramento, CA.

[64] L. J. van der Pauw. A method of measuring specific resistivity and Hall effect of discs of arbitrary shapes. *Philips Research Reports*, **13**:1–9, (1958).

[65] W. Walukiewicz. Amphoteric native defects in semiconductors. *Applied Physics Letters*, **54**:2094–2096, (1989).

[66] W. Walukiewicz, L. Lagowski, and H. C. Gatos. Electron mobility in n-type GaAs at 77 K; determination of the compensation ratio. *Journal of Applied Physics*, **53**:769–770, (1981).

[67] W. Walukiewicz, L. Lagowski, L. Jastrzebski, M. Lichtensteiger, and H. C. Gatos. Electron mobility and free carrier absorption in GaAs: Determination of the compensation ratio. *Journal of Applied Physics*, **50**:899–908, (1979).

[68] S. P. Watkins, G. Haacke, H. Burkhard, M. L. W. Thewalt, and S. Charbonneau. Magnetophotoluminescence characterization of residual donors in GaAs grown by metalorganic chemical vapor deposition. *Journal of Applied Physics*, **64**:3205–3209, (1983).

[69] D. I. Wynne. Liquid phase epitaxial growth of gaas. Master's thesis, University of California at Berkeley, (1997), unpublished.

[70] N.A. Yakusheva, K.S. Zhuravlev, S.I. Chikichev, and O.A. Shegaj. Liquid phase epitaxial growth of undoped gallium arsenide from bismuth and gallium melts. *Crystal Research and Technology*, **24**:235–46, (1989).

[71] P. Y. Yu and M. Cardona. *Fundamentals of Semiconductors*. 3rd Edition, Springer, Berlin, (2001).